Technische Universität München

In vitro Dissection of Intraflagellar Transport in *C. elegans* Sensory Cilia

Mohamed Antar Aziz Mohamed

A thesis submitted for the degree of Doctor of Philosophy

2020

Fakultät für Physik Technische Universität München Lehrstuhl für Biophysik

In vitro Dissection of Intraflagellar Transport in *C. elegans* Sensory Cilia

Mohamed Antar Aziz Mohamed

Vollständiger Abdruck der von der Fakultät für Physik der Technischen Universität München zur Erlangung des akademischen Grades eines Doktors der Naturwissenschaften (Dr. rer. nat.) genehmigten Dissertation.

Vorsitzender: Prof. Dr. Martin Zacharias

Prüfer der Dissertation:

1. TUM Junior Fellow Dr. Zeynep Ökten
2. Prof. Dr. Matthias Feige

Die Dissertation wurde am 21.07.2020 bei der Technischen Universität München eingereicht und durch die Fakultät für Physik am 28.10.2020 angenommen.

Publications

Some figures in part I have been adapted from the following publication:

Mohamed, M.A.A., W.L. Stepp, and Z. Ökten, Reconstitution reveals motor activation for intraflagellar transport. *Nature*, 2018. **557**(7705): p. 387-391.

Summary

Cilia, motile and sensory, are microtubule-based structures that emanate from the cell membrane of many eukaryotic cells, including most cell types of the human body. The specialized location and properties of cilia allow them to be involved in a wide range of vital processes such as development, motility, and signalling, to name but a few. Nearly all cilia are built and continuously maintained by the universally conserved IntraFlagellar Transport (IFT). IFT requires a multi-subunit, non-membranous protein complex assembled from 22 subunits that are categorized into IFT-A and IFT-B complexes. It is driven by the cilia specific kinesin-2 and dynein-2 motors along the polarized microtubules of the ciliary axoneme. During IFT, the building blocks of the axoneme (tubulins) are transported from the ciliary base to the ciliary tip (anterograde transport) via the kinesin-2 motor, whereas the dynein-2 motor transports the turnover products from the ciliary tip back to the ciliary base (retrograde transport). However, to power the retrograde transport, the dynein-2 motor must first be delivered in an inactive form to the ciliary tip by the anterograde kinesin-2 motor.

C. elegans is by far considered the best characterized model system for sensory cilia function. It deploys two types of kinesin-2 motors: the heterotrimeric kinesin-II motor and the homodimeric OSM-3 motor that function redundantly to transport IFT trains along axonemes of sensory cilia. While the kinesin-II motor associates with the IFT-A complex, the OSM-3 motor associates with the IFT-B complex. The functional diversity of *C. elegans* sensory cilia appears to be traceable to the differential regulation of the kinesin-2-powered IFT. Although much progress has been made by multiple laboratories in understanding the basis of IFT over the past years, molecular mechanisms governing IFT trains assembly/restructuring, recruitment of motors to IFT, and the spatio-temporal activation/deactivation of motors are still unknown.

In this thesis, we made use of a systematic bottom-up reconstitution approach to decipher the molecular pathways of OSM-3 recruitment and activation for anterograde transport (part I) and give insights into mechanisms of regulated assembly and restructuring of IFT trains in the sensory cilia of *C. elegans* (part II). While both the Quadripartite Core Complex (QCC) and the Tripartite Core Complex (TCC) were formed stably, only the QCC, and not the TCC, incorporated the OSM-3 motor into a motor-cargo complex with a nanomolar binding affinity. Importantly, the removal of the DYF-1 subunit from the QCC complex completely disrupted the complex formation between the OSM-3 motor and its cargo. As expected from this biochemical characterization, biophysical assays finally provided the functional evidence that the DYF-1 subunit is indeed the key recruiter

of the OSM-3 motor for its allosteric activation. In particular, the fluorophore-labeled OSM-3 incorporated into QCC and moved directionally on surface attached microtubules in a Total Internal Reflection Fluorescence (TIRF) microscope. Results presented here provide a molecular explanation for previous in vivo studies showing that in the absence of *dyf-1* function, the OSM-3 motor is detached from the IFT trains and can only display unbiased diffusion in the cilium. In summary, part I of this thesis describes the first in vitro reconstituted IFT-motor complex and reveals the molecular mechanism of motor recruitment and activation for efficient IFT.

Molecular mechanisms of spatially-regulated assembly and restructuring of IFT trains are still mysterious. Preliminary experimental evidences presented in part II propose that phosphorylation-regulated processes may give rise to the assembly and restructuring of the IFT trains in vivo. Specifically, the DYF-5 and DYF-18 kinases are promising regulatory factors that might modulate the structural integrity of the IFT trains. First, these kinases display a seemingly mutually-exclusive localization pattern between the ciliary base and the ciliary tip, where IFT trains assemble and restructure, respectively. Second, in in vitro phosphorylation assays, these kinases specifically phosphorylate a subset of six subunits from the IFT-B complex. Three subunits (CHE-13, DYF-3, and OSM-5) of the total six phosphorylation targets are located at the evolutionary conserved interface between the IFT-B core complex and the IFT-B peripheral complex. Phosphorylation by the DYF-18 kinase interferes with the structural properties of the CHE-13 and DYF-3 subunits, as it induces them to multimerize, suggesting that the kinase might play a regulatory role in IFT train assembly at the ciliary base. In contrast, phosphorylation by the tip-localized DYF-5 kinase induces disassembly of the oligomeric DYF-11 subunit. Notably, this particular subunit of the IFT-B peripheral complex has been implicated into the turnaround of IFT trains at the ciliary tip in vivo. The disassembly of the DYF-11 oligomer is prevented in the presence of the conserved DYF-11 interaction partner Y110A7A.20 subunit, suggesting that the assembly and disassembly of DYF-11 might be additionally regulated by the Y110A7A.20 subunit. Taken together, results presented in part II provide first evidence that the structural integrity of IFT subunits are subject to phosphorylation-regulated processes. These findings therefore serve as an experimental platform to further dissect the complex formation properties of the IFT subunits and promise to eventually reveal the molecular mechanisms of how IFT train assembly/disassembly might be regulated in vivo.

Zusammenfassung

Zilien sind Zellfortsätze, die aus der Membran vieler eukaryotischer Zellen hervorstehen. So weisen auch die meisten menschlichen Zellen motile oder sensorische Varianten dieser microtubuli-basierten Strukturen auf. Die spezielle Positionierung und Eigenschaften von Zilien ermöglichen ihren Einsatz in einem breiten Spektrum an wichtigen Prozessen der Zelle wie Entwicklung, Motilität und Signalverarbeitung, um nur ein paar zu nennen. Nahezu alle Zilien werden durch den universell konservierten IntraFlagellaren Transport (IFT) gebaut und in Stand gehalten. IFT basiert auf einem Proteinkomplex, der aus 22 Einzelteilen assembliert wird und in den IFT-A- und IFT-B-Komplex kategorisiert wird. Der Transport wird realisiert durch zilienspezifische kinesin-2- und dynein-2-Motoren, die auf den polarisierten Microtubuli des ziliären Axonemes aktiv sind. Durch IFT werden die Bausteine des Axonems (Tubuline) von der Basis des Ziliums zu seiner Spitze transportiert. Dieser Transport wird von kinesin-2 übernommen (Hintransport), während der Rücktransport der umgesetzten Produkte von der Spitze an die Basis von dynein-2 übernommen wird. Um den Rücktransport zu ermöglichen, muss der dynein-2-Motor allerdings erst in einer inaktiven Form vom kinesin-2-Motor an die Spitze gebracht werden.

C. elegans ist bei weitem das am besten charakterisierte Modellsystem für die Funktion von sensorischen Zilien. Es setzt zwei Typen von kinesin-2-Motoren ein, die eine Redundanz des Systems ermöglichen: das heterotrimere kinesin-II und den homodimeren OSM-3-Motor. Während kinesin-II mit dem IFT-A-Komplex interagiert, bindet OSM-3 an den IFT-B-Komplex. Die Vielfalt der sensorischen Zilien in *C. elegans* scheint auf die feine Steuerung des kinesin-2 getriebenen IFT zurückzuführen zu sein. In den letzten Jahren haben verschiedene Labore große Fortschritte im Verständnis der Grundlagen des IFT erzielt, die molekularen Mechanismen, die den Zusammenbau und die Restrukturierung von IFT beherrschen, die Heranziehung von Motoren für den IFT und die zeit- und ortsbezogene De-/Aktivierung von Motoren sind indes noch unbekannt.

In dieser Arbeit haben wir einen systematischen bottom-up-Rekonstruktionsansatz genutzt, um die molekularen Wege des Einbezugs von OSM-3 und seine Aktivierung in diesem Kontext aufzuklären (Teil I). Außerdem geben wir Einblick in die Mechanismen des gesteuerten Zusammenbaus und der Restrukturierung von IFT-Zügen in den sensorischen Zilien von *C. elegans* (Teil II). Währen sowohl der Quadripartite Core Complex (QCC) und der Tripartite Core Complex (TCC) stabile Komplexbildung zeigten, erfolgte die Bindung des OSM-3-Motors mit nanomolarer Bindeaffinität nur durch QCC, nicht durch TCC. Wichtig ist, dass das Entfernen der DYF-1-Untereinheit des QCC-Komplexes eine komplette Auflösung der OSM-3-Bindung zur Folge hatte. Wie durch

diese biochemische Charakterisierung erwartet, lieferten biophysikalische Experimente die funktionelle Bestätigung, dass DYF-1 der Schlüssel für eine allosterische Aktivierung des OSM-3 und seine Einbindung in den QCC ist. So bewegte sich OSM-3 zusammen mit dem QCC entlang oberflächengebundener Microtubuli unter dem Fluoreszenzmikroskop, dessen Beleuchtung auf der totalen internen Reflexion von Licht beruht (TIRF). Die hier präsentierten Ergebnisse liefern eine molekulare Erklärung für vorhergegangene in-vivo-Studien, die eine Dissoziation von OSM-3 und IFT-Zügen in der Abwesenheit von DYF-1-Funktion gezeigt hatten. Außerdem zeigte der Motor keine gerichtete Bewegung mehr, sondern war auf ungerichtete Diffusion entlang der Microtubuli beschränkt. Zusammenfassend beschreibt Teil I dieser Arbeit den erstmals in vitro rekonstruierten IFT-Motor-Komplex und zeigt den molekularen Mechanismus der Einbindung und Aktivierung des Motors für effizienten IFT.

Die molekularen Mechanismen der Regulierung von Aufbau und Restrukturierung der IFT-Züge sind weiterhin rätselhaft. Vorläufige Ergebnisse in Teil II dieser Arbeit weisen darauf hin, dass Prozesse, die durch Phosphorylierung geregelt sind, für diese Regulierung in vivo verantwortlich sein könnten. Besonders die Kinasen DYF-5 und DYF-18 sind vielversprechende Kandidaten für Regulatoren, die die strukturelle Integrität der IFT-Züge modulieren könnten. Zum einen ist DYF-5 an der Spitze, DYF-18 hingegen an der Basis des Ziliums zu finden, wo die IFT-Züge entsprechend aufgebaut beziehungsweise restrukturiert werden. Zum anderen phosphorylieren diese Kinasen spezifisch sechs Untereinheiten des IFT-B-Komplexes in vitro. Drei dieser Untereinheiten (CHE-13, DYF-3 und OSM-5) befinden sich im Komplex an der evolutionär konservierten Schnittstelle zwischen dem IFT-B-Kern- und dem IFT-B-Außenkomplex. Phosphorylierung durch DYF-18 begünstigt die Multimerisierung von CHE-13 und DYF-3, was eine regulierende Rolle der Kinase bei der Assemblierung der IFT-Züge an der Basis des Ziliums nahelegt. Die an der Spitze präsente Kinase DYF-5 führt dagegen durch Phosphorylierung des oligomeren DYF-11 zu dessen Monomerisierung. Gerade diese Untereinheit des IFT-B Komplexes wurde mit der Restrukturierung der IFT-Züge an der Spitze des Ziliums in vivo in Verbindung gebracht. Diese Komplexauflösung wird außerdem durch den ebenfalls evolutionär konservierten Interaktionspartner Y110A7A.20 verhindert, dies legt einen weiteren Regulierungsmechanismus durch diese Untereinheit nahe. Zusammenfassend liefert Teil II dieser Arbeit erste Beweise, dass die strukturelle Integrität von IFT-Untereinheiten durch Prozesse der Phosphorylierung gesteuert wird. Damit legen die Ergebnisse eine experimentelle Grundlage, um die komplexen Interaktionen der IFT-Untereinheiten weiter zu untersuchen und damit letztendlich die molekularen Mechanismen des Auf- und Abbaus des IFT-Zugs in vivo zu erklären.

Contents

1 Introduction

1.1 Cilia: a historical glance

Cilia and flagella are interchangeable terms used to describe the microtubule-based protrusions that emanate from the surface of most eukaryotic cells, with the exception of cells of higher plants and fungi (Figure 1). Cilia are ubiquitously distributed in vertebrate cells, whereas they are restricted to sensory neurons in invertebrate cells [1]. They were first observed by the Dutch microbiologist Antony van Leeuwenhoek in 1674–1675; in a letter to the Royal Society of London, he described tiny animalcules ‘‘most likely ciliate protozoa’’ with incredibly thin feet, which were moved nimbly [2, 3]. Later, these little feet were termed cilia (meaning hair or eyelash in Latin).

Historically, cilia are classified into motile and immotile forms. Motile cilia have a rich and long research history, and their structure and function have been studied extensively. They have evolved to carry out various functions with the best known one being ‘‘motility’’. By beating in a rhythmic manner, motile cilia move cells through fluid media such as in *C. reinhardtii* and sperms, or move fluids over stationary cell surfaces such as cilia on tracheal cells beat to clear mucus away, while those in the brain are responsible for circulation of the cerebrospinal fluid [4].

Immotile cilia (also referred to as primary or sensory cilia) are solitary organelles that project from the cell surface of almost all mammalian cell types during growth arrest [5]. They can be found on the surface of a large number of cells, including photoreceptor cells, kidney tubules, connective tissue, neurons, and pancreas (Figure 1b) [6]. They were first discovered in mammalian cells by Zimmermann in 1898 and first so named by Sergei Sorokin in 1968 [6].

With all attention paid to motile cilia for a long time because their functions were readily observable, the roles of primary cilia remained neglected for decades. Primary cilia were believed to be vestigial organelles with no functions and just inherited from ancestors until their significant roles in sensory reception, signalling pathways, and development were revealed. Defects in functions of primary cilia are accompanied by several human disorders (commonly known as ciliopathies). For these reasons, primary cilia have acquired more attention in research than motile cilia over the last two decades, and most recent works have further focused on studying them.

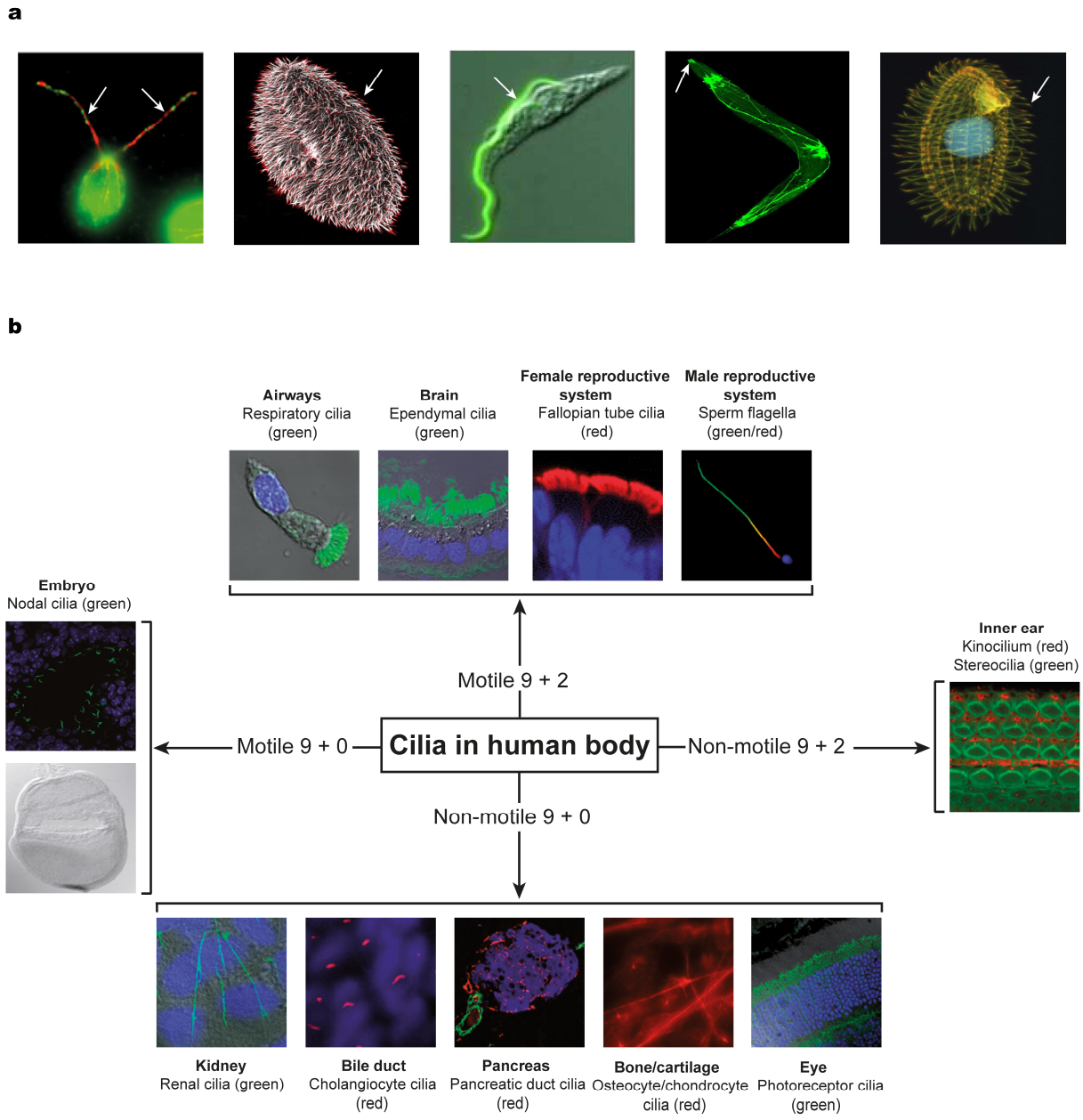

Figure 1: Ubiquity of cilia. Cilia are widely distributed organelles among organisms ranging from single-celled to humans. **(a)** Immunofluorescence images of organisms that possess cilia depicted by white arrows; from left to right: *C. reinhardtii* [7], *Paramecium tetaurelia* [8], *Trypanosoma brucei* [9], *C. elegans* [10], and *Tetrahymena thermophile* [11]. **(b)** The human body represents a striking example of functional diversity of cilia. It contains four different classes of cilia; motile 9 + 2 (top panel), motile 9 + 0 (left panel), non-motile 9 + 0 (bottom panel), and non-motile 9 + 2 (right panel) [see text for details]. All panels in **(b)** are adapted from [4] by permission from Springer Nature.

1.2 Ciliary architecture

The backbone of all cilia is the axoneme. It extends from the basal body and is surrounded by a specialized ciliary membrane. The transition zone at the base of the cilium forms a diffusion barrier that regulates the entry and exit of molecules in the organelle (Figure 2). In addition, it separates the ciliary compartments from the cell compartments. The detailed structure of the cilium is described below.

1.2.1 The ciliary axoneme

The microtubular axoneme is the core scaffold of each cilium, giving the organelle its distinct elongated shape. In motile cilia, the axoneme consists of nine peripheral doublet microtubules (MTs) and two central singlets MTs (9+2 pattern) (Figure 2, cross sections). Each doublet consists of a complete A-tubule that is made up of 13 protofilaments, and an adjacent incomplete B-tubule containing 10 protofilaments. Each protofilament is formed by the polymerization of the α- and β-tubulin dimers. The 9+2 motile cilia possess an additional MT-associated protein complexes that are required for motility, including outer dynein arms (also referred to as ODAs), inner dynein arms (IDAs), radial spokes (RS, connecting the central pair with the outer MT doublets), and nexins (flexible linkers between the adjacent microtubule doublets) (Figure 2, cross sections). Both of the axonemal dynein arms project from the A-tubule with the ODAs pointing toward the ciliary membrane and consist of two dynein heavy-chains, light and intermediate chains, and the IDAs are comprised of at least seven dynein heavy-chains facing the central pair of MTs [12, 13]. The axonemal dynein motors occupy the B-tubule and slide the adjacent microtubule doublets relative to each other, whereas the central pair apparatus with radial spokes and nexin fibres tightly regulate the MT-MT sliding process and translate it to a coherent pattern of beating [14-19]. On the other hand, primary cilia lack the central pair apparatus (9+0 arrangement), dynein and nexin arms, and radial spokes, which in turn results in loss of their motility (Figure 2, cross sections) [20]. Primary cilia possess a relatively simple structure compared to motile cilia, however, their sensory functions are indispensable. The cilia with 9+2 MTs arrangement do not always display motility. For instance, kinocilia located on apices of hair cells in inner ear possess the central pair of MTS but still lacking motility because of the absence of the accessory structures such as ODAs and nexins linkers [21, 22]. On the contrary, cilia in node cavity of mouse embryo have 9+0 pattern but are still capable of performing ciliary beating due to the presence of dynein arms [23].

1.2.2 The basal body and transition zone

The basal body (BB) is a centriole in origin and located at the ciliary base. The centriole is functionally repurposed to nucleate the formation of the primary cilium when the cell is not in division, whereas the centriole regulates the cell cycle by formation of the microtubule organizing center (MTOC) only when it is not associated with the cilium [24-26]. The BB organelle is also a microtubule-based structure consisting of an array of short nine triplet MTs (A, B, and C) (Figure 2, cross sections). While the nine outer doublet MTs (A and B) are continuous with the axonemal tubules, the C-tubule ends at beginning of the transition zone (TZ) [27].

The transition zone (TZ) is an electron dense structure that originates at the distal end of the basal body. It functions as a selective gate for the proteins destined for ciliary assembly and acts as a barrier to separate the ciliary compartment from the cytoplasm. The proximal region of the TZ encompasses a propeller-like array (also referred to as transition fibres) emanating from the B-tubules of the basal body to the periciliary membrane and prevents passive diffusion of molecules larger than 9 nm [28]. The TZ is characterized by the presence of the Y-shaped linkers locating distal to the transition fibres and projecting from the outer doublets to anchor the ciliary MTs to the ciliary membrane [29]. Moreover, these linkers are connected to a specialized structure called the ‘‘ciliary necklace’’, which consists of multiple integral strands of parallel intramembrane protein particles. It is believed that the ciliary necklace marks the beginning of the ciliary membrane [30, 31]. The TZ terminates at the distal region of Y-linkers. In 9+2 cilia, the central microtubule pair originates from the TZ. Notably, the sensory cilia of *C. elegans* possess singlet MTs, which are irrelevant to the central pair in motile cilia, in the cavity of the TZ and the axoneme.

1.2.3 The ciliary membrane and the ciliary pocket

The ciliary membrane is a sophisticated structure that encloses the axoneme and separates the ciliary compartment from the extracellular matrix (ECM) (Figure 2). The ciliary membrane is an extension of the cell membrane, however, it retains a distinct composition of its own. It is highly enriched in sterols, glycolipids, and sphingolipids [32, 33]. These molecules are known to form large platforms of lipid rafts, which interact with proteins of ciliary membrane to perform functions in signal processing and transport [34]. Some cilia exhibit an additional membrane domain called the ciliary pocket (CiPo) that is found at the ciliary base as an invagination of the plasma membrane (Figure 2) [35, 36]. It may function as a site for endocytosis and exocytosis, and a platform for cilia-associated vesicles, similar to the flagellar pocket of trypanosome [37].

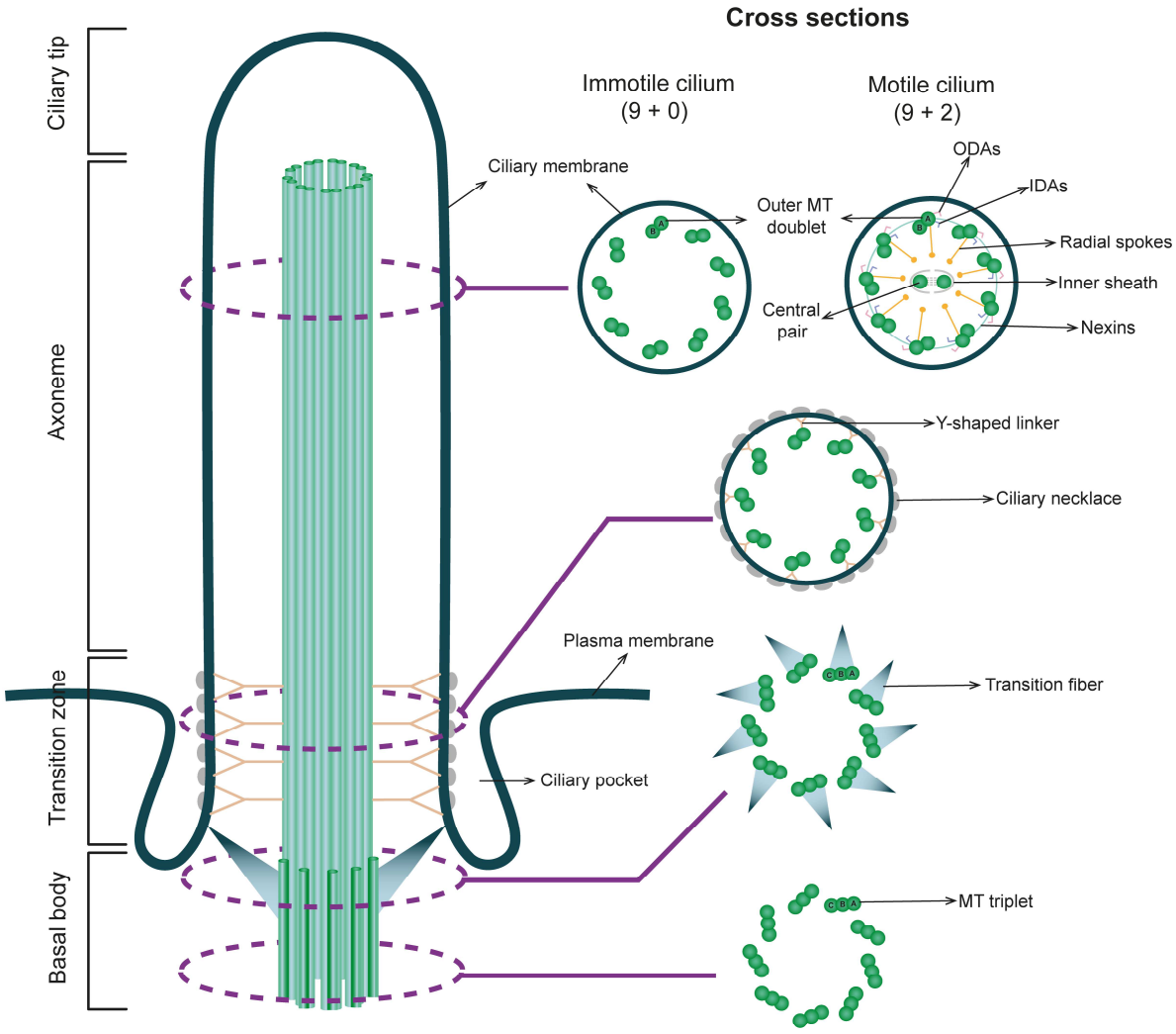

Figure 2: Cartoon representation of the ciliary ultrastructure. Left, a schematic showing the overall structure of the cilium with its functionally distinct regions. Right, cross sections depict the internal organization of the different ciliary regions.

1.3 Ciliary functions

Cilia perform a wide range of functions. Depending on their type and location, cilia can perform dynamic and static functions. Below, I discuss the most common ciliary functions.

1.3.1 Motility

Cilia were first annotated for motility properties. Motile cilia not only project from the cell surface of unicellular organisms but also from the cell surface of multicellular organisms, including mammals.

In humans, motile cilia extend from the cell surface of several cell types to perform different functions. Motile cilia emanating from the surface of epithelial cells in the respiratory system beat in a rhythmic manner to clear mucus from the airway. On the other hand, motile cilia extending from the surface of the ependymal cells lining the brain ventricles to propel the cerebrospinal fluid (CSF) that keeps a stable pressure inside the brain [38]. Motile cilia are also associated with fertility. For example, the mammalian sperm cell uses its long flagellum to propel itself through the female reproductive tract to eventually fertilize the egg, whereas motile cilia lining the female fallopian tubes beat coherently to transport the zygote from the ovary to the uterus [39].

1.3.2 Cilia in development

Nodal cilia are motile cilia present in early stages of developing embryo and play prominent roles in development. They undergo leftward rotation with a regular frequency to produce an extracellular fluid flow that is used as a developmental signal to break the left-right symmetry of the body. The exact mechanism by which the leftward flow determines the left-right asymmetry is a long standing dilemma. Interestingly, unlike other motile cilia, nodal cilia share a similar structure with primary cilia in absence of central apparatus (9+0) but they retain the dynein arms that enable them to move [38].

1.3.3 Sensory and signaling functions

Primary cilia are best-known for sensory functions. They can function as receptors that detect light in the retina, sound waves in the ear, and chemical signals in olfactory neurons of the nose [40]. They also can act as mechanosensors that sense the extracellular fluid flow in the renal tubules of the kidney and the pancreatic ducts [40]. They are known to be involved in cell signaling during development and homeostasis. This is because they possess an arsenal of signaling proteins that act as transmembrane receptors for signalling pathways such as the fundamental platelet derived growth factor receptor (PDGFRα), sonic hedgehog (SHH), Wnt singaling, and epidermal growth factor receptor (EGFR) [40].

1.4 Cilia and ciliopathies

Ciliopathies are a group of heterogeneous disorders with different pathological sequelae. They originate from deficiencies in the components of intraflagellar transport (IFT), the conserved ciliary building machinery (see section 1.6). Defects in motile cilia have long been known to be associated with human diseases. Dysfunctional cilia are found in patients with the Primary Cilia Dyskinesia (PCD) syndrome, who suffered from male/female infertility, respiratory infections, cystic kidneys,

and hydrocephalus [41, 42]. PCD is characterized by defects in the ciliary structure, including the central pair, lack of IDAs and ODAs, and the radial spokes [13]. In contrast to motile cilia, the link between primary cilia and human diseases has been perplexing and just emerged two decades ago when it was shown that mice with mutations in the Tg737 (an IFT-B subunit and the homologue of *C. reinhardtii* IFT88) develop polycystic kidney disease (PKD) and die shortly after birth [43]. Since this breakthrough till today, hundreds of studies have linked defects in primary cilia to a wide range of human diseases such as retinitis pigmentosa (RP), nephronophthisis (NPHP), Joubert syndrome (JBTS), hearing loss, Usher syndrome, Meier-Gorlin syndromes, Meckel syndrome (MKS), and Bardet-Biedl syndrome (BBS), to name but a few [44].

1.5 Ciliary length control

Due to their simple geometry and well documented kinetics, the flagella of *C. reinhardtii* are serving as a role model organelle for researchers of all disciplines who are interested in studying how cells build themselves and how they control the size of their cellular organelles. Controlling flagella length is important for cells to preform proper physiological functions, as mutants with longer flagella display low beating frequencies and decreased swimming velocities, and mutants with unequal length flagella move around in circles [45]. It is well known that IFT is the key process of controlling the flagellar length by relentlessly transporting the tubulin building blocks of the axoneme to the flagellar tip and the turnover products to the flagellar base by the help of kinesin-2 and dynein-2 motors, respectively. Previous cell imaging studies have shown that the rate of IFT entering the flagellum (also referred to as IFT injection rate) is negatively regulated with the length of the flagellum, but how cells sense the flagellar length and how the flagellum retains its same steady-state length are unknown [46].

Although there exist a series of mathematical models for length control, the balance point is by far the most consensus model that can explain the experimental results (Figure 3). The balance point model is based on three different parameters: first, the quantity of intraflagellar transport machinery as a function of length, second, the variation of flagellar length as a function of flagellar number, and third, the rate of flagellar growth as a function of length. This model proposes that the flagellar length control is governed by the continuous balance between the flagellar assembly and disassembly rates [47]. It shows that the assembly rate is length dependent, whereas the disassembly rate is length independent. Therefore, the steady-state length can be achieved by the point at which the two rates come into balance (Figure 3).

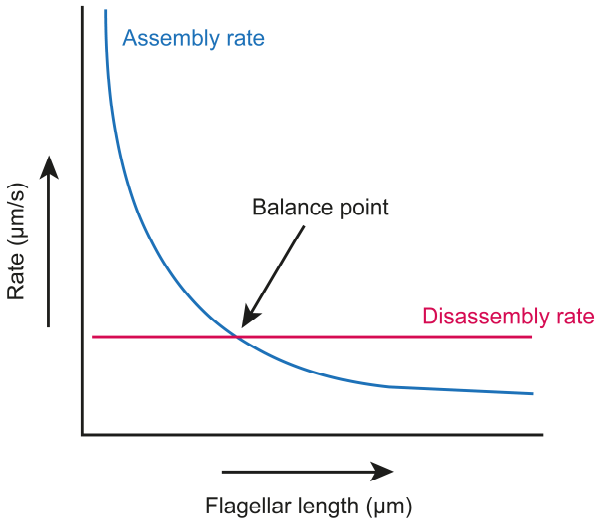

Figure 3: The balance point model for flagellar length control. The assembly rate (blue curve) and the disassembly rate (red curve) as a function of length. The flagellum reaches a steady-state length only when the decelerating assembly rate intersects with the constant disassembly rate [47].

1.6 Cilia biogenesis: IntraFlagellar Transport (IFT) and its components

Although cilia harbor several hundreds of proteins (~652 proteins) as formerly shown in mass spectrometry (MS) analyses, they lack the protein synthesis machinery (i.e., ribosomes) for synthesizing these proteins [48]. Therefore, it is conceivable that cilia rely on an active transport mechanism for maintaining their integrity and localizing proteins of interest to cilia. This mechanism is called the intraflagellar transport (IFT) that was first observed by Keith G. Kozminski in 1993 as moving particles between the axoneme and the flagellar membrane (Figure 4, top panel) of the paralyzed green algae *C. reinhardtii* using differential interference contrast microscopy (DIC) [49]. These particles were moving from the ciliary base to the ciliary tip (anterograde transport) at a rate of 2 µm/s and from the ciliary tip to the ciliary base (retrograde transport) at a rate of 3.5 µm/s [49, 50]. This bidirectional movement of particles (IFT) was then observed in many other organisms, including *C. elegans* [51, 52]. Following its discovery, biochemical studies have showed that depending on ionic strength, IFT can dissociate into two main complexes: IFT-A and IFT-B. Moreover, further increase of ionic strength leads to dissociation of IFT-B complex into IFT-B peripheral complex and IFT-B core complex [53, 54]. The IFT-A and the IFT-B complexes collectively

consist of at least 22 subunits, which were first named according to their molecular weights on SDS gel (Supplementary table 1). The IFT subunits are highly conserved among ciliated eukaryotic organisms, and contain protein-protein interaction domains such as β-propellers, tetratricopeptide repeats (TPRs), and coiled-coils [55].

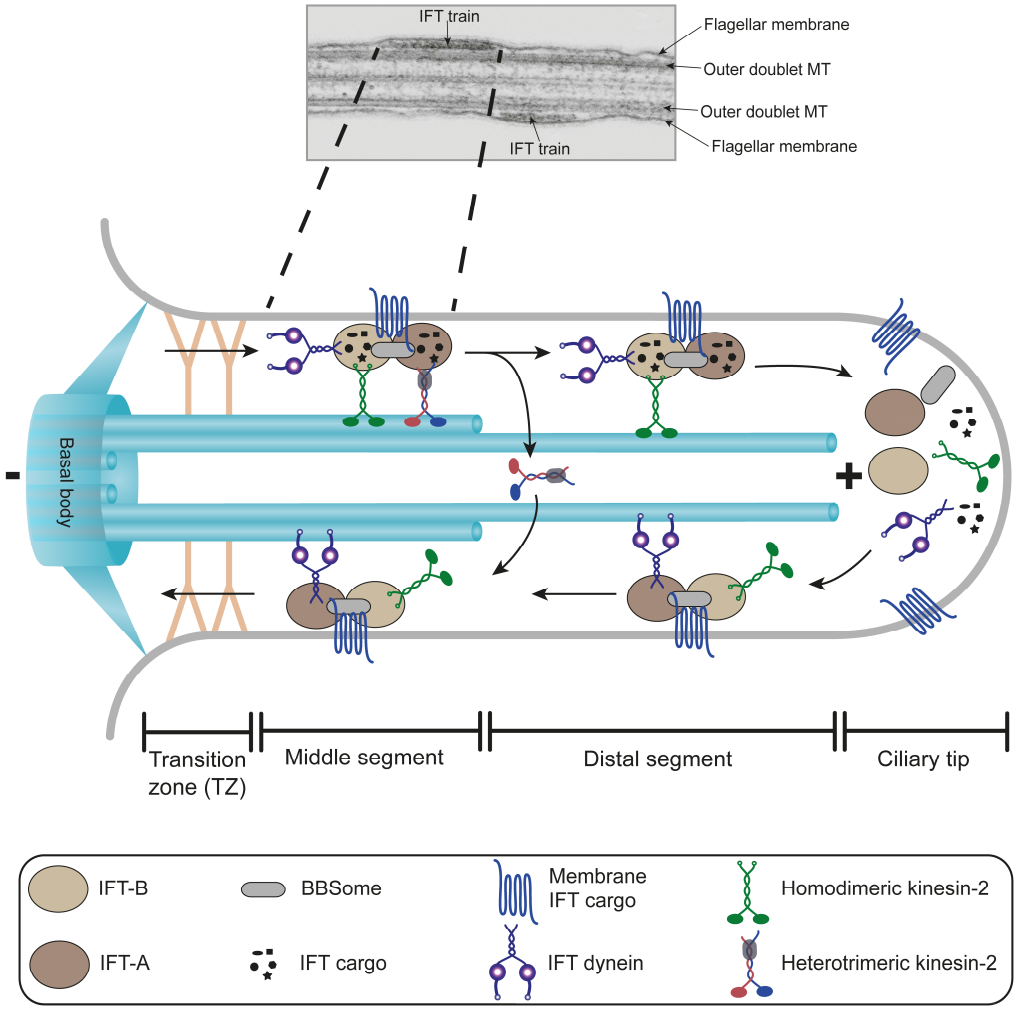

Figure 4: Overview of the IFT pathway in *C. elegans*. The upper image (adapted from [56]) is an EM of a longitudinal ultrathin section through a *C. reinhardtii* flagellum showing the anterograde and retrograde IFT trains (upper and lower IFT trains, respectively) as an electron-dense material squeezed between the flagellar membrane and the outer doublet MT. The lower panel is a schematic overview of the anterograde IFT (base to tip) and the retrograde IFT (tip to base) in the sensory cilia of *C. elegans*. While anterograde trains are loaded with soluble cargo proteins, ciliary precursors, membrane cargos, and the passenger dynein-2 motor, retrograde trains are loaded with turnover products and the passenger OSM-3 motor.

The universally conserved IFT machinery builds almost all cilia, with the exception of the flagellum of the mammalian sperm [57]. The process of IFT is highly regulated, and occurs at multiple stages (Figure 4, bottom panel). At the ciliary base the IFT-A and IFT-B complexes form trains presumably by the help of the BBSome complex. Other cargos (membrane proteins, inactive retrograde dynein-2 motor, and ciliary precursors) are loaded onto IFT trains. Once trains are assembled and loaded, the heterotrimeric kinesin-2 motor navigates trains through the transition zone, which is characterized by Y-shaped linkers. Following their selective entry, IFT trains are transported along the middle segment by the heterotrimeric and homodimeric kinesin-2 motors at an intermediate speed. Before the end of the middle segment, the heterotrimeric kinesin-2 motor gradually dissociates from IFT trains and hands over the transport to the homodimeric kinesin-2 motor to drive the anterograde IFT trains exclusively along the distal segment. Once IFT trains reach to the ciliary tip, they undergo remodeling, cargos are unloaded, the homodimeric kinesin-2 is inactivated, and the retrograde IFT dynein motor is activated to drive IFT trains back to the ciliary base. On the way back to the base along the middle segment, the homodimeric kinesin-2 is gradually unloaded and the heterotrimeric kinesin-2 is picked up for recycling at the base where trains disassembly takes place [58, 59]. Previous biochemical and genetic studies have revealed that the IFT machinery is comprised of different categories, including the IFT motors, the IFT particles, and the BBSome complex (see below).

1.6.1 IFT motors

The anterograde and retrograde IFT movements along the ciliary axoneme are powered by the kinesin-2 and dynein-2 motors, respectively. The kinesin-2 family comprises two forms of kinesin motors: the heterotrimeric kinesin-2 (kinesin-II) and the homodimeric kinesin-2 (also referred to as OSM-3 in *C. elegans* and KIF-17 in mammals), which are known to function as anterograde IFT motors.

Kinesin-II: kinesin-II holoenzyme consists of two motor subunits termed KLP-20 and KLP-11 (homologues of FLA-10 and FLA-8 in *C. reinhardtii*, respectively) and a non-motor accessory subunit named kinesin-associated protein (KAP-1, the homologue of FLA-3 in *C. reinhardtii*). Each motor subunit is composed of an N-terminal head domain (motor domain) with an ATPase activity, a middle domain (stalk) consisting of coiled-coil to aid in heterodimerization of the two motor subunits, and a C-terminal cargo binding domain (tail), where the KAP-1 subunit binds [60]. The KAP-1 subunit is a globular protein containing an armadillo repeats needed for protein-protein interactions, a tyrosine–rich acidic tail, and a binding site within the C-terminal region for the heterodimer KLP-20/KLP-11

[61, 62]. Kinesin-II functions as a canonical anterograde motor in many organisms, including *C. reinhardtii*, *C. elegans*, sea urchin, mouse, and *Drosophila* [63-66]. It solely drives anterograde IFT trains along the flagellar axoneme of *C. reinhardtii* at a rate of 2 µm/s, which is also supported by in vitro studies [67, 68]. In *C. elegans*, the KAP-1 subunit is proposed to function as an adaptor protein bridging the heterodimer KLP-11/KLP-20 motor with the IFT particles. It is also thought that the heterodimerization of KLP-11 and KLP-20 polypeptides is necessary for an efficient binding to the KAP-1 subunit [69, 70]. Recently, the KAP-1 subunit has been proposed to activate the heterodimer FLA-8/FLA-10 of *C. reinhardtii* (See section 3 for details) [68].

OSM-3: OSM-3 exists as a homodimeric motor. It consists of an N-terminal catalytic motor domain (head) attached to a C-terminal tail domain by a homodimeric coiled-coil stalk. Unlike kinesin-II motor, OSM-3 motor lacks accessory subunits. In *C. elegans* sensory cilia, the fast moving OSM-3 motor (~1.3 µm/s) functions redundantly with the slow moving kinesin-II motor (~0.5 µm/s) to transport the IFT trains along the middle segment at an intermediate speed of ~0.7 µm/s and then the OSM-3 motor solely transports the trains along the distal segment at its own pace of ~1.3 µm/s [67, 69, 71]. While the OSM-3 motor can build the full-length sensory cilium of *C. elegans* in the absence of the kinesin-II motor, the kinesin-II motor is only able to build the middle segment in the absence of the OSM-3 motor. In the absence of both motors, cilia are not built [67, 72]. The presence of accessory kinesins in *C. elegans* is not only restricted to OSM-3 motor since there exist numerous accessory kinesins, some of which play roles in cilium biogenesis by transporting specific ion channels, receptors, and signaling molecules to cilia. For example, the kinesin-3 family member KLP-6 is required for modulating male mating behavior and transporting polycystin ion channels to cilia membranes in the nematode [60, 63, 67, 73].

Intriguingly, mammalian primary cilia contain two types of accessory motors, namely the heterotrimeric KIF3A/KIF3C/KAP and the homodimeric KIF-17 (OSM-3 homologue) in addition to the canonical KIF3A/KIF3B/KAP (homologue of the *C. reinhardtii* FLA-10/FLA-8/FLA-3, respectively) [74, 75]. In contrast to the functionally operating accessory OSM-3 motor of *C. elegans*, the mammalian KIF3A/KIF3C/KAP and KIF-17 are unessential motors for building cilia. This is based on the observation that in the absence of the KIF3A/KIF3B/KAP, neither the KIF3A/KIF3C/KAP motor nor the KIF-17 motor were able to build and maintain the cilium, indicating that the KIF3A/KIF3B/KAP is the sole fundamental motor for cilia assembly and maintenance [74]. In mammalian cells, KIF-17 motor is a cargo that is associated with IFT-B complex during IFT. The role of KIF-17 in ciliogenesis is poorly understood and so far there is no clue that KIF-17 functions directly in IFT like OSM-3 [67, 76]. This passive KIF-17 motor is not to be confused with the active KIF-17

motor that is spatially-located in the mouse brain. The neuronal KIF-17 is believed to exist as a homodimer and carries NR2B-containing vesicles toward the plus ends of MTs with an average velocity of 0.8-1.2 µm/s [77]. However, in zebrafish, KIF-17 is crucial for formation of outer segments of photoreceptors, which are modified primary cilia [78, 79].

Dynein-2: dynein motors are large multi-subunit macromolecular complexes. They are classified into three major classes: the cytoplasmic dynein-1 functions in intracellular transport, the axonemal dynein is responsible for ciliary beating, and the ciliary dynein-2 [80]. Dynein-2 is a minus-end directed microtubule motor and the canonical motor for the retrograde IFT. During the anterograde transport, dynein-2 motor is transported to the ciliary tip in an inhibited state as a cargo. At the ciliary tip, dynein-2 motor restructures to shift to an active state driving IFT trains back to the ciliary base along the A-tubules of the axoneme [81]. The conception that dynein-2 functions as a retrograde motor came from studies in *Chlamydomonas* and *C. elegans* showing that mutations in genes encoding CHE-3, DLC-1, and XBX-1 subunits of dynein-2 motor lead to assembly of short cilia containing large aggregations of IFT particles due to deterioration of retrograde transport in these cilia [17, 63, 82]. Subsequent studies in mammals have demonstrated that mutations in the dynein heavy chain gene DYNC2H1 (CHE-3) generate stunted mutant cilia similar to those observed in *Chlamydomonas* DHC1b (CHE-3) mutants [17, 82]. These results pinpoint the conserved roles of dynein-2 motor in retrograde transport. Finally, in addition to the biphasic anterograde transport in *C. elegans* that is carried out by the concerted movement of the kinesin-2 motors, dynein-2 is shown to drive retrograde IFT trains back to the ciliary base in a triphasic manner: it speeds up along the distal segment reaching the maximum velocity approximately in the middle segment and eventually slows down near to the ciliary base [83].

Dynein-2 motor complex consists of four different polypeptide chains: two heavy chains (CHE-3) belong to the AAA+ family of ATPases, a light intermediate chain termed XBX-1, and several light chains, including DLC-1 and putative WD repeats [63]. Each CHE-3 chain consists of motor and tail domains. The motor domain encompasses the main catalytic core that is a ring of six AAA+ modules from which two main structures project into two different directions: the first structure is a coiled-coil stalk extending antiparallel from the ring to form a microtubule binding domain at the end of the C-terminal domain and the second structure extending in the opposite side to form the N-terminal tail domain that is connected to the ring via a mechanical linker [80, 84]. The remaining structures of dynein, including intermediate and light chains, and WD repeats as well as presumably cargo proteins bind to the tail domain [80, 84].

1.6.2 The IFT-A complex

Owing to simplification, the *C. elegans* nomenclature of IFT subunits is used henceforth, unless it is necessary in some positions the *C. reinhardtii* nomenclature will be additionally stated in parentheses. See the supplementary table 1 for the nomenclature of IFT proteins.

Although the IFT-A complex consists of few subunits, much less information is available on its architecture and the specific functions of its subunits. The IFT-A complex consists of six subunits, namely DYF-2, CHE-11, DAF-10, ZK328.7, IFTA-1, and IFT-43 (Figure 5). It is further classified into core and peripheral complexes [85]. The core complex includes the DYF-2, CHE-11, and DAF-10 subunits, whereas the rest of the subunits (ZK328.7, IFTA-1, and IFT-43) are considered the peripheral complex (Figure 5) [85, 86]. With the exception of the IFT-43 subunit, the IFT-A subunits are large size proteins with a molecular weight of more than 100 kDa.

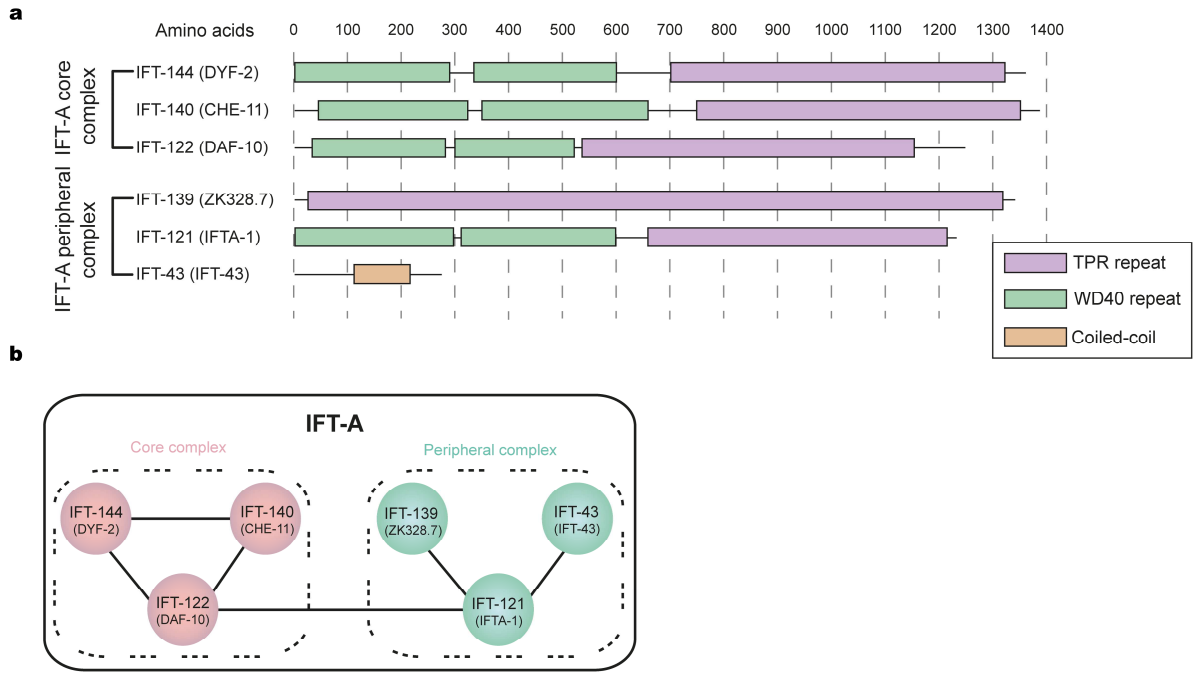

Figure 5: Architecture of the IFT-A complex. (a) Domain architecture of the identified IFT-A subunits. **(b)** The interaction map of the IFT-A complex. The core and peripheral subunits known to form stable complex are color coded and surrounded by dashed squares. Direct interactions are depicted by solid black lines. The corresponding nomenclature of the IFT-A subunits in *C. elegans* is included in parentheses.

Four subunits of the IFT-A complex (DYF-2, CHE-11, DAF-10, and IFTA-1) display an evolutionary relationship with members of coat protein complex I (COPI) by sharing similarities in the domain

architecture containing an N-terminal WD40 β-propellers and a C-terminal α-solenoid TPR repeats (Figure 5a) [55, 87]. In *C. reinhardtii*, CHE-11 and DAF-10, DYF-2 and CHE-11, and DYF-2 and DAF-10 were reported to form direct interactions (Figure 5b) [86]. Furthermore, a number of additional direct interactions were detected between the peripheral subunits as well as the peripheral and core subunits using different biochemical approaches. For example, IFTA-1 was shown to interact with both IFT-43 and ZK328.7, and DAF-10 interacts with IFTA-1 (Figure 5b) [86]. In *C. elegans*, the IFT-A complex is required for the anterograde IFT in addition to its role in retrograde transport [67, 71]. This in fact is consistent with the previous findings showing that SEC analysis of extracts from *C. reinhardtii* flagella resulted in co-elution of IFT-A complex, dynein-2, and kinesin-II in the same fractions, but not IFT-B, suggesting that IFT-A complex play a role in anterograde IFT as well as retrograde IFT [88].

1.6.3 The IFT-B complex

In contrast to its counterpart IFT-A complex, the IFT-B complex consists of many more subunits (Figure 6). Earlier studies in *C. reinhardtii* revealed that increasing the ionic strength to 300 mM NaCl results in the dissociation of the IFT-B complex into IFT-B core complex consisting of six subunits (IFT-27, DYF-6, OSM-6, OSM-5, IFT-74, and IFT-81) and IFT-B peripheral complex consisting of four subunits (Y110A7A.20, OSM-1, CHE-2, and CHE-13) [89]. Additional core (DYF-1, IFTA-2, and IFT-25) and peripheral subunits (DYF-11, DYF-3, and DYF-13) have been identified in subsequent studies using different model organisms, bringing the total number of IFT-B subunits to 16 subunits (Figure 6) [90]. Interestingly, the homologues of IFT-25 and IFT-27 are absent in *C. elegans*, whereas five core subunits, namely IFT-25, 27, 22, 81, and 74 are missing in *Drosophila*, indicating that these subunits are involved in functions other than the canonical IFT (e.g., signalling) [91]. Initial findings into subunit interactions within the context of IFT-B complex brought about a significant improvement in the recombinant reconstitution and biochemical characterization of IFT-B complexes, which in turn led to a better understanding of the high-resolution structure of IFT subunits. Recently, it was shown that the *C. reinhardtii* IFT-B core complex is stable under salt concentrations of > 2 M, whereas the IFT-B peripheral complex stays intact up to 1 M salt concentration with the exception of the salt labile OSM-1 that dissociates from the complex at ~200 mM salt concentration, indicating that the subunits assemble together via a substantial hydrophobic interactions [90, 92]. Although much information is available on the structure and the interaction map of the IFT-B complex (Figure 6a, b, respectively), the specific contributions of its subunits in ciliogenesis are still cryptic. This is because the subunits form networks of interdependent protein-protein interactions. Deletion of one subunit causes complex disassembly that eventually leads to

formation of general dysfunctional phenotypes, making it impossible to pinpoint the specific functions of the missing subunit in IFT. For example, OSM-6 is known to be the most prominent subunit for interdependent protein-protein interactions. It is located at the heart of the IFT-B complex and associates with at least five other IFT-B proteins, therefore mutations in the gene encoding the *Chlamydomonas* OSM-6 subunit results in loss of flagella and destabilization of several IFT-B core components [90, 93].

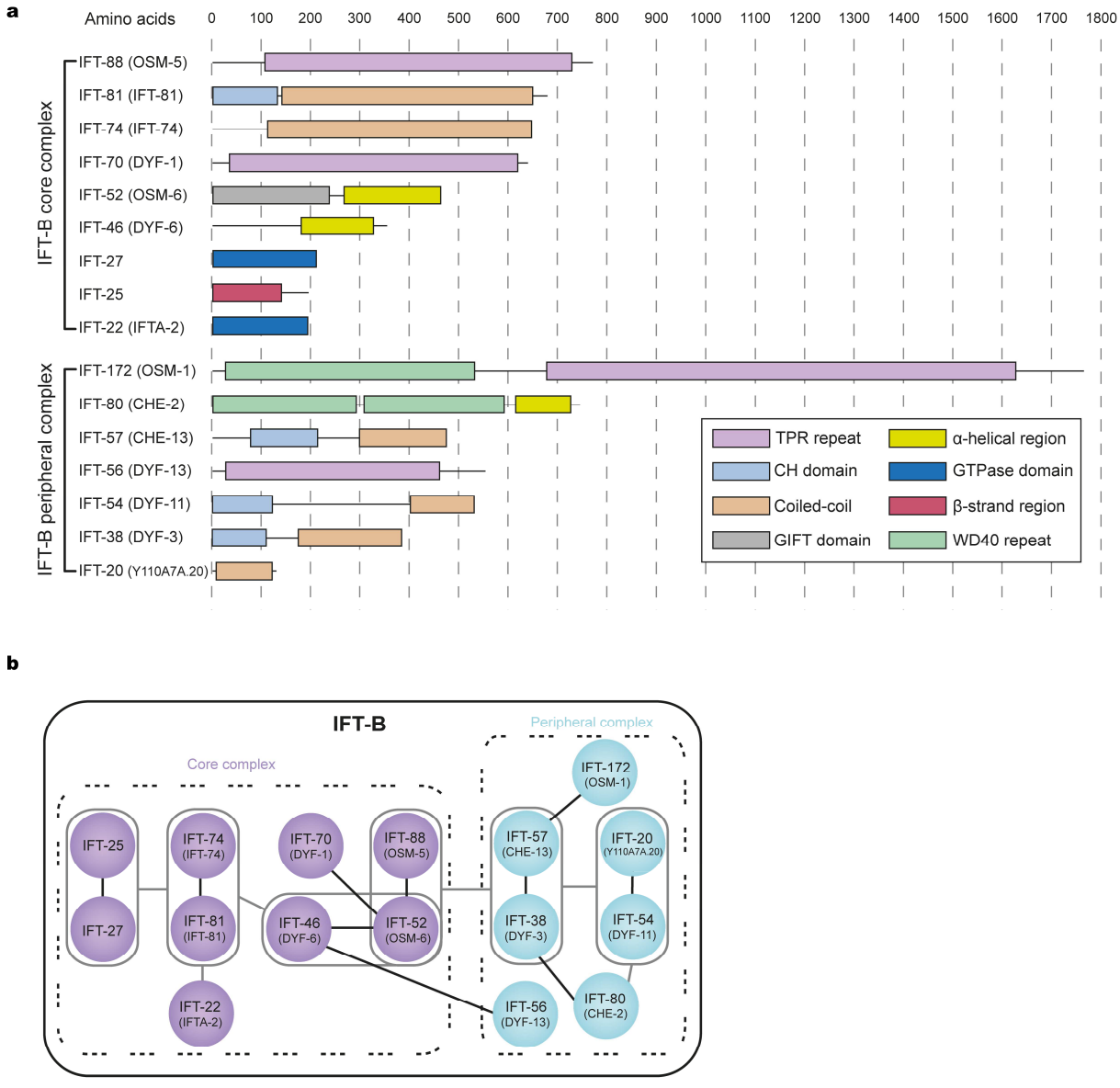

Figure 6: Schematic architecture of the IFT-B Complex. (a) Domain architecture of the IFT-B subunits showing that the majority of the subunits contain protein-protein interactions motifs such as coiled-coil, WD40 repeats, and TPRs. IFT-27 and IFT-25 subunits of the IFT-B core complex in *C. reinhardtii* are missing in *C. elegans*. **(b)** Interactions between the subunits of the IFT-B complex that

have been identified to date. The core and peripheral subunits known to form stable complexes are color coded and surrounded by dashed squares. Direct interactions are depicted by solid lines. The IFT-57/IFT-38 and IFT-88/IFT-52 heterodimers form an interaction interface connecting the IFT-B peripheral complex with the IFT-B core complex, respectively. IFT-22 binds to IFT-74/IFT-81 heterodimer. IFT-25/IFT-27 heterodimer interacts with IFT-74/IFT-81 heterodimer. IFT-46/IFT-52 heterodimer interacts with IFT-74/IFT-81 heterodimer. IFT-57/IFT-38 heterodimer binds to IFT-54/IFT-20 heterodimer. IFT-80 binds to IFT-54/IFT-20 and IFT-57/IFT-38 heterodimers. The corresponding nomenclature of subunits in *C. elegans* is included in parentheses.

1.6.4 The BBSome complex

In humans, dysfunctional BBSome is the main causative of a rare genetic disorder termed Bardet-Biedl syndrome (BBS) that is accompanied by clinical manifestations, including retinal degeneration, obesity, polydactyly, and kidney failure [94, 95]. In contrast to IFT-A and IFT-B complexes, the BBSome complex is dispensable for cilia assembly. It is considered to be a cargo that couples IFT trains with ciliary signaling proteins [94]. Dysfunctions in BBSome components lead to accumulation or depletion of several signaling subunits from cilia [96]. For example, the ARL6/BBS3 and LZTFL1/BBS17 mutant cells accumulate GPCRs (GPR161), Smo, and Gli2 in their cilia [90]. A number of direct interactions between IFT particles and BBSome subunits have been observed in different organisms. In *C. reinhardtii*, the interaction between the IFTA-2 (IFT-22) subunit and the BBS3/ARL6 subunit is required for the recruitment of the BBSome complex to the basal body [97]. In *C. elegans*, the BBS-1 binds to the IFT-A core subunit DYF-2 (IFT-144) to stabilize the interaction between the IFT complex and the BBSome complex [98]. Abolishing this interaction by hypomorphic mutations in DYF-2 or BBS-1 results in accumulation of BBSome and IFT-B components at the ciliary base and the ciliary tip, respectively [98]. Moreover, in *C. elegans*, the BBS-7 and BBS-8 subunits are responsible for stabilizing the interaction between the IFT-A and IFT-B complexes. Mutations in BBS-7 and BBS-8 subunits lead to dissociation of IFT particles into IFT-A and IFT-B complexes, which are moved by kinesin-II and OSM-3 motors, respectively, along the ciliary axoneme [69]. The nomenclature and the sizes of the subunits of the BBSome complex are included in the supplementary table 1.

1.7 Regulation of IFT motors

1.7.1 Regulation of kinesin-2 motors

Since cilia lack an internal protein synthesis machinery, activities of kinesin-2 motors must be regulated to ensure safe delivery of motors from their site of synthesis inside the cell to the cilium, the only place where kinesin-2 motors function. Kinesin-2 motors display an intrinsic dual

autoinhibitory mechanisms to probably gain a full control of their activities. The first mechanism is necessary to prevent coordinated stepping of the two motor domains during anterograde transport, whereas the second mechanism is required to prevent premature binding to microtubules, nucleotide exchange and hydrolysis, and cargo association [99]. In the second mechanism, kinesin-2 motors adopt a folded, compact conformation enabling the tail domain to come in contact with the motor domain (Figure 7 left), which results in shutting down the ATPase catalytic activity of the motors. This mechanism is required to guarantee a safe switch from anterograde to retrograde transport and to transport inactive kinesin-2 motors as passengers back to the ciliary base on dynein-2-driven retrograde trains. Relief of autoinhibition can be achieved either artificially by introducing a point mutation in the kink region resulting in an extended conformation of the motor that is capable of efficient movement or naturally as they exist in the cilium by a competitive binding of a cargo to the motor's tail (Figure 7 right and middle, respectively) [100]. For more details, see part I.

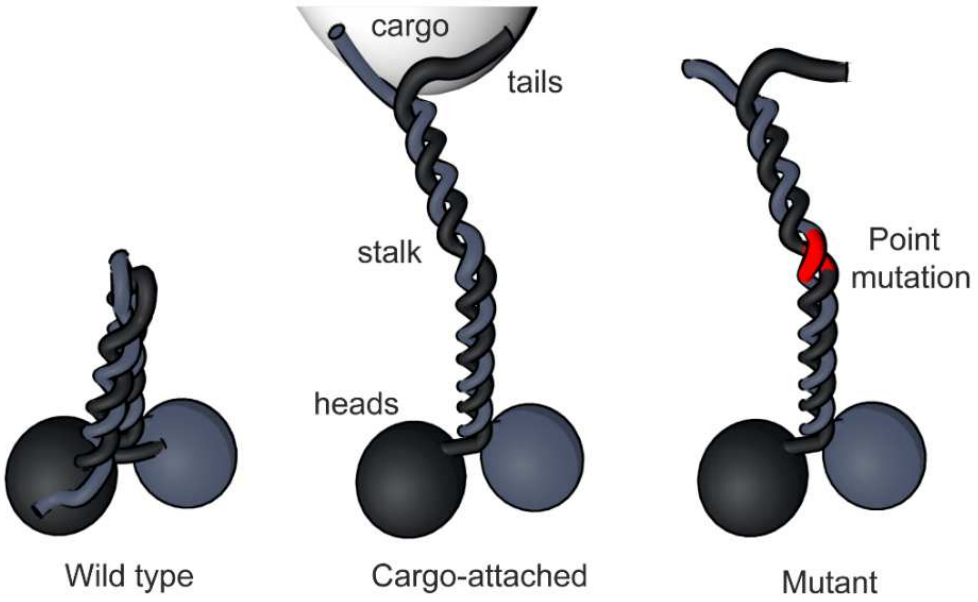

Figure 7: Schematic representation of different regulation mechanisms of kinesin-2 motor. An overview showing the autoinhibited state of wild type kinesin-2 motor (left). The motor can be activated either by cargo binding to the tail region (middle) or by a mutation in the stalk (right). The point mutation is depicted in red. This figure is courtesy of Willi L. Stepp.

1.7.2 Regulation of dynein-2 motors

During anterograde transport, dynein-2 motor exists in an inactive state and travels as a passenger on anterograde IFT trains to the ciliary tip to avoid entering a tug-of-war with the oppositely directed kinesin-2 motors. Recent studies in *C. reinhardtii* had shed some lights on the underlying molecular

mechanisms of dynein-2 inhibition and activation. During anterograde transport, dynein-2 inhibition is achieved by two concurrent mechanisms: the first mechanism involves reconfiguration of dynein-2 subunits, including trapping its linkers, stalks crossing, and closely opposing the two AAA+ rings (Figure 8a). The second mechanism is a reorientation of dynein-2 domains, in which the tail is pointed toward MTs facing the ciliary base and the motor domain faces the ciliary membrane with its stalks oriented toward the ciliary tip [101]. These two mechanisms assure that the dynein-2 motor is switched off during anterograde transport by preventing it from premature engaging with MTs. Once IFT trains reach the ciliary tip, somehow the dynein-2 motor undergoes restructuring and repositioning modifications by freeing its linkers and stalks, releasing the motor's activity allowing it to power the retrograde transport. A subsequent elegant cryo-EM study showed that the autoinhibited dynein-2 motor displays an asymmetric conformation in its heavy chain tails, which is achieved through the use of different non-motor subunits. While one of the motor's heavy chain tails is straight, the other heavy chain tail folds into a zig-zag shape to match the periodicity of anterograde IFT-B trains (Figure 8b, c) [80].

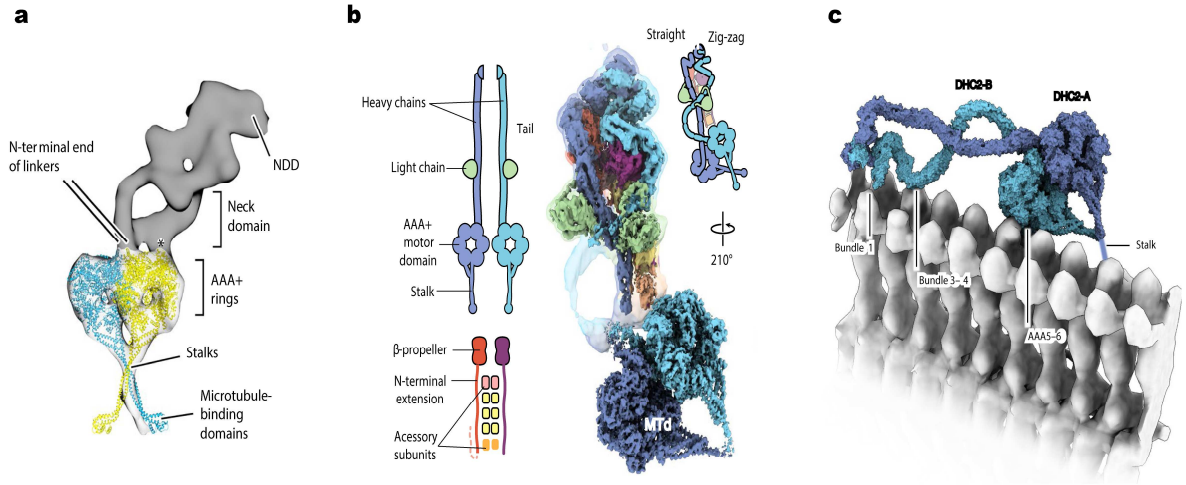

Figure 8: Dynein autoinhibition regulation. (a) Fitting of an atomic model to a single dynein motor showing the autoinhibition of dynein via a stacking of the AAA+ rings and a crossing of the stalks [101]. **(b)** Overview showing the dynein-2 subunits (left). Cryo-EM reconstitution of the dynein showing the asymmetric conformation in the heavy chain tails (right) [80]. **(C)** Docking of dynein-2 complex into a tomogram of IFT-B train. Note how the zig-zag tail of the heavy chain (DCH2-B) matches the periodicity of IFT-B train [80]. This figure is reprinted by permission from Springer Nature.

1.8 Aims of the thesis

Motile cilia have acquired tremendous attention in the past decades because their functions were readily observable. This, of course, came at the cost of their immotile cousins or the so-called sensory cilia. Despite the fact that every single cell in the human body possesses a solitary sensory cilium, the functions of sensory cilia were obscure for many decades. Sensory cilia were first thought to be vestigial structures that we just inherited from our ancestors without any apparent functions, until the onset of the 21st century when they underwent a renaissance and moved to the position of importance. Research breakthrough had revealed the crucial roles of the sensory cilia in many aspects of human health, development, and diseases (ciliopathies).

To develop a better understanding about the functions of sensory cilia in vivo, the regulatory mechanisms of the ciliary building machinery IFT needs to be dissected at a molecular level in vitro. It is clear that revealing the roles of the individual IFT subunits is the key to the understanding of the IFT regulation mechanisms. This, however, is proven to be challenging in vivo because knockout or knockdown of an IFT subunit leads to formation of complex and common phenotypes. More detailed information about the specific functions of individual IFT subunits have been obtained from in vitro reconstitution studies using recombinant IFT subunits.

Since IFT initial discovery in 1993, the two most fundamental questions that have perplexed researchers in the field have been: first, how kinesin-2 motors are regulated for efficient IFT? In part I, we therefore deployed a bottom-up reconstitution approach to investigate how the kinesin-2 motor OSM-3 is recruited to IFT trains and what are the factors essential for its activation to drive anterograde IFT trains in vivo. Answering this question using a step-wise reconstitution allowed us to assemble the first functional multi-component IFT complex that is deployed in the sensory cilia of *C. elegans* and enabled us to incorporate previous in vivo results into a general molecular mechanism. Second, what are the underlying molecular mechanisms of regulated assembly and remodeling of IFT trains in vivo? Our in vitro preliminary data in part II showing the phosphorylation-dependent oligomerization and disassembly of IFT subunits hold the promise to provide the first novel concepts of the regulatory roles of the DYF-5 and DYF-18 kinases into the spatially-regulated processes of assembly and restructuring of IFT trains in vivo. The success of the proposal in part II will pave the way for further work on understanding how phosphorylation-dependent processes modify the interaction landscape of the IFT subunits in other eukaryotic organisms.

Part I

2 Results

2.1 Assembly of the first kinesin-2-IFT complex

As mentioned before in section 1.6.3, the IFT-B complex of *C. reinhardtii* is divided into IFT-B core complex and IFT-B peripheral complex depending on the salt concentration [89, 90]. While the core complex consists of nine subunits (IFT-74, IFT-81, IFT-27, IFT-25, IFTA-2, DYF-1, OSM-5, OSM-6, and DYF-6) (Figure 9), the peripheral complex is composed of seven subunits (DYF-13, CHE-2, OSM-1, DYF-11, DYF-3, CHE-13, and Y110A7A.20) (Figure 6) [90]. Interestingly, the IFT-25 and IFT-27 subunits are present in the IFT-B core complex of *C. reinhardtii* but not in *C. elegans* [91]. Initial findings in *C. reinhardtii* brought about a significant improvement in the recombinant reconstitution and biochemical characterization of the IFT-B complexes, which in turn led to a better understanding of the whole architecture of IFT.

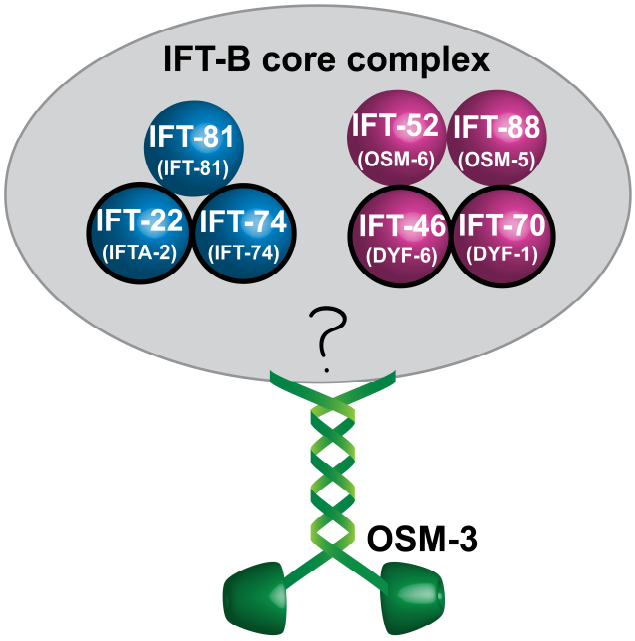

Figure 9: Schematic representation of the subunits of the IFT-B core complex and their proposed assembly in vitro along with the homodimeric OSM-3 motor. Overview of the IFT-B core complex from *C. elegans* (corresponding nomenclature of the subunits in *C. elegans* is shown in parentheses). Subunits known to form complexes in *C. reinhardtii* are color-coded. The OSM-3 is shown in green. The subunits that are proposed to interfere with OSM-3 function in vivo are highlighted with black circles.

Dissecting specific functions of individual IFT-B subunits is challenging in vivo due to the fact that the subunits are known to form networks of intermolecular interactions, making them dependent on each other for stabilization. Deletion or mutation of an individual subunit in vivo results in severe ciliary phenotypes, which in turn compromises the analysis of the regulatory roles of the missing subunit in IFT.

To develop a thorough molecular understanding of the convoluted IFT machinery in vivo, here we used a bottom-up in vitro reconstitution approach to dissect the OSM-3-IFT-B complex that is deployed in the sensory cilia of *C. elegans*. Loss of function in many IFT-B subunits has been proposed to interfere with OSM-3 function in vivo, and many of these subunits have been shown to be part of the IFT-B core complex (Figure 9) [69, 102-105].

2.1.1 Purification and co-expression assays of the IFT-B core subunits

Guided by the previous finding in *C. reinhardtii*, we sought to assemble the presumptive IFT-B core complexes of *C. elegans* using the wild-type, full-length subunits. To this end, the subunits were first checked for their expression using the Sf9 baculovirus system (see section 8.3.3 in methods part). As shown in Figure 10, all proteins can be recombinantly synthesized with satisfying expression levels. Subsequently, preliminary co-expression experiments were carried out to systematically probe the intermolecular interactions between the Flag-tagged and the untagged IFT-B core subunits. In these experiments, the Flag-tagged IFT-74 co-precipitated the untagged IFT-81 and IFTA-2 subunits (Figure 10 right), and the Flag-tagged OSM-5 co-precipitated the untagged DYF-1, DYF-6, and OSM-6 subunits (Figure 10 left), suggesting that the subunits interact directly and might be able to assemble together in complexes.

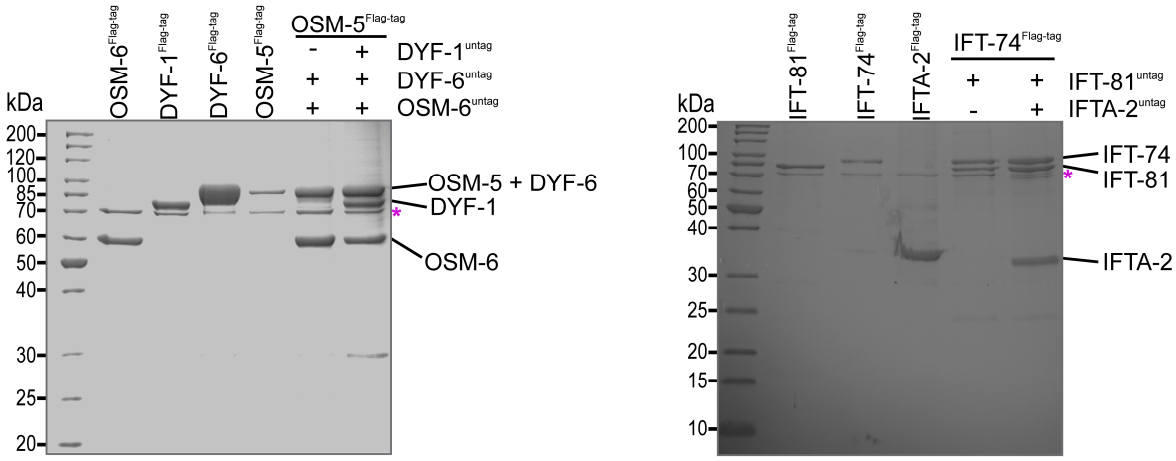

Figure 10: Pull-down assays of the IFT-B core subunits. The SDS-PAGE gels show that the untagged IFT-81 and IFTA-2 subunits are pulled down with the Flag-tagged IFT-74 subunit (the two rightmost lanes in the right gel), and the Flag-tagged OSM-5 subunit pulls down the untagged OSM-6, DYF-6, and DYF-1 subunits (the two rightmost lanes in the left gel). The molecular weight ladder (kDa) is shown on the left of the gels. The following lanes show the single expression of the respective subunits that are used in the co-expression experiments as a size control. Asterisks indicate the HSP70 protein band.

Since there exist examples of interactions between IFT subunits that were later proven to be non-specific bindings (see the following section), it is therefore plausible to think that the interactions showed in pull-down experiments might be false positive results caused by non-specific interactions between the used proteins [90, 106]. We therefore made use of size-exclusion chromatography that was coupled to multiple-angle light scattering (SEC-MALS) to further characterize the co-expression results biochemically, and assess complex formation by the subunits.

2.1.2 The IF-B core subunits IFT-74 and IFT-81 form a heterodimer

In addition to its interaction with the IFT-74 subunit, the IFT-81 subunit has been proposed to self-assemble into a homodimer in yeast two-hybrid assays, suggesting the existence of the IFT-71-81-81-74 heterotetrameric complex [89]. However, this result could not be reproduced in subsequent studies where it was shown that the recombinantly expressed IFT-B core subunits (IFT-88/81/74/70/52/46/27/25/22) of *C. reinhardtii* form a nonameric complex containing one copy of each protein [93, 107]. To assess whether the *C. elegans* IFT-81 subunit behaves as its *C. reinhardtii* counterpart or it forms a higher order oligomer, the IFT-74/IFT-81 complex was subjected to SEC-MALS analysis. Interestingly, the SEC-MALS analysis showed that the IFT-74/IFT-81 is a heterodimeric complex with 1:1 stoichiometry, indicating that the IFT-81 does not self-dimerize (Figure 11).

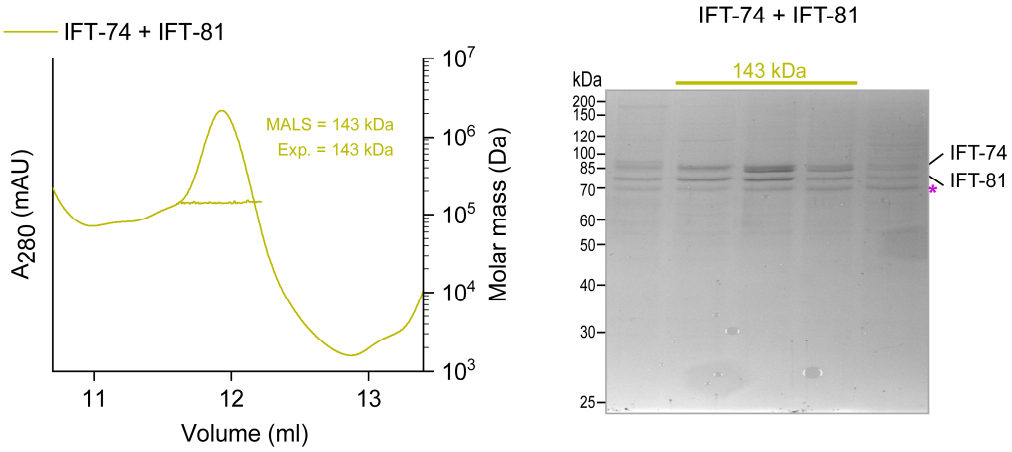

Figure 11: The IFT-74 and IFT-81 subunits form a heterodimer. The SEC-MALS and SDS-PAGE analyses (left and right, respectively) demonstrate that the IF-74/IFT-81 complex is formed stably. The IFT-74/IFT-81 complex is indeed a heterodimer containing one copy of each protein judged from MALS analysis (143 kDa). The molar mass determined from the MALS fit and the expected mass (Exp., calculated theoretically from the sequence of the constructs) are inset. In the SEC-MALS profile, the left axis is the UV absorbance at 280nm, the bottom axis represents the elution volume (ml), and the right axis represents the molar mass (Da). Asterisk refers to the HSP70 protein band. The heterodimeric complex was purified using the Superdex 200 Increase 10/300 GL column.

These results are in agreement with the previous findings in *C. reinhardtii* and in stark contrast to the yeast two-hybrid results [89]. A plausible explanation for this controversy is that $(IFT\text{-}81)_2/(IFT\text{-}74)_2$ heterotetramer is just a false positive result due to a self-homodimerization of the IFT-81 at the coiled-coil domain in the yeast two-hybrid assays.

2.1.3 Assembly of the Tripartite Core Complex (TCC)

In Ni^{2+}–NTA pull-down assays, the *Trypanosoma* IFTA-2$^{His\text{-}tag}$ protein was able to pull down the *C. reinhardtii* (IFT-74/81/25/25)^{untagged} tetrameric complex, implicating that these proteins form a pentameric complex [108]. In addition, crystal structure and SEC analyses showed that the *C. reinhardtii* IFT-74/81/25/25/22 subunits assemble into a stable pentameric complex [93]. To check whether the C. *elegans* tripartite core complex IFT-74/IFT-81/IFTA-2 (Blue subunits in Figure 9; hereafter TCC) forms stably or the additional IFT-25 and IFT-27 subunits, which are missing from the IFT-B core of *C. elegans*, are needed. Intriguingly, the SEC-MALS and SDS-PAGE gel analyses show that the individual subunits of the TCC are held together into a stable complex containing one copy of each protein, suggesting that the additional IFT-25 and IFT-27 subunits are not required for complex formation (Figure 12).

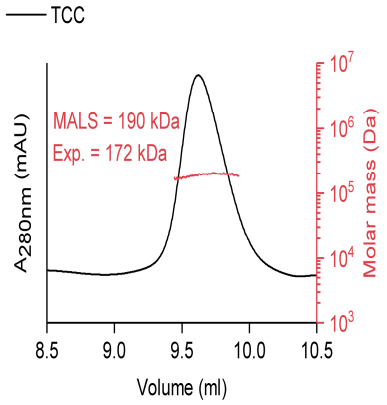

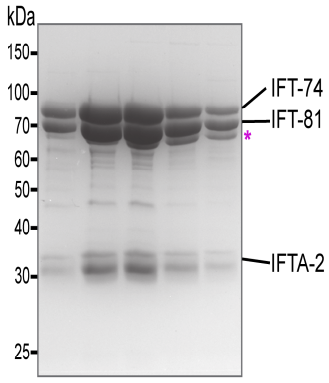

Protein	Calculated molar mass (kDa)
IFT-74	73
IFT-81	70
IFTA-2	29
Total	172

Figure 12: TCC is stably formed. The SEC-MALS elution profile shows that TCC is a 1:1:1 complex (left). The MALS and expected (Exp.) molar masses are inset in red. The SDS-PAGE gel of the MALS peak shows that the subunits of TCC co-elute in the same fractions (middle). The table includes the calculated molar masses of the subunits along with their total sum (right). Asterisk indicates the HSP70 protein band. Gel filtration was carried out using the TSKgel G4000SW$_{XL}$ column.

Notably, the elution profile of the IFT-74/IFT-81 heterodimeric complex has significantly been improved after the addition of the IFT-A2 subunit (Figure 11 versus Figure 12). This behavior is well known for the IFT subunits, as most of the IFT subunits require the presence of their binding partners for stabilization (see section 1.6.3 and part II for discussion).

2.1.4 Investigation of the interaction between TCC and OSM-3(G444E)^{Halo} motor

Previous in vitro studies have shown that the IFT-74/IFT-81 complex interacts with the OSM-3 motor in yeast two-hybrid assays [102]. Moreover, mutations in the genes encoding for these two subunits resulted in disruption of OSM-3-driven IFT [102]. Based on these results, we asked whether the TCC containing the IFT-74/IFT-81 heterodimer can incorporate the OSM-3 into a stable complex. Accordingly, the OSM-3(G444E)^{Halo} motor used in this study was first purified using the TSKgel G4000SW$_{XL}$ to check whether the motor is still a homodimer or the Halo-tag that has been introduced to the end of the C-terminal region of the motor interferes with the motor's structural properties. Fortunately, the motor displayed a homodimeric peak as shown in the SEC-MALS analysis (Supplementary figure 1a). Next, gel filtration was performed using the purified TCC + OSM-3(G444E)^{Halo} complex (Figure 13a, right), which yielded an elution profile with two peaks: peak 1 with a molar mass of 206 kDa corresponds to the OSM-3(G444E)^{Halo} motor alone and peak 2 with a molar mass of 189 kDa corresponds to the TCC alone (Figure 13a, right versus left). Additionally, the SDS-PAGE gel of the collected factions showed that TCC and OSM-3(G444E)^{Halo} motor do not co-elute in the same fractions (Figure 13b, right). Taken together, these results demonstrate that OSM-3(G444E)^{Halo} motor does not bind to TCC. This is in contrast to the previous yeast two-hybrid findings. Notably, the yeast two-hybrid system is well known for producing false positive results [109].

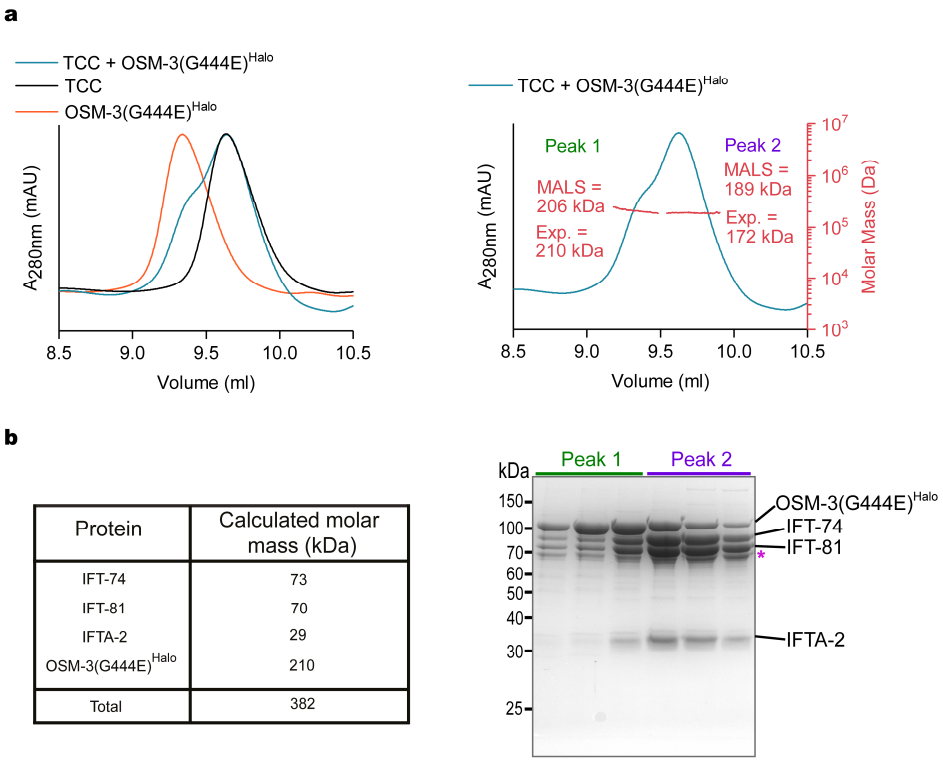

Figure 13: The TCC does not interact with the OSM-3(G444E)^{Halo} motor. (a) Overlay of the SEC profiles of TCC (Figure 12), TCC+ OSM-3(G444E)^{Halo}, and OSM-3(G444E)^{Halo} motor alone (left). The individual SEC-MALS profile of TCC + OSM-3(G444E)^{Halo} (right). Note that peak 1 in the TCC + OSM-3(G444E)^{Halo} SEC-MALS profile overlaps with the OSM-3(G444E)^{Halo} peak, and peak 2 overlaps with the TCC peak (right versus left). The molar masses acquired from MALS and expected molar masses (Exp.) are inset in red. **(b)** The corresponding SDS-PAGE gel shows that TCC and OSM-3(G444E)^{Halo} co-elute in separate fractions (right). The table includes the calculated molar masses from the expected sequences of the TCC subunits and OSM-3(G444E)^{Halo} motor along with their expected sum (left). Asterisk indicates the HSP70 protein band (**b**, right). Data represent three independent experiments. The identities of the protein bands were confirmed by LC-MS/MS analysis [110].

2.1.5 Assembly of the Quadripartite Core Complex (QCC)

The recombinant *C. reinhardtii* OSM-6/OSM-5/DYF-6/DYF-1 subunits (Magenta subunits in Figure 9; hereafter QCC) have been purified as an intact complex using SEC analysis. An elegant crystal structure study from the Lorentzen lab gave a more detailed insights into the reciprocal interactions between the individual proteins of QCC [93]. This study showed that DYF-1 binds to OSM-6 residues (330-370), OSM-5 (118-437) binds to OSM-6 (281-329), and the C-terminal region of DYF-6 (165-319) interacts with the C-terminal domain of OSM-6 (382-454) [93]. These interactions were proven

to be necessary for stabilizing the individual subunits of the complex. For example, the antiparallel interaction between the N-terminal region of DYF-1 and the C-terminal part of OSM-6 induces proper folding of DYF-1 and hence increases its solubility, as the *E. coli* expressed DYF-1 is shown to be insoluble alone [93]. Guided by these findings, we opted for the Flag-tagged, full-length subunits to investigate whether the reconstituted QCC of the *C. elegans* assembles into a stable complex. The full-length subunits represent the wild-type proteins as closely as possible, and the Flag-tag is used for affinity purification of the proteins. The Flag-tag is known to be far superior to other tags (e.g., His-tag) with respect to purity.

Consistent with *C. reinhardtii* results, the SEC-MALS analysis of the *C. elegans* QCC showed that the complex is stably formed (Figure 14). The MALS fit of the complex displayed a heterogeneous distribution, indicating that the QCC is missing another key binding partner that might bring it to homogeneity for a reliable fit (see section 2.1.7 for comparison). This heterogeneous distribution spans from ~460 kDa to ~130 kDa with an overall molar mass average of 301 kDa. The SDS-PAGE gel analysis of the MALS peak demonstrates that the individual proteins of QCC co-elute in the same fractions.

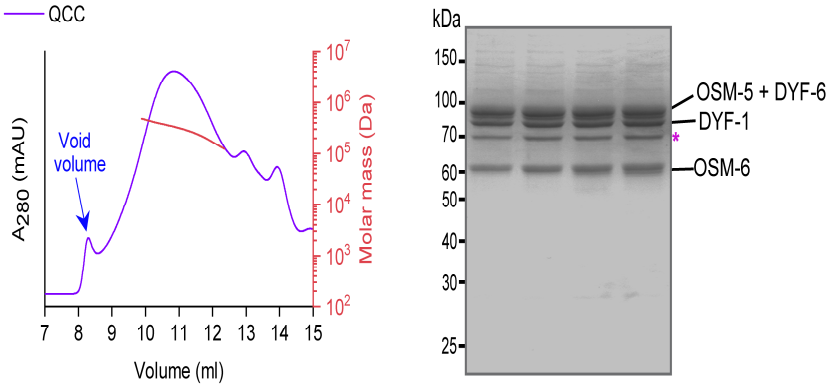

Protein	Calculated molar mass (kDa)
OSM-6	55
DYF-6	55
OSM-5	92
DYF-1	73
Total	275

Figure 14: Assembly of the QCC. The SEC-MALS and SDS-PAGE analyses of the QCC (left and middle, respectively) show that the OSM-5/DYF-6/DYF-1/OSM-6 subunits co-elute in the same fractions, indicating a complex formation. Note that the protein bands of OSM-5 and DYF-6 overlap together and they were positively identified by LC-MS/MS analysis [110]. The table includes the calculated molar mass of the subunits along with their total sum (right). Asterisk indicates the HSP70 protein band. QCC was purified using the Superose 6 Increase 10/300 GL column.

2.1.6 The OSM-3 motor interacts with the DYF-1 subunit of QCC

Previous in vivo studies conducted in *C. elegans* suggested that the DYF-1 subunit recruits the OSM-3 motor into the IFT-B cargo for functional anterograde transport, as loss of function in the

DYF-1 gene resulted in undocking of OSM-3 motor from IFT trains [69]. This provoked the question whether the OSM-3 motor binds to the QCC containing the DYF-1 in our in vitro assays. Before doing a large scale purification that is required for gel filtration of QCC and OSM-3, small scale purifications for pull-down experiments were carried out to probe the interaction between the OSM-3 motor and the individual subunits of the QCC. To this end, the OSM-3(G444E) motor was tagged with a 6x-His tag at the C-terminal (OSM-3(G444E)$^{His\text{-}tag}$), and co-expressed with the C-terminally Flag-tagged individual subunits of QCC. A Flag-tag purification was performed for each pull-down experiment and the supernatant from each Flag-tag purification was later incubated with Ni-NTA Agarose beads for His-tag purification to confirm the presence of the OSM-3(G444E)$^{His\text{-}tag}$ motor in excess during purifications. Purified proteins were resolved using a 10% SDS-PAGE. Strikingly, OSM-3(G444E)$^{His\text{-}tag}$ motor co-precipitated with DYF-1$^{Flag\text{-}tag}$ subunit but not with OSM-6$^{Flag\text{-}tag}$, OSM-5$^{Flag\text{-}tag}$, and DYF-6$^{Flag\text{-}tag}$ subunits (Figure 15). Note that Ni^{2+}–NTA purification of His-tagged proteins is far inferior when compared to Flag-tag protein purification with respect to purity, although the protein bands of the OSM-3(G444E)$^{His\text{-}tag}$ motor are still distinguishable on the SDS-PAGE gel. These results indicate a specific direct interaction between the OSM-3 motor and the DYF-1 subunit of QCC, which is consistent with previous in vivo findings [69].

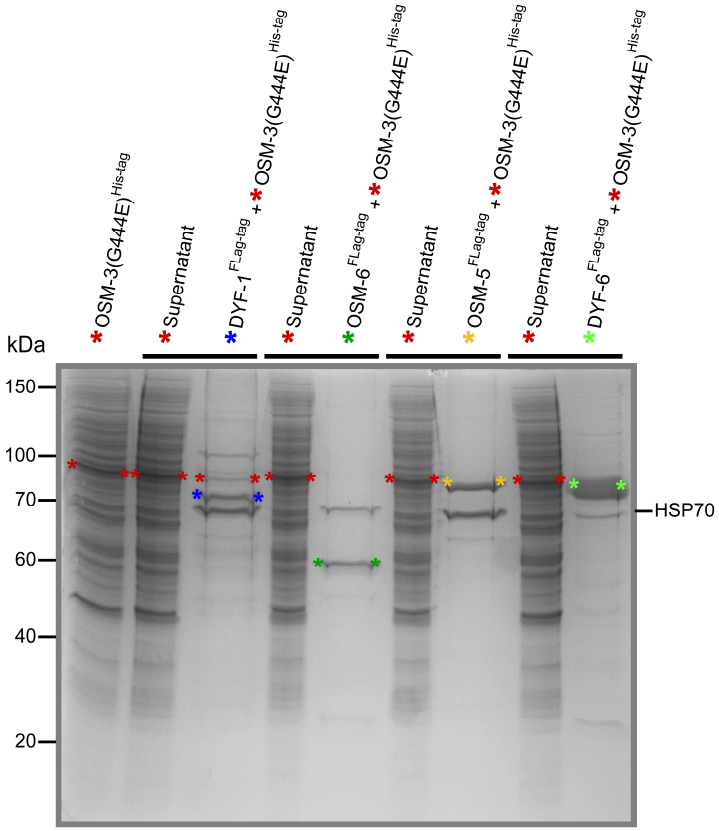

Figure 15: Pull-down assays of the OSM-3(G444E)$^{His\text{-}tag}$ motor with the corresponding Flag-tagged subunits of QCC. Co-expression of the 6xHis-tagged OSM-3(G444E) motor with each Flag-tagged subunit of QCC. The elution of the mock His-purification for the OSM-3(G444E)$^{His\text{-}tag}$ motor is shown on the left lane as a reference. The supernatant and the Flag-pull down for each subunit are shown (demarcated with solid black lines on the top). The OSM-3(G444E)$^{His\text{-}tag}$ band appeared only when the Flag-tagged DYF-1 is present (the third lane from the left). The identities of the protein bands were confirmed by LC-MS/MS analysis.

2.1.7 QCC incorporates OSM-3 motor into a stable complex

To validate the previous results from the pull-down assays, the purified OSM-3(G444E)^{Halo} motor and QCC, which contains the DYF-1 protein displayed a physical binding to OSM-3 motor in pull-down experiment (Figure 15), were subjected to SEC-MALS analysis. Interestingly, QCC could incorporate OSM-3(G444E)^{Halo} motor into a stable complex, suggesting that the interaction that was observed in pull-down experiments between DYF-1 and OSM-3 is indeed strong enough to survive gel filtration (Figure 16, left). Consistent with this notion, OSM-3(G444E)^{Halo} motor co-fractionated with QCC in a stoichiometric manner (Figure 16, right).

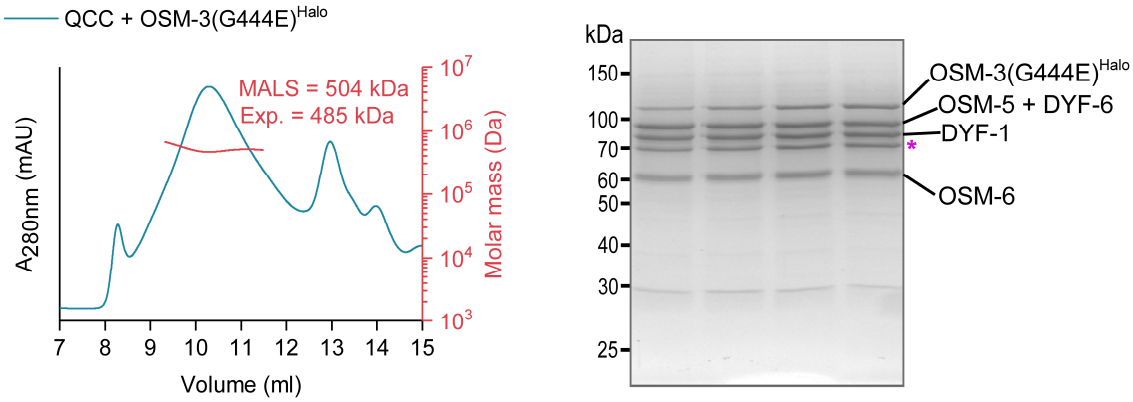

Figure 16: OSM-3(G444E)^{Halo} motor interacts with QCC. The SEC-MALS elution profile (left) shows that OSM-3(G444E)^{Halo} motor binds stoichiometrically to QCC, as the MALS fit of the complex displays a molecular weight of 504 kDa compared to the expected 485 kDa molecular weight. See the calculated molar masses from the expected sequences of the respective subunits in the table in Figure 17. The coomassie-stained SDS-PAGE gel analysis (right) demonstrates that QCC and OSM-3(G444E)^{Halo} motor co-elute in the same fractions, indicating a complex formation. Gel filtration was carried out using the Superose 6 Increase 10/300 GL column. The identities of the protein bands were confirmed by LC-MS/MS analysis [110]. Data represent three independent experiments. Asterisk indicates the HSP70 protein band.

2.1.8 DYF-1 is the key subunit to the incorporation of the OSM-3 into the QCC

The binding specificity of OSM-3 motor to DYF-1, which has been detected in the pull-down experiments (Figure 15), was further evaluated by removing DYF-1 from QCC (hereafter QCC without DYF-1). QCC without DYF-1complex was first co-expressed with OSM-3(G444E)^{Halo} motor and then the purified protein mixture was subjected to gel filtration. Interestingly, removal of the DYF-1 subunit terminated the interaction of the motor with QCC. The SEC-MALS profile of QCC without DYF-1 + OSM-3(G444E)^{Halo} displayed two peaks: peak 1 with 230 kDa MALS fit corresponds to the QCC without DYF-1 complex, whereas peak 2 with a molar mass of 201 kDa corresponds solely to the OSM-3(G444E)^{Halo} motor (Figure 17a, right). In contrast to OSM-3(G444E)^{Halo} motor that co-eluted with QCC under the same peak, OSM-3(G444E)^{Halo} motor is lacking from the peak of QCC without DYF-1 (Figure 16, right versus Figure 17b, right). For proper alignment of elution profiles, OSM-3(G444E)^{Halo} was also purified using the Superose 6 Increase 10/300 GL column (Supplementary figure 1b). The overlay of the elution profiles shows that removal of DYF-1 from QCC resulted in a significant shift in the elution profile of QCC without DYF-1 + OSM-3(G444E)^{Halo} toward a smaller elution volume in comparison to QCC + OSM-3(G444E)^{Halo} elution profile (Figure 17a, left). Consistently, the SEC-MALS along with SDS-PAGE analysis are in agreement with the previous pull-down experiments suggesting that OSM-3 binds only to DYF-1 of QCC (Figure 15).

a

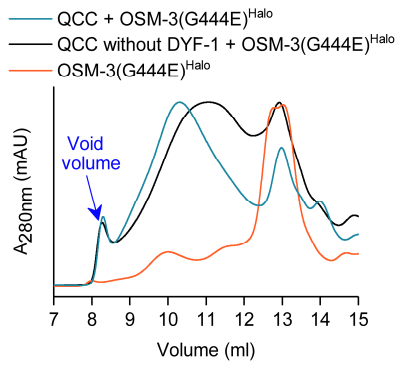

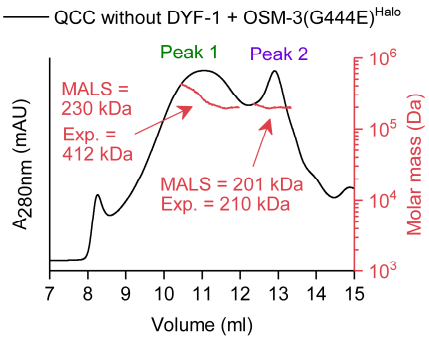

b

Protein	Calculated molar mass (kDa)
OSM-6	55
DYF-6	55
OSM-5	92
DYF-1	73
OSM-3(G444E)^{Halo}	210
Total	485

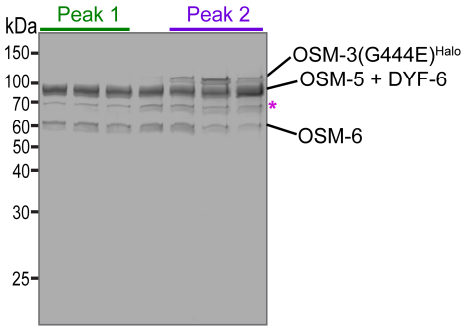

Figure 17: DYF-1 mediates the interaction between OSM-3(G444E)^{Halo} motor and its QCC cargo. (a) Overlay of the SEC chromatograms of QCC + OSM-3(G444E)^{Halo} (Figure 16), QCC without DYF-1 + OSM-3(G444E)^{Halo}, and OSM-3(G444E)^{Halo} shows DYF-1-dependent interaction of the OSM-3(G444E)^{Halo} with QCC (left). The individual SEC-MALS profile of QCC without DYF-1 + OSM-3(G444E)^{Halo} is shown (right). The molar masses acquired from MALS and the expected molar masses (Exp.) are inset in red. **(b)** The calculated molar masses from the expected sequences of the QCC subunits and OSM-3(G444E)^{Halo} motor along with their expected sum (left). The SDS-PAGE gel of the MALS fractions of QCC without DYF-1 + OSM-3(G444E)^{Halo} shows that OSM-3(G444E)^{Halo} motor does not co-elute with QCC without DYF-1 (right). Asterisk indicates the HSP70 protein band. Data represent three independent experiments. The identities of the protein bands were confirmed by (LC-MS/MS) analysis [110].

2.2 MST-based k_d measurement between OSM-3 motor and QCC

Microscale thermophoresis (MST) is a precise tool to measure biomolecular interactions such as protein-protein interactions in free-solution and with a small sample volume (~4 µl) [111]. To complement the previous SEC-MALS findings, MST technique was used to measure the affinity of the interaction (k_d) between OSM-3 and QCC. For this reason, the unlabeled QCC and QCC without DYF-1 complexes were titrated against a fixed concentration of the fluorophore labeled OSM-3(G444E)^{Halo} motor. While the titration of QCC with OSM-3(G444E)^{Halo} yielded a typical sigmoidal binding curve displaying a high binding affinity of 132 ± 8 nM, removal of the DYF-1 subunit abolished this interaction (Figure 18).

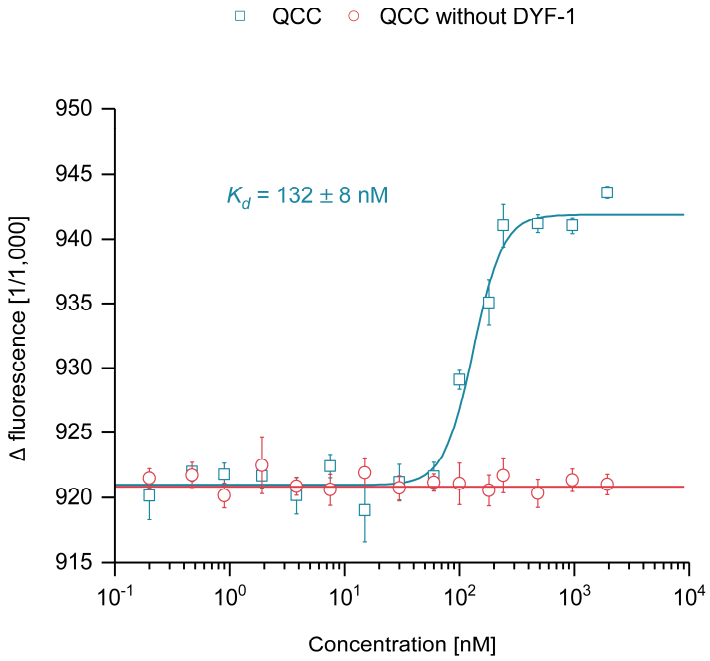

Figure 18: The OSM-3(G444E)^{Halo} motor robustly binds to QCC through the DYF-1 subunit. The Halo-tagged OSM-3(G444E) motor was titrated with QCC and QCC without DYF-1. Only QCC displayed a binding to OSM-3(G444E)^{Halo} motor with k_d of 132 ± 8 nM. Data represent mean ± s.d. from three independent experiments. Y-axis represents the normalized fluorescence intensity, whereas the X-axis represents the serial concentrations of the corresponding complexes.

2.3 Functional investigation of the DYF-1 roles in OSM-3 recruitment and activation

2.3.1 Photobleaching of the individual subunits of the IFT-B core complex

What is the functional relationship between the OSM-3 motor and the IFT-B complexes QCC and TCC? Although previous studies showed that mutations in the IFT-74/IFT-81 subunits of the TCC and the DYF-6/DYF-1 subunits of the QCC disrupt the OSM-3 function in vivo, the functional relationship between these subunits and the motor is still enigmatic in vitro. Our previous solution-based biochemical analyses (SEC-MALS and MST) collectively provided an evidence that the DYF-1 subunit is the key factor that mediates the incorporation of the OSM-3 motor into its corresponding QCC complex; however, the answer of the aforementioned question cannot be concluded from these assays. We therefore turned to fluorescence-based microscopy assays to gain insights into the interplay between the corresponding IFT-B core complexes with their individual subunits and the OSM-3 motor in the context of IFT. To this end, the single subunits of the TCC and the QCC were first C-terminally functionalized with different fluorophores for photobleaching experiments to check their behavior (i.e., aggregation) under assay conditions, as functionalization might cause non-specific, self-assembly of the subunits which eventually lead to aggregates formation. All of the assayed subunits displayed a dominant single photobleaching step, suggesting detection of non-aggregated single molecules (Figure 19).

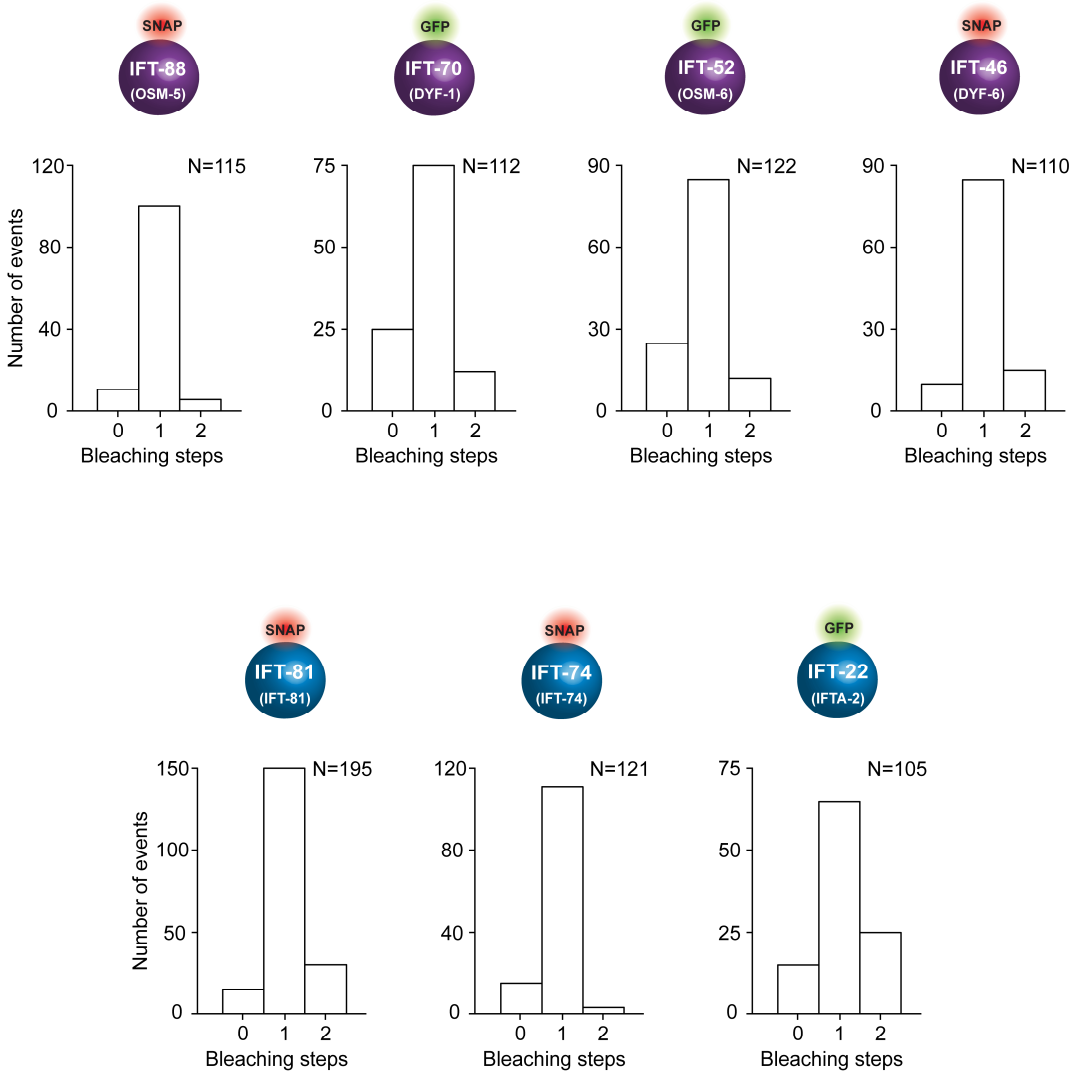

Figure 19: Photobleaching properties of the C-terminally functionalized subunits of IFT-B core complex. All the indicated subunits were C-terminally tagged either with GFP or SNAP tags for fluorophore labelling, and exposed to photobleaching. The individual subunits of QCC are in magenta (top), whereas the TCC subunits are in blue (bottom). N, is the number of events obtained from three independent experiments.

2.3.2 Pairwise colocalization efficiencies of the IFT-B core subunits

Results from the previous biochemical experiments showed that TCC and QCC are indeed stable complexes, however, this does not mean that these complexes will remain intact under the microscopy assay conditions. Because, firstly, fluorophore labeling might interfere with the binding properties of the interacting partners in the complexes resulting in their dissociation. Secondly,

protein complexes are usually exposed to significant serial dilutions, making them more prone to dissociation. Therefore, the C-terminally functionalized single subunits of TCC and QCC, displaying non-aggregates in the photobleaching experiments (Figure 19), were subjected to pairwise colocalization assays. Due to the limitations of the number of fluorescence signals that can be detected simultaneously in our TIRF setup, we could not detect more than two signals at a time. Consistently, all the assayed subunits displayed an efficient colocalization percentage (~80%) with their corresponding binding partners (Figure 20).

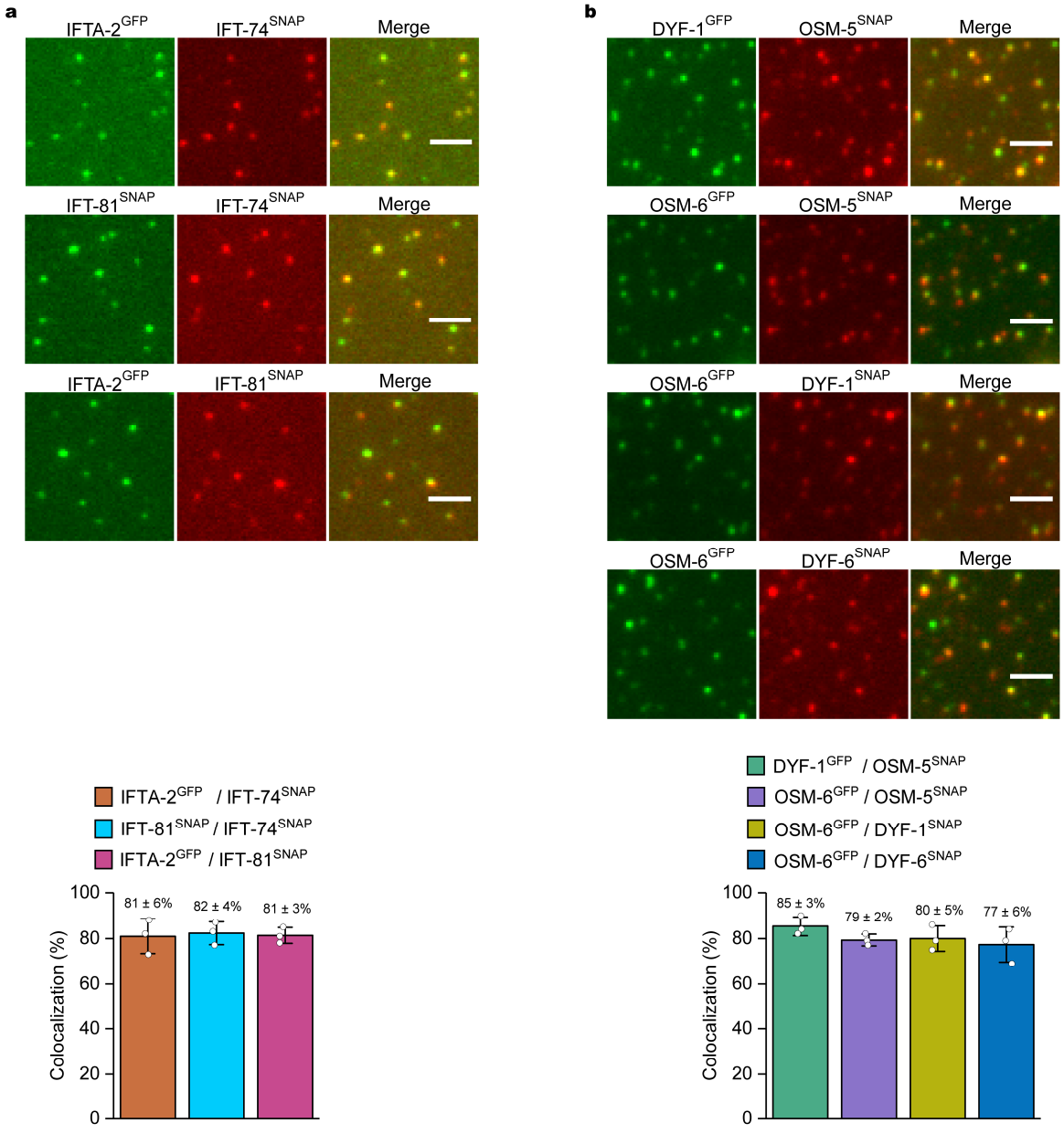

Figure 20: TCC and QCC maintain their complex formation capabilities under single-molecule assay conditions. (a and b, top) The TCC and the QCC subunits were C-terminally functionalized either with GFP or SNAP-tags, and analysed for their pairwise colocalization efficiency. **(a and b, bottom)** The column graphs represent the percentage of the colocalized spots in the corresponding colocalized images (top). All the binary combinations of the labeled subunits displayed a significant colocalization efficiencies. Data are mean ± s.d. from three independent experiments. Scale bars, 3 µm.

These results suggest that the C-terminal functionalization of the subunits does not hinder their assembly, and the assay conditions have no impact on the potentialities of TCC and QCC formation.

2.3.3 OSM-3 motor interacts only with QCC, particularly with its DYF-1 subunit

The constitutively active OSM-3(G444E) motor adopts an extend conformational state, whereas the autoinhibited wild type OSM-3 motor displays a compact conformation, in which the distal part of the C-terminal tail domain is folded back onto the N-terminal head domain (see section 1.7.1) [100, 112]. These two conformational states might have an impact on the intramolecular or intermolecular interactions of the OSM-3 motor. Previous studies conducted in *C. elegans* demonstrated that the worms containing the OSM-3(G444E) motor construct develop severely truncated cilia lacking distal segments of axonemes, phenotypes similar to those observed in OSM-3 null mutants [71, 100]. Consequently, it has been speculated that the OSM-3(G444E) motor lost the ability to associate with the IFT-B cargo and hence it failed to localize inside the cilium to function as an anterograde motor [100]. To verify this hypothesis in our microscopy assays, two types of the OSM-3 motor were designed: the constitutively active OSM-3(G444E)^{Halo} and the wild type OSM-3^{SNAP} motors. The OSM-3(G444E)^{Halo} motor contains a Flag and Halo-tags at the very end of the C-terminal tail, and a glycine to a glutamic acid (G444E) point mutation that has been introduced in the coiled-coil stalk causing an extended conformation of the motor. On the other hand, the compact OSM-3^{SNAP} motor construct possesses a wild type stalk lacking the G444E mutation, and a Flag and a SNAP-tags at the N-terminal domain for affinity purification and fluorophore-labeling, respectively.

The differentially labeled TCC, QCC without DYF-1, and QCC were separately mixed with the fluorophore-labeled OSM-3(G444E)^{Halo} and OSM-3^{SNAP} motors for colocalization measurements. Consistent with our previous SEC-MALS results, neither TCC nor QCC without DYF-1 significantly colocalized with any of the motors; however, the presence of the DYF-1 subunit resulted in an efficient association of QCC with OSM-3(G444E)^{Halo} and OSM-3^{SNAP} motors (Figure 21a and Figure 22a). To delineate whether the colocalization of the OSM-3 motors with the QCC requires a

preformed binding interface or it is specific to the DYF-1 subunit, the C-terminally functionalized OSM-6, OSM-5, DYF-6, and DYF-1 subunits of QCC were accordingly checked for colocalization with both OSM-3(G444E)^{Halo} and OSM-3^{SNAP} motors. Notably, none of the previously mentioned subunits displayed an efficient colocalization with the motors except the DYF-1 subunit that showed a robust interaction with the motors (Figure 21b and Figure 22b).

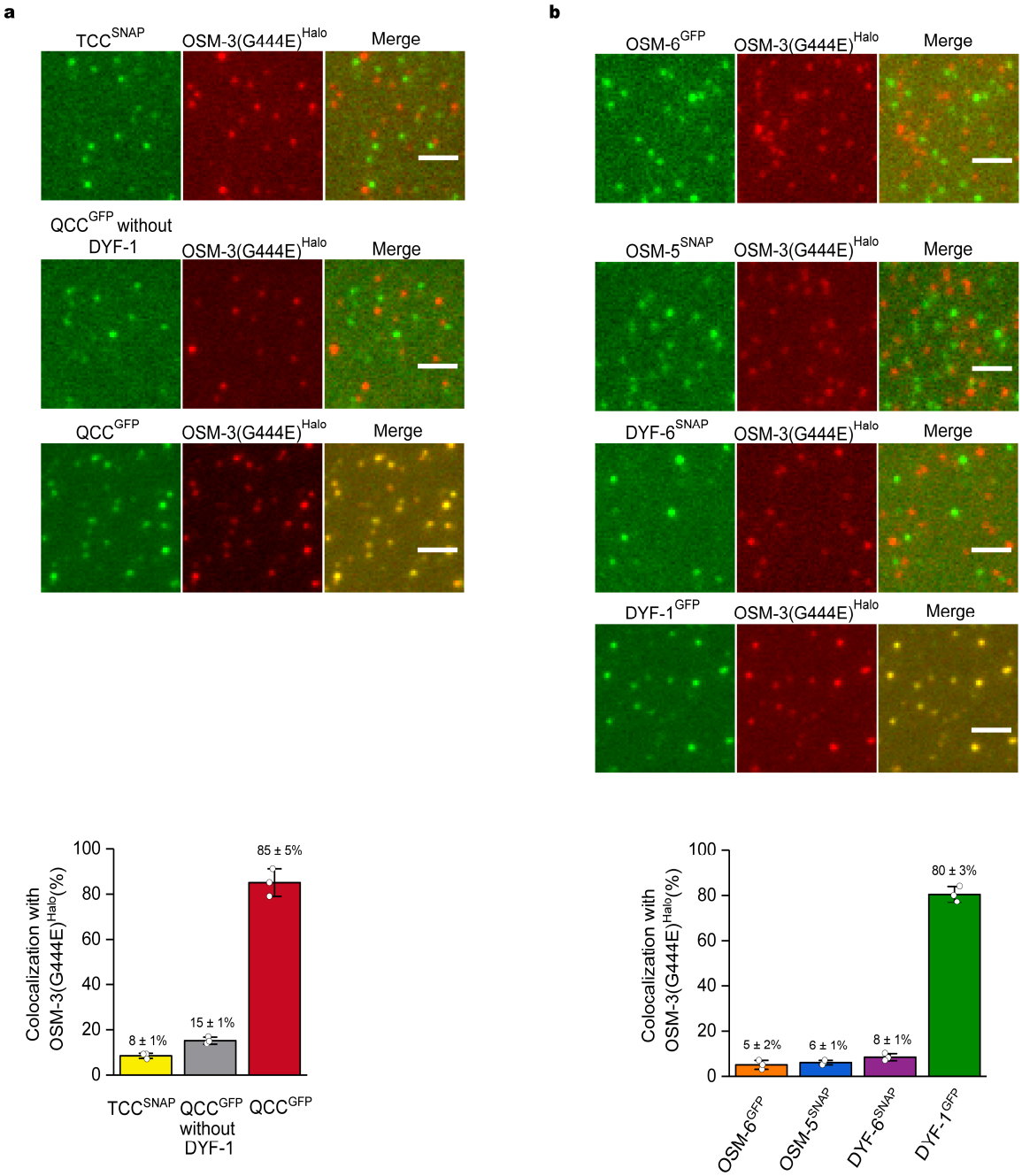

Figure 21: The OSM-3(G444E)^{Halo} motor associates efficiently with QCC due to the presence of the DYF-1 subunit. (a) Neither TCC (with the C-terminally SNAP-tagged IFT-81 subunit) nor QCC that lacks the DYF-1 subunit (with the C-terminally GFP-tagged OSM-6 subunit) efficiently colocalized with the OSM-3(G444E)^{Halo} motor. However, in the presence of DYF-1 subunit, QCC efficiently colocaliazted with the OSM-3(G444E)^{Halo} motor with a colocalization percentage of 85 ± 5%. **(b)** Consistently none of the QCC subunits were capable of interacting with the OSM-3(G444E)^{Halo} motor except the DYF-1 subunit that displayed a strong interacting with the OSM-3(G444E)^{Halo} motor with a colocalization percentage of 80 ± 3%. The column graphs (bottom) represent the percentage of colocalized spots in the corresponding colocalized images (top). Data represent means ± s.d. from three independent experiments. Scale bars, 3 µm.

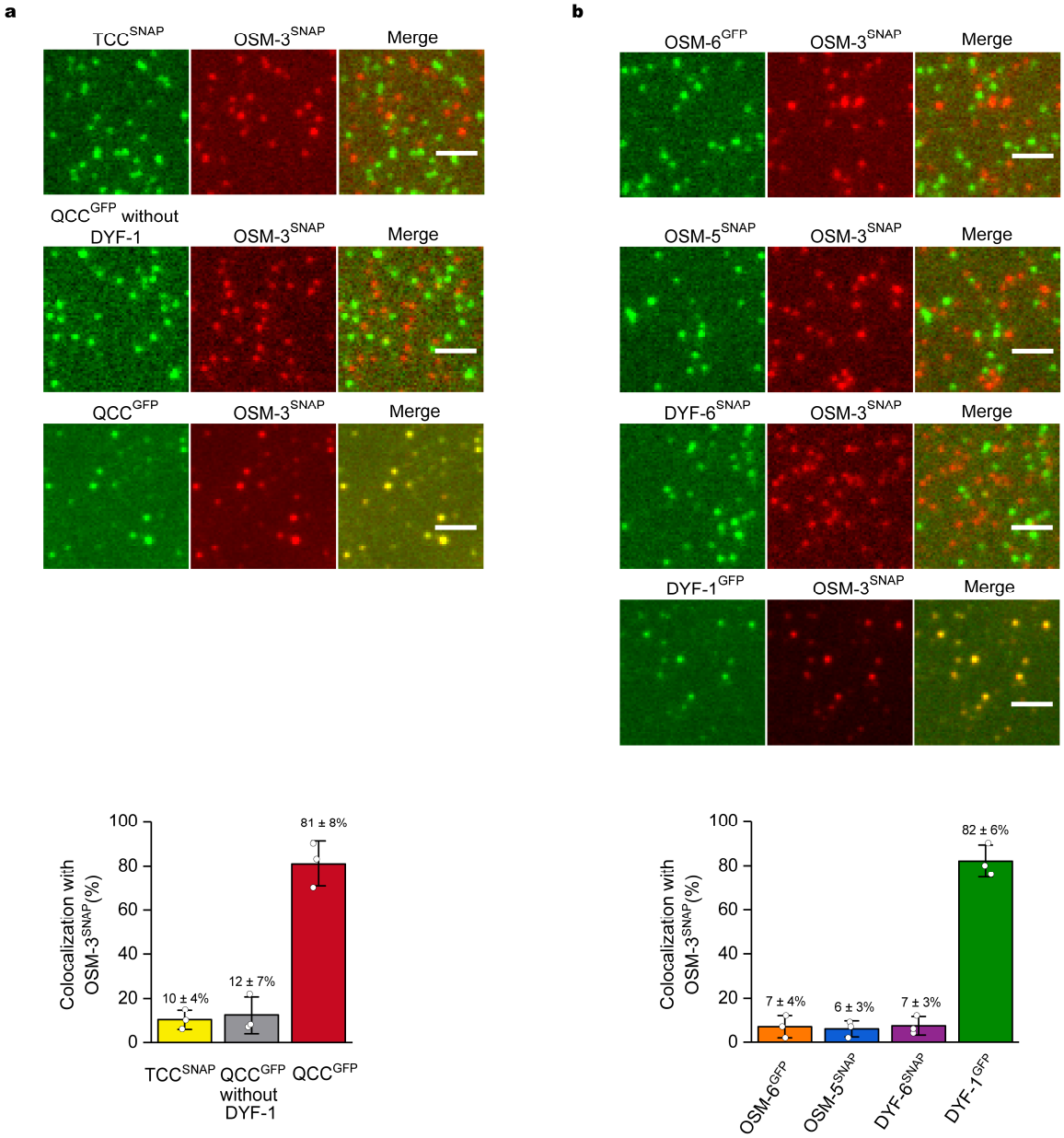

Figure 22: The OSM-3^{SNAP} motor containing a wild type stalk interacts with QCC in a DYF-1-dependent manner. (a) Neither TCC nor QCC without DYF-1 displayed an efficient colocalization with the OSM-3^{SNAP} motor. On the other hand, in the presence of DYF-1 subunit, QCC was capable of binding to the wild type OSM-3^{SNAP} motor with a colocalization efficiency of 81 ± 8%. **(b)** Only the DYF-1 subunit from the QCC displayed an efficient colocalization with the OSM-3^{SNAP} motor (82 ± 6%). The IFT-81 subunit from TCC was SNAP-tagged at the C-terminal. The OSM-6 from QCC without DYF-1 and QCC was C-terminally functionalized with a GFP-tag. Data represented in the column graphs are mean ± s.d. from three independent experiments. Scale bars, 3 µm.

These results collectively indicate that the OSM-3 motor retains the ability to bind to the IFT-B cargo, specifically through the DYF-1 subunit, even after introducing a G444E point mutation into its hinge region. This is in contrast with the hypothesis suggesting that the G444E mutation disrupts the interaction of the motor with its IFT-B cargo in vivo [100]. To further support our findings, an in vivo study in *C. elegans* from the Ou lab showed that movements of OSM-3 motor along the remaining middle segments of axonemes of sensory cilia are severely compromised by the G444E point mutation; however, OSM-3(G444E) motor remains associated with IFT-B cargo [112]. Moreover, in BBS-8 mutant worms (subunit of the BBSsome complex that is required for holding together IFT-A and IFT-B complexes, see section 1.6.4 for details), OSM-3(G444E) motor displayed movements and transported IFT-B complex along the middle segment with a significantly reduced speed of ~0.6 µm/s in comparison to ~0.7 µm/s the intermediate speed of the functionally co-operating OSM-3 and kinesin-II motors [112].

2.3.4 Colocalization of the kinesin-II motor with the IFT-B core complexes

As mentioned before, the rod-shaped sensory cilia of *C. elegans* are built by the cooperatively trafficking kinesin-2 motors: OSM-3 and kinesin-II. These two motors are believed to be held together for concerted functions required for assembly of the middle segment of the axoneme via the adaptor BBSome complex by stabilizing the association between the IFT-A and the IFT-B complexes [69]. This notion is based on the previous in vivo reports showing that in *bbs-7* and *bbs-8* mutant worms, IFT machinery falls apart into two parts: IFT-A complex transported by kinesin-II motor along the axonemal middle segment, and IFT-B complex transported by OSM-3 motor along the middle and the distal segments of the axoneme [69]. Therefore, there exists a conception that the OSM-3 motor is linked to the IFT-B complex, which is in agreement with the results from this study, and the kinesin-II motor is linked to the IFT-A complex but not to the IFT-B complex. On the contrary, a recent cryo-EM study in *C. reinhardtii* showed that during anterograde IFT, the kinesin-II motor is attached to the IFT-B complex, while the IFT-A complex is located on top of the IFT-B

complex and underneath the ciliary membrane [101]. To investigate whether the heterotrimeric kinesin-II (KLP11-KLP20-KAP in *C. elegans*) motor displays a binding affinity to the IFT-B complex, a SNAP fluorophore tag was introduced to the adaptor KAP subunit of the heterotrimeric kinesin-II. The functionalized motor was then subjected to colocalization assays with the differentially labeled TCC and QCC. Expectedly and consistent with previous in vivo results in *C. elegans*, neither TCC nor QCC were able to associate with the heterotrimeric motor (Figure 23); however, the in vitro evidences showing that the heterotrimeric kinesin-II motor does not bind to the IFT-B peripheral complex, and proving the connection between the heterotrimeric motor and the IFT-A complex are still lacking.

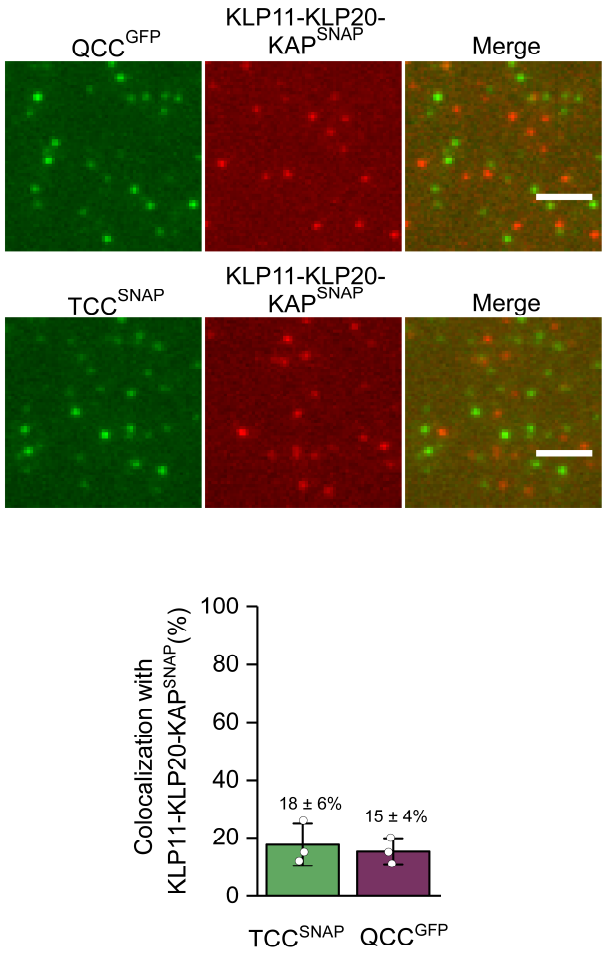

Figure 23: Colocalization of TCC and QCC with the heterotrimeric kinesin-2 (KLP11-KLP20-KAP) motor. Neither TCC (with the SNAP-tagged IFT-81 subunit) nor QCC (with the GFP-tagged OSM-6 subunit) displayed an efficient colocalization with the KLP11-KLP20-KAP^{SNAP} motor. Data in the column graph represent means ± s.d. from three independent experiments. Scale bars, 3 µm.

2.3.5 Functional transport assays demonstrate a DYF-1-dependent recruitment and activation of OSM-3 motor

As discussed above in section 1.7.1, OSM-3 autoinhibition mechanism is achieved by an intramolecular interaction, in which parts of the stalk and the tail domains are folded back interacting with the head domain, and consequently inhibiting the catalytic (i.e., ATPase) activity of the motor and hence its processivity (the ability of taking multiple sequential steps along a microtubule without dissociation). Autoinhibition is a prerequisite for efficient localization of OSM-3 motor to the sensory cilia where it functions in transporting anterograde IFT trains [69, 71, 100]. It also prevents futile ATP hydrolysis when OSM-3 is not engaged in IFT. The recombinantly expressed full-length OSM-3 motor showed a low ATPase (k_{cat} 4 ATP/s/head) activity and did not display a processive movement in single-molecule fluorescence assay [100]. According to previous evidences, relief of OSM-3 autoinhibition can be achieved either by introducing a G444E point mutation in the hinge region, which results in an ATPase activity of 75 ATP/s/head or by attachment to a cargo. Both activation methods convert OSM-3 from a folded conformation into an extended conformation [100]. It has been speculated that the DYF-1 subunit acts as an adaptor and a positive regulator of OSM-3 activity in vivo [69]. This speculation is built on the fact that in the DYF-1 mutant worms, OSM-3 dissociates from IFT trains and diffuses along ciliary axonemes rather than displaying a directional movement [69]. To verify this hypothesis, we turned to functional transport assays, in which TIRF microscopy has been used to directly track movements of the fluorophore-labeled OSM-3 motors with its IFT-B binding cargo along unlabeled surface-attached microtubules and axonemes.

2.3.5.1 Further activation of the constitutively active OSM-3(G444E)^{Halo} motor in vitro

Functional transport assays arguably provide the most direct evidence for the specific recruitment and activation of the OSM-3 motor by the DYF-1 subunit. To assess whether our reconstituted OSM-3–IFT-B complex is capable of directional movement in vitro, we tracked the differentially fluorophore-labeled OSM-3(G444E)^{Halo} motor and its IFT-B complex. The constitutively active OSM-3(G444E)^{Halo} motor displayed a directional movement along the surface-attached microtubules with a velocity of 1.2 ± 0.5 µm/s (Figure 24a, left and Supplementary video1), similar to the transport rates extracted from in vivo studies [58, 69, 71]. Although most of the fluorophore signals from the OSM-3(G444E)^{Halo} motor and the DYF-1^{GFP} subunit were colocalized, velocities of the OSM-3(G444E)^{Halo} alone or in the presence of DYF-1^{GFP} subunit were indistinguishable (1.2 ± 0.5 µm/s versus 1.3 ± 0.3 µm/s) (Figure 24a, left versus middle). Strikingly, incorporation of the OSM-3(G444E)^{Halo} motor into the QCC resulted in further activation of the motor, as the motor velocity

significantly increased from 1.2 ± 0.5 µm/s to 1.8 ± 0.5 µm/s (Figure 24a, left versus right). Consistent with our previous SEC-MALS, MST, and colocalization results, the OSM-3(G444E)^{Halo} motor moved alone along microtubules when incubated with QCC without DYF-1, indicating that the removal of DYF-1 subunit terminated the interaction between OSM-3(G444E)^{Halo} motor and QCC (Supplementary video 1, bottom left). Notably, the processivity of the OSM-3(G444E)^{Halo} motor was independent of the presence of DYF-1 subunit and QCC (Figure 24b).

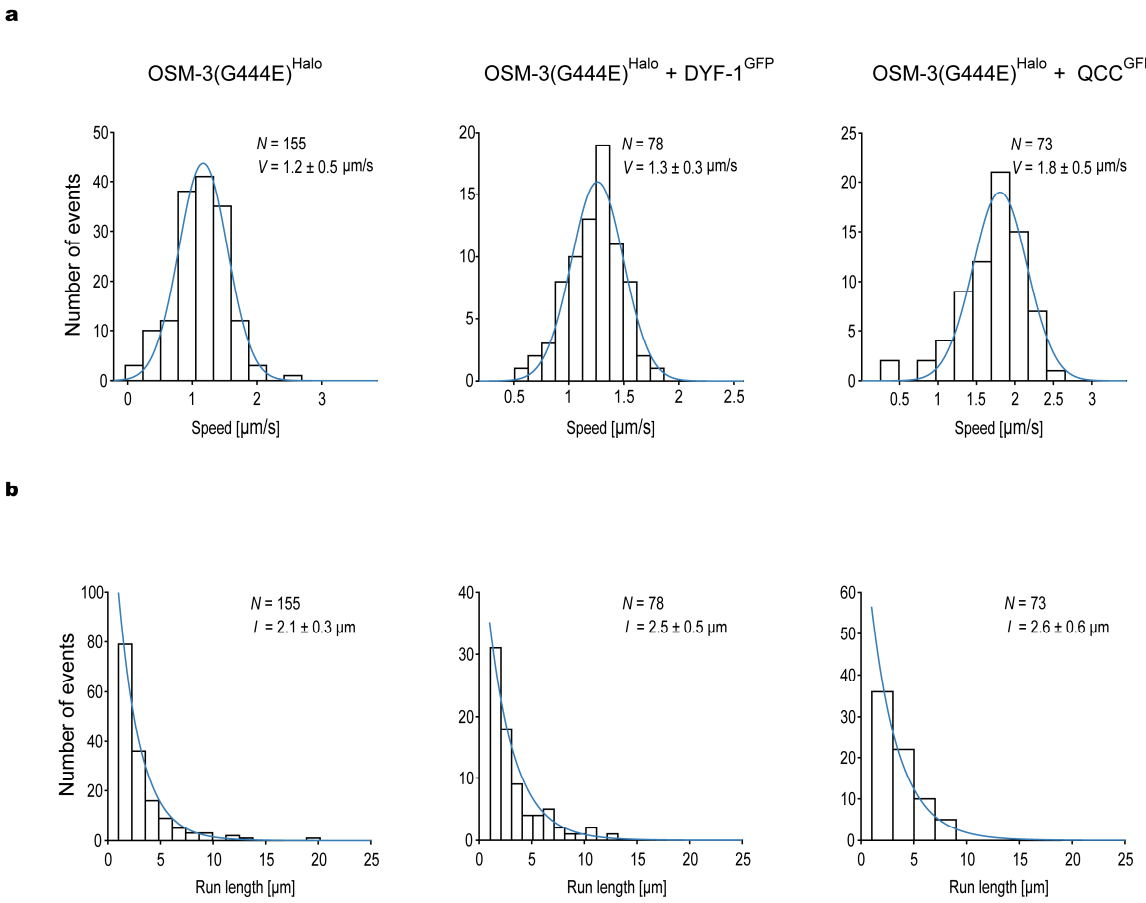

Figure 24: Transport parameters of the OSM-3(G444E)^{Halo} motor and its IFT-B cargos on purified microtubules. (a) The velocity of the constitutively active OSM-3(G444E)^{Halo} motor was indiscernible in the presence (middle) and the absence (left) of the DYF-1 subunit, however, incorporation into the QCC fully activated the motor as indicated with the significant increase of the motor's velocity from 1.2 ± 0.5 µm/s to 1.8 ± 0.5 µm/s (left versus right). *P* values for velocities were obtained from a two-tailed *t*-test assuming unequal variances: OSM-3(G444E)^{Halo} versus OSM-3(G444E)^{Halo} + DYF-1^{GFP}, 0.013; OSM-3(G444E)^{Halo} versus OSM-3(G444E)^{Halo} + QCC^{GFP}, 2.5 × 10^{-18}; OSM-3(G444E)^{Halo} + DYF-1^{GFP} versus OSM-3(G444E)^{Halo} + QCC^{GFP}, 3.4 × 10^{-15}. **(b)** The processivity of the motor did not alter in the presence of the DYF-1 subunit or the QCC. *N*, number of events acquired from three independent experiments. *V*, velocity and *l*, run length. Velocities were fit to a Gaussian distribution, mean ± s.d. Run length data were fit to a single exponential ± confidence interval.

2.3.5.2 Changing tracks does not influence the motility properties of OSM-3

Microtubules and axonemes are structurally distinct tracks utilized by different subsets of motor proteins for transport processes in vivo. Microtubules purified from porcine brains (see section 8.3.2 in methods part) used in this study are singlet filaments; however, intraflagellar transport is carried out along axonemes, which are microtubule-based structures comprising nine peripherally arranged doublet microtubules. Each doublet consists of A- and B-tubule (see section 1.2.1). Changing tracks between microtubules and axonemes has been shown to have different impacts on processivity of kinesin motors. For example, in an in vitro study, the authors showed that kinesin-2 motors distinguish between axonemes (doublet tracks) and microtubules (singlet tracks) in their stepping behavior [113, 114]. When walking on microtubules, kinesin-2 motors take step sizes of ~13 nm. This step size significantly increases to ~16 nm when the motor tracks on axonemes. Moreover, kinesin-2 motors display left-handed spiraling trajectories around microtubules, whereas they walk straight on axonemes. The difference in the stepping pattern suggests that the kinesin-2 motors take biased left-handed sidesteps to the neighboring protofilaments of the microtubule lattice ensuring that the kinsen-2-driven anterograde transport takes place on the B-tubule to prevent any unnecessary collision with the dynein-powered retrograde trains that are driven on the A-tubule [81, 113].

Intrigued by these findings, we asked whether the transport rates of OSM-3(G444E)^{Halo} motor measured on microtubules will get affected when using axonemes purified from sperms of the black sea urchin *Arbacia lixula* (courtesy of Willi L Stepp). Accordingly, all the experimental procedures that have been used to obtain the previously mentioned transport parameters of OSM-3(G444E)^{Halo} motor on microtubules were typically followed in the case of using axonemes with the exception that axonemes were directly attached to surface of flow chamber via unspecific binding. The transport parameters obtained for the motor walking on axonemes were similar to those detected when microtubules were used (Figure 25 versus Figure 24). In addition, the processivity of the OSM-3(G444E)^{Halo} motor did not alter in the presence of the DYF-1 subunit and the QCC (Figure 25b). Given the consistency of data obtained from axonemes and microtubules, all the following experiments were conducted using microtubules purified from porcine brains.

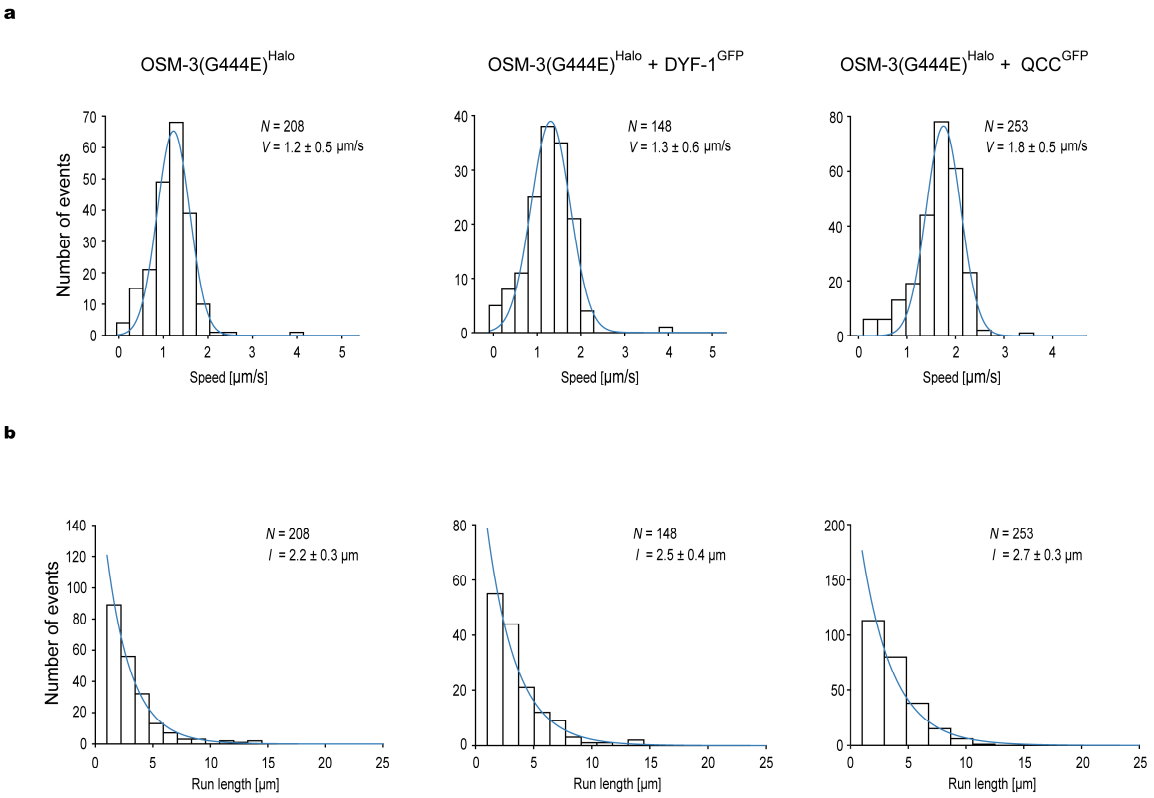

Figure 25: Single-molecule transport parameters of the OSM-3(G444E)^{Halo} motor and its IFT-B cargos on axonemes. (a) The velocity of the constitutively active OSM-3(G444E)^{Halo} motor was indistinguishable in the presence (middle) or absence (left) of DYF-1. Incorporation of OSM-3(G444E)^{Halo} motor into QCC fully activated the motor judged from the significant increase of the motor's velocity from 1.2 ± 0.5 µm/s to 1.8 ± 0.5 µm/s (left versus right). *P* values for velocities were obtained from a two-tailed *t*-test assuming unequal variances: OSM-3(G444E)^{Halo} versus OSM-3(G444E)^{Halo} + DYF-1^{GFP}, 0.025; OSM-3(G444E)^{Halo} versus OSM-3(G444E)^{Halo} + QCC^{GFP}, 1.4×10^{-21}; OSM-3(G444E)^{Halo} + DYF-1^{GFP} versus OSM-3(G444E)^{Halo} + QCC^{GFP}, 2.6×10^{-20}. **(b)** The processivity of the motor is independent of the presence of the DYF-1 subunit or the QCC. *N*, number of events acquired from three independent experiments. *V*, velocity and *l*, run length. Velocities were fit to a Gaussian distribution, mean ± s.d. Run length data were fit to a single exponential ± confidence interval.

2.3.5.3 QCC is the minimum IFT-B complex that is required for full activation of OSM-3

The previous results showing that the DYF-1-dependent incorporation into the QCC further activates the OSM-3(G444E)^{Halo} motor in vitro, provoked the question whether the ~1.8 µm/s is the maximum speed the motor can achieve in vitro or the motor can get further activated by adding more of the IFT-B particles. We therefore sought to assemble larger IFT-B complexes in vitro and investigate their impact on OSM-3 velocity and processivity in functional TIRF assays.

Crystal structure studies in *C. reinhardtii* showed that the IFT-B core complex can assemble stably by connecting IFT-52 (OSM-6) and IFT-46 (DYF-6) subunits of QCC with IFT-74 (IFT-74) and IFT-81 (IFT-81) subunits of TCC [93]. Guided by these findings and our successful assembly of QCC, TCC, and QCC + OSM-3 complexes as shown previously, we opted for the assembly of the *C. elegans* IFT-B core complex (QCC + TCC) consisting of seven subunits. Intriguingly, we were able not only to assemble the entire IFT-B core complex but also the IFT-B core complex + OSM-3 (Figure 26). The assembled complexes displayed a heterogeneous MALS fits with an overall average of 453 kDa and 625 kDa molecular weights of the IFT-B core complex and the IFT-B core complex + OSM-3, respectively (Figure 26a, middle and right). The heterogeneity and peak broadening of the complexes may be due to the absence of other binding partners from the IFT-B peripheral subunits whose presence might convert this heterogeneity to a more reliable homogeneous MALS fits.

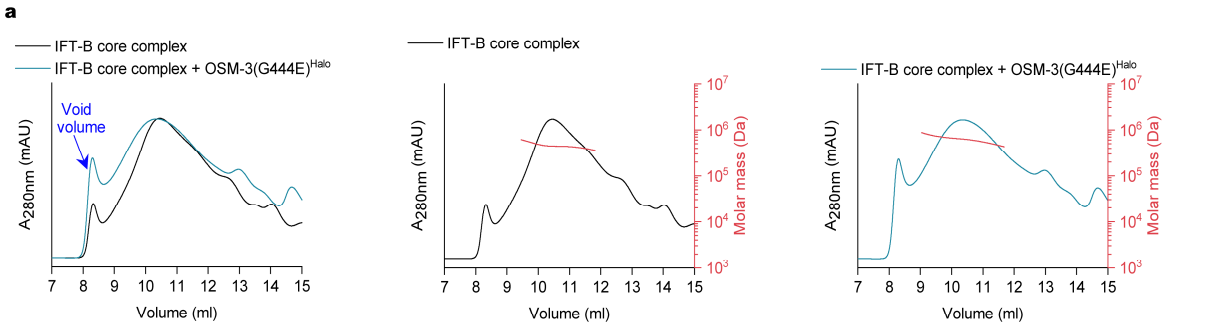

Protein	Calculated molar mass (kDa)
OSM-6	55
DYF-6	55
OSM-5	92
DYF-1	73
IFT-74	73
IFT-81	70
IFTA-2	29
OSM-3(G444E)Halo	210
Total	657

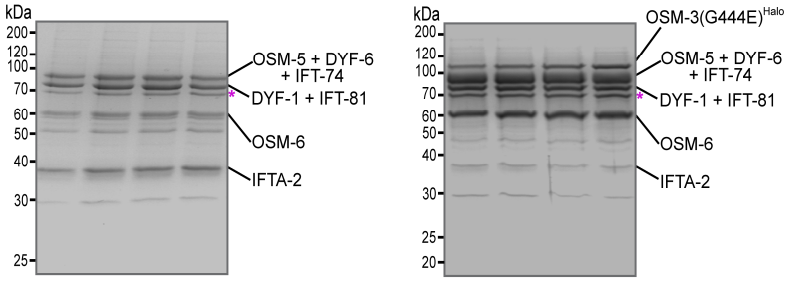

Figure 26: Assembly of the IFT-B core complex with the OSM-3(G444E)^{Halo}. (a) Overlay of the SEC profiles of the IFT-B core complex and the IFT-B core complex + OSM-3(G444E)^{Halo} (left) along with their individual SEC-MALS profiles (middle and right, respectively). **(b)** The SDS-PAGE gel analyses of the corresponding complexes (middle and right). The table indicates the calculated molar masses of the IFT-B core subunits and the OSM-3(G444E)^{Halo} along with their total sum (left). Note that the protein bands of OSM-5/DYF-6/IFT-74 and DYF-1/IFT-81 overlap together. They were positively identified by LC-MS/MS. Asterisks in **(b)** indicate the HSP70 protein band.

Our previous colocalization results showed that TCC and QCC are stably formed under functional assay conditions (Figure 20). Therefore, to track the entire IFT-B core complex under TIRF microscopy, the TCC was labeled with a fluorophore SNAP tag at the IFT-81 subunit and the QCC was labeled with a GFP tag at the DYF-1 subunit. Owing to limitations of number of fluorescence signals that can be simultaneously detected by the TIRF microscopy used in this study, we designed an OSM-3 motor construct with a G444E point mutation and a Flag tag at the C-terminal for affinity purification (hereafter OSM-3(G444E)^{Flag}).

To determine whether the IFT-B core complex has an effect on the transport parameters of motor, the differentially labeled TCC and QCC were incubated with the OSM-3(G444E)^{Flag} motor and then movements were detected under TIRF microscopy. Although most of fluorophore signals from TCC and QCC were colocalized and moved directionally by motor along microtubules, neither velocity nor run length values of OSM-3(G444E)^{Flag} motor increased when compared to values of OSM-3(G444E)^{Halo} + QCC^{GFP} (Figure 27a, b left versus Figure 24a, b right).

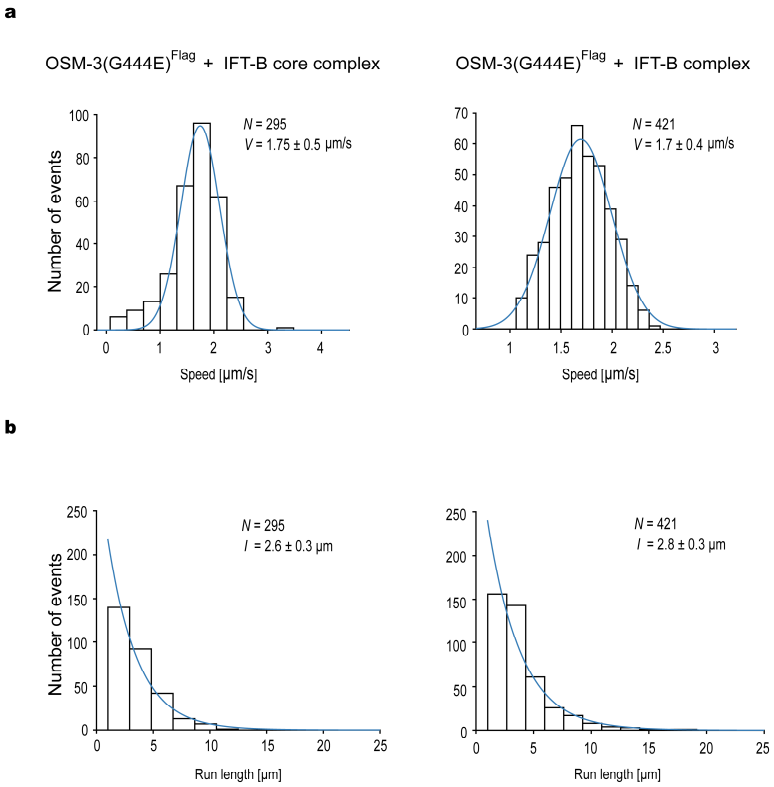

Figure 27: The IFT-B complex cannot further activate the OSM-3 motor than QCC. **(a)** Velocity histograms of the OSM-3(G444E)^{Flag} motor with the IFT-B core complex and the entire IFT-B complex show constant transport rates of the OSM-3 motor (left and right, respectively). **(b)** The corresponding analysis of run length data. *N*, number of events acquired from three independent experiments. *V*, velocity and *l*, run length.

Previous in vitro reconstitution studies confirmed that the IFT-B subunits of C*. reinhardtii* form a stable complex, as the authors reconstituted the whole IFT-B complex lacking only the IFT-56 (DYF-13) subunit [92]. These results motivated us to take it further and ask the question what are the functional consequences of the whole IFT-B complex (14 subunits) on the OSM-3 motor. To this end, the IFT-B peripheral complex (7 subunits) labeled with a fluorophore SNAP tag at the Y110A7A.20 subunit and the IFT-B core complex (7 subunits) labeled with a GFP tag at the DYF-1 subunit were incubated with the OSM-3(G444E)^{Flag} motor, and the mixtures were eventually subjected to functional transport assays. Similarly, although most of the fluorophore signals from the IFT-B peripheral and the IFT-B core complexes were colocalized and moved directionally by motor along microtubules, neither the velocity nor the run length of the OSM-3(G444E)^{Flag} were affected when compared to OSM-3(G444E)^{Halo} + QCC^{GFP} (Figure 27a,b right versus Figure 24a, b right). Taken together, these results suggest that of the 14 subunits forming the IFT-B complex, the four subunits of the QCC are sufficient to fully unleash the OSM-3 activity in vitro.

2.3.5.4 Relief of the wild type OSM-3 autoinhibition by its DYF-1 cargo

Results derived from previous transport assays showed clearly the colocalized movements of the OSM-3(G444E)^{Halo} with the DYF-1 and the QCC cargos; however, one is unable to conclude whether the DYF-1 cargo is capable of relieving the autoinhibition of OSM-3 in vitro, since motor constructs used in these assays are constitutively active. Therefore, we turned to the autoinhibited OSM-3^{SNAP} motor containing a wild type stalk. Similarly, fluorophore-labeled OSM-3^{SNAP} motor was individually mixed with DYF-1, QCC without DYF-1, and QCC. Functional transport TIRF assays were subsequently performed for OSM-3^{SNAP} alone and previous protein mixtures.

In contrast to OSM-3(G444E)^{Halo} motor that displayed directional movements, OSM-3^{SNAP} motor was incapable of preforming directional movements but rather displayed bidirectional diffusion along surface-attached MTs (compare the top left of the Supplementary video 1 to the top left of the Supplementary video 2). These results are in agreement with previous studies showing that wild type OSM-3 is an autoinhibited motor [69, 100]. It has been suggested that cargo attachment relieves OSM-3 autoinhibition and initiates its processive movement [100]. Remarkably, the diffusing OSM-3^{SNAP} motor displayed a robust unidirectional movement in the presence of its DYF-1 cargo with a velocity of 1.3 ± 0.3 µm/s, (Figure 28a left and the top right in the Supplementary video 2), denoting that the DYF-1 subunit is capable of relieving the autoinhibition mechanism of the wild type OSM-3 motor, which was predicted previously when loss of function mutation in the DYF-1 gene led to the dissociation of the OSM-3 from IFT trains and in addition the OSM-3 motor was no longer able to move along axonemes [69]. Consistently, as in the case of OSM-3(G444E)^{Halo} + QCC,

incorporation of OSM-3^{SNAP} motor into QCC further enhanced its velocity to 1.7 ± 0.6 µm/s compared to 1.3 ± 0.3 µm/s velocity of OSM-3^{SNAP} + DYF-1^{GFP} (Figure 28a left versus right). Removal of the DYF-1 subunit abolished the interaction of OSM-3^{SNAP} motor with QCC, which in turn resulted in the deactivation of the motor that displayed a bidirectional diffusion along MTs (the bottom left of the Supplementary video 2). Finally, the processivity of the DYF-1 activated OSM-3^{SNAP} motor was independent of the presence of DYF-1 or the QCC (Figure 28b).

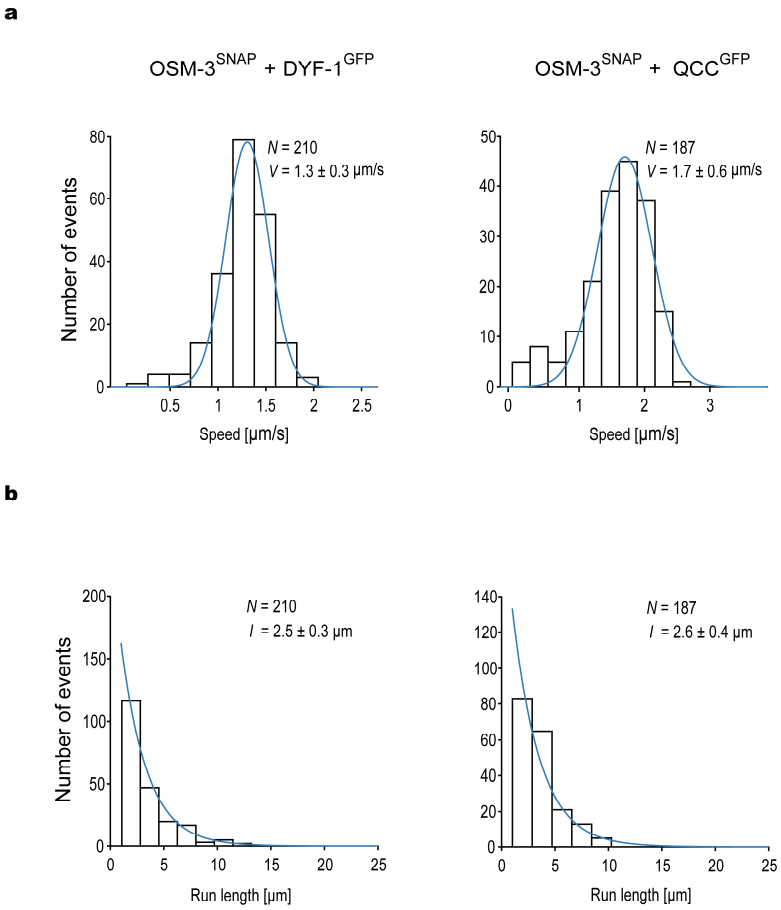

Figure 28: The autoinhibited OSM-3^{SNAP} motor with a wild type stalk is activated by the DYF-1. (a) Velocity histograms of OSM-3^{SNAP} + DYF-1^{GFP} (left) and OSM-3^{SNAP} + QCC^{GFP} (right) show that theDYF-1-dependent incorporation into QCC fully activates the wild type OSM-3^{SNAP} motor. *P* values for velocities were obtained from a two-tailed *t*-test assuming unequal variances: OSM-3^{SNAP} + DYF-1^{GFP} versus OSM-3^{SNAP} + QCC^{GFP}, $P = 1.8 \times 10^{-12}$. **(b)** Once activated by the DYF-1 subunit, the processivity of the OSM-3^{SNAP} was not modified by the presence of DYF-1 and QCC. *N*, number of events acquired from three independent experiments. *V*, velocity and *l*, run length.

Next, we designed a wild type OSM-3 construct with only a Flag-tag at the C-terminus (hereafter OSM-3^{Flag}) to ensure that the N-terminal Flag and SNAP-tags do not interfere with the autoinhibitory folding of the motor. The OSM-3^{Flag} motor cannot be tracked directly in the transport assays due to the lack of fluorescence information. However, the OSM-3^{Flag} represents the wild type motor as closely as possible. Consistently, the DYF-1 subunit recruited and activated the OSM-3^{Flag} motor for an efficient transport with velocity rates of 1.3 ± 0.4 µm/s (Figure 29a left and the top left of the Supplementary video 3). The OSM-3^{Flag} motor was fully activated in the presence of QCC, as the motor displayed a velocity of 1.7 ± 0.5 µm/s compared to 1.3 ± 0.4 µm/s velocity of the OSM-3^{Flag} + DYF-1^{GFP} (Figure 29a right and the top right of the Supplementary video 3). Finally, once activated by the DYF-1 subunit, the processivity of the OSM-3^{Flag} was independent of the presence of the DYF-1 and the QCC (Figure 29b).

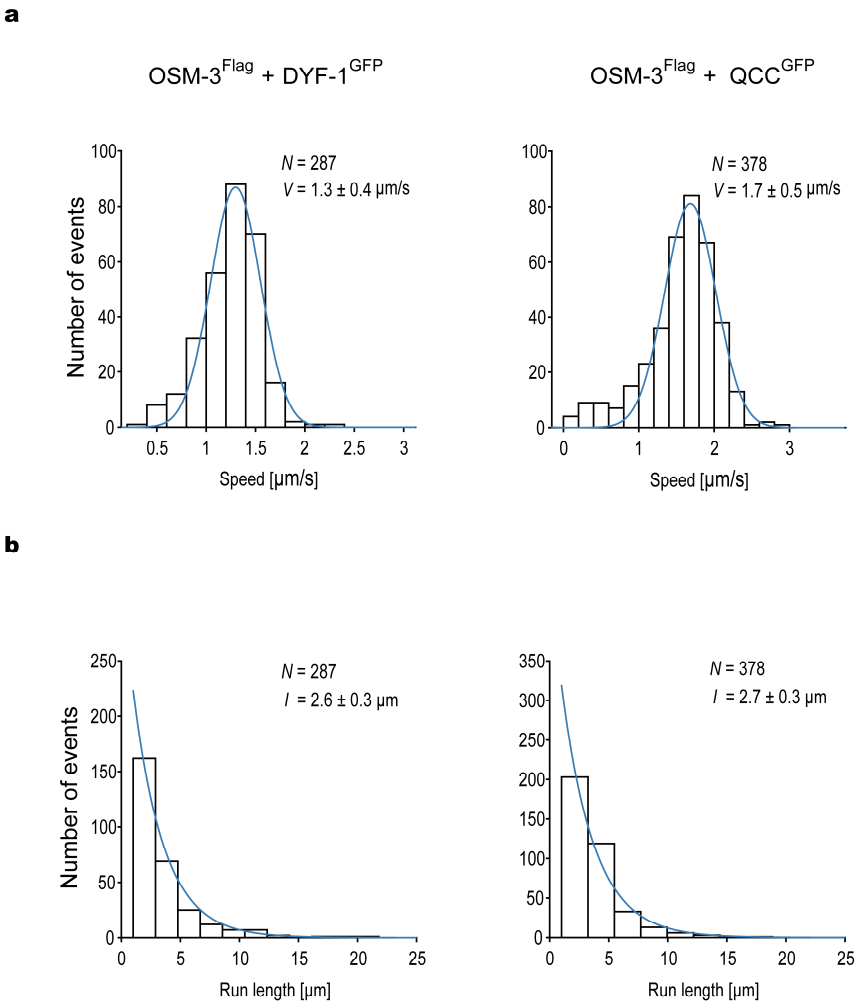

Figure 29: DYF-1-mediated incorporation into QCC fully activates the wild type OSM-3^{Flag} motor. (a) DYF-1 alone is capable of abolishing the autoregulation of the wild type OSM-3^{Flag} motor, whereas QCC binding fully activates the motor in vitro. Velocity histograms of OSM-3^{Flag} + DYF-1^{GFP} and OSM-3 ^{Flag} + QCC^{GFP} (left and right, respectively). *P* values for velocities from a two-tailed *t*-test assuming unequal variances: OSM-3^{Flag}+ DYF-1^{GFP} versus OSM-3^{Flag} + QCC^{GFP} right, $P = 9.6 \times 10^{-25}$). **(b)** The corresponding run length histograms. *N*, number of events acquired from three independent experiments. *V*, velocity and *I*, run length.

Taken together, the functional transport assays show that the wild type OSM-3 is an autoinhibited motor displaying a two-dimensional back and forth diffusion along MTs (the top left of the Supplementary video 2). The presence of the DYF-1 subunit alone is sufficient to relieve the autoinhibition of OSM-3 motor (the top right of the Supplementary video 2 and the top left of the Supplementary video 3). However, the DYF-1-mediated OSM-3 incorporation into the QCC results in an allosteric activation of the motor (Figure 24, Figure 25, Figure 28, and Figure 29).

3 Discussion

The spatial and temporal regulation of motor-based IFT transport ensures precise cilia assembly and maintenance. This regulation is the key factor for versatile biological functions performed by sensory cilia. In the sensory cilia of *C. elegans*, two different kinesin-2 motors (the heterotrimeric kinesin-II and the homodimeric OSM-3) are employed to drive anterograde IFT trains. Based on their unique structure, kinesin-2 motors display a folded autoinhibitory conformation in the absence of IFT cargo by assuming a direct motor-to-tail interaction to prevent erroneous ATPase activity and congestion of microtubule tracks. Introducing a point mutation (G444E) in the well conserved kink region of the motors hampers their autoinhibition in vitro ; however, the G444E constitutively active motors do not support building of sensory cilia of *C. elegans* in vivo [100, 112]. How the heterotrimeric kinesin-II and the homodimeric OSM-3 motors are regulated inside the cilium is unknown. In this study, we focused on the homodimeric OSM-3 motor and its IFT-B cargo as an example to reveal the regulatory mechanisms that control kinesin-2 motor activities in vivo.

Loss of function in many IFT-B subunits has been proposed to interfere with OSM-3 function in vivo [100, 112]. In particular, loss of DYF-1 function leads to dissociation of OSM-3 from IFT trains and production of phenotypes lacking the distal segment of the axoneme, phenocopies of OSM-3 mutant animals [69]. Therefore, it has been suggested that not only the DYF-1 is involved in the IFT-B/OSM-3 interaction but also it mediates the activation of the motor in vivo [69]. This conclusion is plausible but it does not tell whether the effects seen in the loss of DYF-1 function mutants are due to direct effects of DYF-1 on OSM-3 motor or an unidentified intermediary is involved in DYF-1-dependent activation of the motor (e.g., posttranslational modifications (PTMs)) [69]. There exist in vivo clues showing that DYF-1 is involved in PTMs of tubulin. For example, knockout of DYF-1p, the ortholog of *C. elegans* DYF-1, in *Tetrahymena thermophila* results in formation of short axonemal remnants with hyperglutamylated tubulins, but displayed normal levels of tubulin glycylation [115]. Contrarily, mutations in the fleer gene encoding for DYF-1 in zebrafish cause production of short cilia exhibiting defects in B-tubules ultrastructure and reduced levels of tubulin glutamylation and glycylation [116, 117].

Posttranslational modifications are known to affect the motility properties of kinesin motors. Detyrosination of α–CTT tubulin has been shown to increase the processivity but not the velocity of OSM-3 motor by ~2 fold in *C. elegans* , whereas tubulin deglutamylation regulates the velocity of OSM-3 motor in male-specific cephalic cilia (CEM) of *C. elegans* [118, 119]. Thus, the idea that DYF-1 activates OSM-3 motor through an unidentified intermediary is an attractive one. On the other

hand, the idea that DYF-1 activates OSM-3 motor through a direct protein-protein interaction is undeniable and supported by co-immunoprecipitation experiments in mouse showing that TTC30/DYF-1 physically interacts with KIF-17/OSM-3 [120].

Given the previous discrepancies in the DYF-1 functions, we opted for investigating whether DYF-1 modulates OSM-3 activity directly or other factors are needed. Therefore, our attention was shifted to the IFT-B core complex containing the target DYF-1 subunit. To this end, the wild type, full-length IFT-B core subunits were recombinantly expressed using the baculovirus Sf9 expression system. This was followed by screening co-expression experiments to map the interactions between the IFT-B core subunits and the IFT-B core subunits with the OSM-3 motor (Figure 10 and Figure 15, respectively). Although these experiments gave us some hints that the subunits of TCC and QCC might form stable complexes and only the QCC subunit DYF-1 can co-precipitate the motor, some IFT-B subunits are known to form non-specific bindings to other subunits or even to motor proteins in pull-down and co-immunoprecipitation assays, probably due to the presence of coiled-coil domains in their structure [89, 90, 106].

Next, we made use of SEC-MALS to monitor the interactions seen in the co-expression experiments and gauge the molecular masses of the presumptive complexes. Our SEC-MALS experiments showed, firstly, that the subunits of TCC and QCC form stable complexes with a stoichiometric ratio (Figure 12 and Figure 14). Secondly, OSM-3 motor interacts only with QCC. The interaction is dependent on DYF-1 subunit, as deletion of DYF-1 resulted in dissociation of the motor from QCC (Figure 16 and Figure 17). Due to the poor quality of elution profiles of individual subunits of IFT-B core complex, our systematic dissection of QCC/OSM-3 interaction has been compromised.

The interaction of OSM-3 with QCC is indeed strong as shown in the MST assays (Figure 18). This interaction has been abolished by the removal of DYF-1. Collectively, these results represent the first evidence reporting a direct interaction between OSM-3 and DYF-1, which is consistent with previous in vivo observations showing that in DYF-1 mutants, OSM-3 dissociates from its IFT cargo. Taken together, our results along with the in vivo reports demonstrate that the DYF-1 subunit is the sole recruiter of the OSM-3 to its IFT-B cargo. Yet, the interaction of DYF-1 and QCC with OSM-3 motor requires more characterization in vitro.

Notably, the previous SEC-MALS results showing that TCC, QCC, QCC + OSM-3, IFT-B core complex, and IFT-B core complex + OSM-3 contain one copy of each protein are somewhat surprising because electron-tomographic analysis of IFT particles in situ revealed formation of multimegadalton IFT trains in flagella of *C. reinhardtii* [15]. It is therefore tempting to think that some

IFT subunits have the ability to multimerize in order to form trains in vivo. Although the underlying molecular mechanisms of the multimerization processes are still unknown, factors like phosphorylation might be involved in regulating these processes (see part II for details).

The fact that OSM-3 displays no movement in DYF-1 mutant animals using time-lapse fluorescence microscopy made us to ask whether DYF-1 influences the motility of OSM-3. To better understand the molecular basis of this question, it is important to characterize the properties of the DYF-1/OSM-3 complex in in vitro motility assays. We therefore turned to fluorescence-based single molecule techniques to directly visualize movements of OSM-3 motor and its IFT-B cargos. To this end, photobleaching and colocalization experiments were first carried out showing that the corresponding subunits and complexes neither form aggregates owing to fluorescence functionalization nor dissociate due to different dilutions factors used in the TRIF assays, respectively (Figure 19 and Figure 20). This was followed by in vitro transport assays showing that the DYF-1 subunit activates the autoinhibited wild type OSM-3 motor for a directional transport with transport rates of ~1.2 µm/s similar to those observed in vivo (Figure 28, Figure 29, and Supplementary video 2 and 3). Strikingly, DYF-1-containing QCC fully unleashed the motor's activity in vitro, as the motor speed has been enhanced from ~1.2 µm/s to ~1.8 µm/s (Figure 24, Figure 25, Figure 28, and Figure 29). Furthermore, neither the IFT-B core complex (7 subunits) nor the entire IFT-B complex (14 subunits) could increase the motor speed further than ~1.8 µm/s, suggesting that QCC is the minimal complex needed for full activation of the motor in vitro (Figure 27).

Intriguingly, the ~1.8 µm/s speed has never been reported before, to our knowledge, neither in vivo nor in vitro. All previous studies have only detected a ~1.2 µm/s speed rate of OSM-3 motor. However, in a recent study from the Peterman lab, the authors showed that IFT trains are transported through the transition zone by kinesin-II at its ~0.5 µm/s speed [58]. Once IFT trains pass the transition zone, kinesin-II motor gradually detaches from IFT trains, which is concurrently accompanied by a gradual attachment of OSM-3 motor to guarantee an efficient handover of trains. This in turn results in a gradual increase in the speed of IFT trains reaching ~1.3 µm/s at the tip of the middle (proximal) segment [58]. Strikingly, IFT trains are transported along the distal segment solely by OSM-3 reaching a speed of ~1.5 µm/s at the terminal end of the segment [58].

These novel findings showing for the first time that OSM-3 reaches a speed of ~1.5 µm/s in vivo may support the idea that the ~1.8 µm/s speed of OSM-3, which has been detected in our motility assays, can indeed be achieved in vivo by OSM-3, but due to presence of additional specific regulatory factors (e.g., kinases) that are absent in our in vitro assays, the velocity of OSM-3 is

decreased in vivo [104, 112]. Previous in vivo results showed that the DYF-5 kinase regulates OSM-3 speed in amphid and phasmid cilia of *C. elegans* [104].

Another plausible explanation is that the slower kinesin-II motor and the faster OSM-3 motor are in mechanical competition. Either the faster OSM-3 motor drags forward the slower kinesin-II motor or the slower kinesin-II pulls back the faster OSM-3 motor, which in any case leads to slowing down of the OSM-3 motor in vivo. The idea that the faster OSM-3 motor drags forward the slower kinesin-II motor is supported by the in vivo findings demonstrating that kinesin-II motors are completely absent in the handover zone in *C. elegans* mutants lacking OSM-3 function, suggesting that OSM-3 motors pulls kinesin-II motors further along the middle segment than they travel by themselves [58]. This of course reduces OSM-3 speed from ~1.5 µm/s to ~1.3 µm/s [58].

To better understand the regulation of OSM-3 activity in vivo which is crucial for its ciliary functions, it is important to reveal the underlying molecular mechanisms of OSM-3 full activation in vitro. Thus, generating stepwise truncation constructs will reveal the minimum length that is needed to hold DYF-1 and OSM-3 together in a stable complex. The same approach can also be followed in the case of QCC and OSM-3. The outcomes of this step will provide indications about which residues of DYF-1 can relieve the autoinhibition mechanism of OSM-3 and whether OSM-3 needs the whole QCC (4 subunits) for full activation or a minimal interaction interface is sufficient to do so.

It is also important to check whether the full activation mechanism of OSM-3 affects the frequency of IFT trains, the ultrastructure of the cilium, or the regulation of the ciliary length in vivo. Previous studies have linked the velocity of IFT to the ciliary length control. Increased velocity of anterograde trains contributes to elongation of cilia, whereas decreased velocity is associated with short cilia [121]. Finally, single molecule optical tweezers experiments of OSM-3 motor (~1.2 µm/s) displayed a stall force of 6 pN [59]. This therefore raises the question does the full active motor (~1.8 µm/s) possess a different stall force? If so, what are the resulting effects of this force on kinesin-II/OSM-3 motors functional coordination? And in a broader context, what are the consequences on complex formation between IFT-A/ kinesin-II and IFT-B/OSM-3?

The functional transport assays used in this study revealed the direct and pivotal roles of the DYF-1 subunit in recruitment of the OSM-3 motor into its physiologically relative context, which in turn further activates the motor for an efficient transport. Curiously, a similar activation mechanism has recently been observed in kinesin-2 motor from *C. reinhardti* [68]. As mentioned before, the kinesin-2 is a heterotrimeric motor complex comprising two motor subunits (FLA-8/FLA-10) that form

heterodimer and a non-motor subunit (KAP-1). The association of the KAP-1 subunit with the heterodimer motor subunits is known to be required for proper IFT in a wide variety of organisms ranging from *C. reinhardtii* to mammals [68]. The exact roles of the KAP-1 subunit in the context of IFT are ambiguous, although it has been speculated that the KAP-1 subunit might regulate kinesin-II motor's activity [60]. This speculation was recently proved by in vitro observations showing that at saturated ATP conditions, the heterodimeric FLA-8/FLA-10 motor displays a heterogeneous velocity distribution. The slower velocity of ~ 0.9 µm/s corresponds to the autoinhibited wild type motor and the faster velocity of ~ 2 µm/s corresponds to the in vivo transport rates. Interestingly, addition of the KAP-1 subunit led to suppression of the autoinhibition of the heterodimeric FLA-8/FLA-10 motor via abolishing the slow movement rates leaving the motor fully activated [68].

Taken together, our results in *C. elegans* along with these novel findings in *C. reinhardtii* represent a functional reciprocity that is particularly notable given the complexity of the IFT machinery and suggest that the adaptor-dependent recruitment and activation mechanisms of kinesin-2 motors might be conserved between these two organisms [68, 110]. Revealing the underlying activation and recruitment mechanisms of the mammalian kinesin-2 motor (KIF3A/KIF3B/KAP3) will surely close the gaping hole toward understanding whether or not the recruitment and the activation mechanisms of kinesin-2 motors to their physiologically relevant context are universally conserved.

Intriguingly, in the absence of kinesin-II motor, OSM-3 motor alone can build the full-length sensory cilium of *C. elegans* [67]. This odd feature of *C. elegans* suggests that these two motors function redundantly in sensory cilia. It brings up the question why *C. elegans* uses two motors to build its sensory cilia if one can do the job alone? The only explanation is that the speed of IFT trains matters for controlling some ciliary processes such as regulation of ciliary length, trains frequency, and ferrying additional ciliary precursors. Perhaps, *C. elegans* uses two kinesin-2 motors to provide its cilia with advantages of functional diversity, including mechanosensation and chemical sensation. Yet, the answer to the previous question remains puzzling [67].

Finally, answering how the OSM-3 is activated for IFT transport intuitively raises the question how the motor gets deactivated at the ciliary tip to be transported as a cargo to the ciliary base by the retrograde dynein motor? It is tempting to think that additional factors that are spatially-located at the ciliary tip (e.g. kinases) are involved in the disruption of OSM-3 motor interaction with its DYF-1 cargo, which in turn leads to OSM-3 deactivation. This can be supported by the findings showing that in mammalian neuroblastoma cells, phosphorylation of the tail region of the KIF-17 motor (a homologue of the *C. elegans* OSM-3 motor) by the CaMKII kinase results in abolishing of the

association between the motor and its Mint1 cargo, which consequently leads to release of this cargo from the transport machinery [122]. Furthermore, in *C. reinhardtii*, the homologue of CaMKII kinase (CrCDPK1) was shown to phosphorylate the kinesin-II motor subunit FLA-8. This phosphorylation regulates the IFT entry at the ciliary gate and loading/unloading at the ciliary tip. At the ciliary base, phosphorylation of the FLA-8 subunit by the CrCDPK1 kinase prevents the kinesin-II motor from entering the cilium, whereas at the ciliary tip, phosphorylation of the FLA-8 subunit leads to deactivation of the kinesin-II motor and abolishing its association with the IFT-B complex [123]. In sensory cilia of *C. elegans*, the conserved mitogen-activated protein (MAP) kinase DYF-5 was shown to be involved in docking and undocking of kinesin-2 motors (kinesin-II and OSM-3) onto IFT trains during anterograde transport presumably by changing the affinity between these motors and their IFT complexes. Additionally, this kinase was shown to modulate the speed of OSM-3 motor in vivo [104].

4 Summary

The physiological relevance of our in vitro results is complemented by the previous in vivo findings in the sensory cilia of *C. elegans* showing that in the absence of DYF-1 function, OSM-3 not only detaches from IFT trains but also it fails to move directionally along the ciliary axoneme [69]. This finding can now be explained by the direct role of the DYF-1 subunit in recruitment and activation of the OSM-3 motor as shown in part I of this study. These results collectively represent a notable example of reinforcement of in vitro findings to in vivo studies to pinpoint the specific functions of an individual IFT subunit.

Daunting the complexity of the IFT machinery, this work provides novel insights into the molecular basis of how a kinesin motor is integrated into IFT trains for efficient transport, and is an example of the power of bottom-up reconstitution approaches to decipher the underlying molecular mechanisms of highly convoluted processes such as ciliogenesis. Finally, given that one subunit playing the key role in the specific motor recruitment and activation, our results now propose a simple model for the spatial regulation of OSM-3-driven IFT trains in vivo (Figure 30).

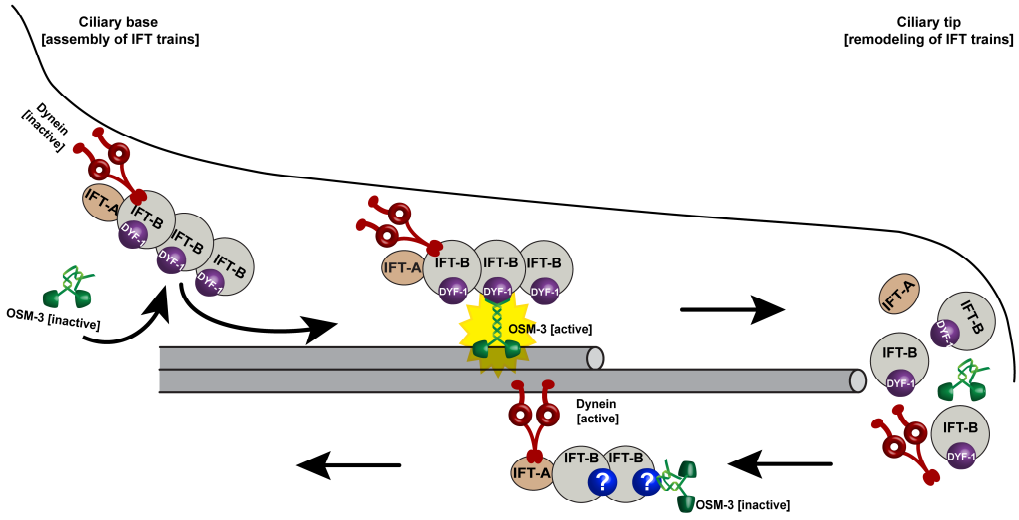

Figure 30: Proposed model showing the regulation mechanism of OSM-3-dependent IFT in vivo. The specific, DYF-1-dependent recruitment of the OSM-3 to the IFT-B complex acts as an on-switch for the autoinhibited motor during the IFT process. Because the DYF-1 subunit is the sole activator of the motor, simply disrupting this interaction would suffice to inactivate the OSM-3 during remodeling at the ciliary tip. The factors involved in the inactivation of the motor are not yet known. The inactive motor is transported back on the dynein-driven retrograde trains to the ciliary base for recycling.

Part II

5 Molecular mechanisms of IFT train assembly and remodeling

5.1 IFT complexes form trains of megadalton sizes

As mentioned previously, IFT is a highly regulated process that occurs in consecutive steps: (a) IFT components (motor proteins, IFT particles, BBSome, soluble building blocks of tubulins, and some other protein cargos) first accumulate at the ciliary base, (b) by some anonymous mechanisms these components form trains that eventually are allowed to enter the cilium through the TZ gate in a kinesin-2 dependent manner and (c) move processively toward the ciliary tip carrying the oppositely directed dynein-2 motor as a passenger, (d) upon arrival at the ciliary tip, trains undergo restructuring, different cargos are unloaded, turnover products are loaded, kinesin-2 motors are deactivated, and finally retrograde dynein-2 motors are activated to (e) drive retrograde IFT trains back to the ciliary base where (f) they get disassembled and recycled for another IFT transport. However, factors that control assembly and remodeling of IFT trains are elusive.

The IFT particles consist only of 22 protein subunits (see section 1.6.2 and 1.6.3), identified to the date, and organized into two biochemically stable complexes: the IFT-A contains 6 proteins and the IFT-B contains 16 proteins. Several studies have detected numerous direct protein-protein interactions between the IFT subunits using materials either purified directly from model organisms such as flagella of *C. reinhardtii* or using recombinantly expressed proteins. In addition, crystal structure studies have provided a detailed map of the interaction landscape of the IFT subunits [124]. Yet, our knowledge on how IFT proteins assemble to form IFT trains of multimegadalton sizes similar to those observed in in vivo is limited.

The ultrastructure of IFT trains has been resolved in 2009 using transmission electron microscopy (TEM) and electron-tomographic analysis of longitudinal sections from *C. reinhardtii* flagella [15]. In this study, two types of IFT trains were measured: long thin trains (~700 nm length) displaying a defined periodicity of 40 nm and short electron-opaque trains with a length of ~250 nm and a periodicity of 16 nm. Moreover, the authors used a *fla14 C. reinhardtii* mutants characterized by a deletion of the LC8 subunit of dynein motor to disrupt the retrograde transport, allowing them to conclude that the long thin trains correspond to the anterograde transport, whereas the short compact trains correspond to the retrograde transport [15]. In a striking contrast, a recent study showed that both retrograde and anterograde trains in mature flagella of *C. reinhardtii* have a unified

length of ~200 nm using a time-resolved correlative fluorescence and three-dimensional electron microscopy approaches [81]. Another electron tomography study showed that IFT trains comprise three different architectural types: two short trains (narrow and wide) with ~300 nm length and long trains with ~700 nm length [125]. In addition, the short IFT trains were observed to participate in anterograde transport [125]. These discrepancies can be explained by the hypothesis that during the initial rapid growth of flagella, longer IFT trains are more abundant than shorter trains in flagella to transport the building blocks required for axonemal assembly. However, when flagella reach full-length (i.e., become mature cilia) shorter trains become more available than longer trains since fewer flagellar precursors are needed to maintain the axonemal turnover [125].

5.2 Mutual interactions of IFT subunits compromise analysis of specific functions of individual subunits in vivo

The interdependency of the IFT subunits for mutual stability makes it difficult to delineate the specific roles displayed by the individual subunits in IFT regulation in vivo because depletion or deletion of a specific subunit results in formation of severe phenotypes or even complete loss of cilia, which in turn mask the role of the missing subunit. For example, the IFT-B core subunit OSM-6 functions as a central scaffold for the IFT-B complex by displaying several direct interactions with many IFT-B subunits (e.g., OSM-5, DYF-6, and DYF-1) (Figure 6b) [90, 93, 126]. Consequently, deletion of OSM-6 leads to destabilization of IFT trains and even a complete loss of the cilium [127, 128]. It is therefore tempting to believe that the bottom-up reconstitution approach that has been used in part I is the best suited experimental tool to decipher the molecular pathways of the regulation mechanisms of IFT (i.e., assembly and restructuring of IFT trains) and pinpoint the specific functional contributions of each individual subunit in the context of IFT.

Despite the unprecedented progress that has been made by multiple research groups in understanding the molecular basis of IFT, many long-standing questions still remain unresolved till today such as:

(1) How do the 22 subunits of the IFT-A and -B complexes oligomerize into multimegadalton IFT trains with ~700 nm length at the ciliary base?

(2) What are the mechanisms and factors governing IFT trains remodeling at the ciliary tip to initiate the retrograde transport by the dynein-2 motor?

The fact that the same individual components enter and eventually exit the cilium during ciliogenesis, makes it plausible to think of existence of spatio-temporal regulation mechanisms to organize assembly of trains at the ciliary base and reorganize interaction interfaces to allow restructuring of trains at the ciliary tip. So far, there exist only few subunits of the IFT-B complex that have been speculated to be implicated in the remodeling process at the ciliary tip [129, 130]. However, the underlying molecular mechanisms by which these subunits regulate the remodeling process still remain elusive.

5.3 The DYF-5 and DYF-18 kinases are promising candidates to study assembly and remodeling of IFT trains

Cilia contain several types of kinases, but only a few of these kinases have been shown to be implicated in mechanisms of IFT regulation. Of particular interest, two of these kinases are: the so called serine/threonine DYF-5/MAK and DYF-18/CCRK, which have been identified to play regulatory roles in stabilizing interactions between IFT trains and kinesin-2 motors in the sensory cilia of *C. elegans* [104, 112]. In addition, mutations in the DYF-5 kinase lead to accumulation of IFT proteins at distal tips of axonemes, implicating the regulatory roles of the kinase in the remodeling process of IFT particles [104, 112].

Given the intricacies of IFT, identification of the specific targets of kinases among IFT particles is difficult in vivo. This causes major setbacks to reveal the molecular mechanisms of the phosphorylation-regulated processes. We therefore sought to investigate the direct phosphorylation targets and the functional consequences of the DYF-5 and DYF-18 kinases at the molecular level using the purified IFT components of *C. elegans*. To this end, the data presented here hold promise to provide the first molecular insights into the convoluted regulation mechanisms of IFT trains assembly and remodeling in vivo.

5.4 The DYF-5 and DYF-18 kinases display a site-specific localization in the cilium

To determine their precise functions in cilia, the ciliary localization pattern of the DYF-5 and DYF-18 kinases must first be examined. For this purpose, we have collaborated with the Ou group (Tsinghua University, Beijing, China) who made use of the CRISPR/Cas9 technology to endogenously co-express DYF-5::GFP, DYF-18::mScarlet, and the most commonly used IFT marker OSM-6::BFP under the control of the P*dyf-1* promoter in the same worm. The respective fluorescence intensities

of the previously mentioned proteins were quantified along the transition zone, the middle segment, and the distal segment of the ciliary axoneme of the sensory amphid and phasmid cilia of *C. elegans*. Interestingly, the DYF-5 kinase was shown to abundantly localize to the ciliary tip, whereas the DYF-18 kinase is mostly localized to the ciliary base (unpublished data). Given the fact that IFT train assembly takes place at the ciliary base, whereas train remodeling occurs at the ciliary tip, and the localization pattern of the DYF-18 and DYF-5 kinases between the tip and the base, respectively, we hypothesized that these kinases might be involved in distinct phosphorylation-regulated, site-specific processes of IFT in vivo.

5.5 Revealing the phosphorylation targets of the DYF-5 and DYF-18 kinases among the IFT-B subunits

As mentioned before, identification of the specific phosphorylation targets of the DYF-5 and the DYF-18 is a major obstacle toward understanding the functional consequences of phosphorylation-mediated processes in vivo. Therefore, we asked whether any of our recombinantly expressed IFT-B subunits of *C. elegans* (14 subunits) are targets for phosphorylation by DYF-5 and DYF-18 in vitro. In order to answer this question, the Flag-tagged IFT-B subunits were individually purified (see section 8.3.4), and their concentrations were adjusted accordingly to assure that all proteins roughly lie in the same concentration range during the phosphorylation assays (Figure 31a). Then, the proteins were individually mixed with equimolar concentrations of purified DYF-5 and DYF-18, and finally subjected to kinase assay (see section 8.3.6). Interestingly, the kinases could phosphorylate a subset of six subunits from the IFT-B complex: two subunits (DYF-6 and DYF-11) were targeted by both DYF-5 and DYF-18, while the remaining subunits were targeted by either DYF-5 (IFT-74 and OSM-5) or DYF-18 (CHE-13 and DYF-3) (Figure 31b, c).

The interaction interface between IFT-B core and peripheral complexes is highly conserved from unicellular organisms to mammals. It comprises four subunits: two subunits (OSM-6 and OSM-5) belong to the IFT-B core complex, while the other two subunits (CHE-13 and DYF-3) belong to the IFT-B peripheral complex (Figure 6b). Notably, three subunits (OSM-5, CHE-13, and DYF-3) of the total four subunits forming the conserved interface are exclusive targets of phosphorylation. Thus, the strategic localization of these subunits provoked the following question.

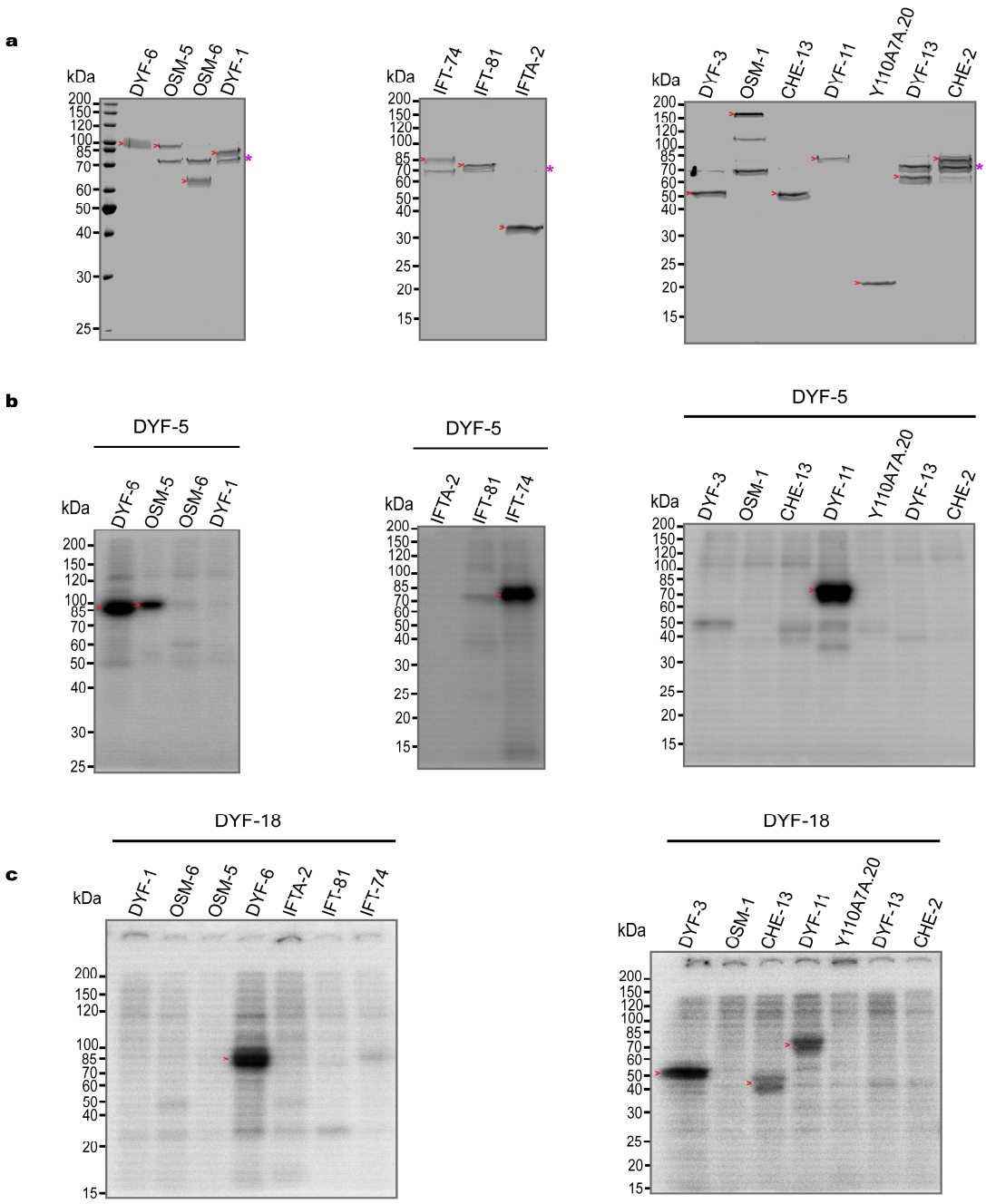

Figure 31: Six of the 14 subunits of the IFT-B complex are kinase targets. (a) SDS-PAGE gels show the relatively similar concentrations of the 14 subunits forming the IFT-B complex. **(b)** And **(c)** Autoradiographs show the DYF-5 and DYF-18 phosphorylation targets from IFT-B subunits, respectively. The DYF-5 targets are DYF-6, OSM-5, IFT-74, and DYF-11, whereas the DYF-18 targets are DYF-6, DYF-3, CHE-13, and DYF-11. The molecular weight ladder (kDa) is shown on the left. The corresponding protein and phosphorylation bands are depicted by red arrow heads. Asterisks in **a** refer to the HSP70 protein band.

5.6 Can phosphorylation substantially interfere with the structural properties of the conserved interaction interface?

To assess the functional implications of phosphorylation on the structural properties of the interaction interface, the untreated CHE-13 and DYF-3 proteins and the DYF-18-phosohorylated CHE-13 and DYF-3 proteins were subjected to SEC-MALS analysis. Intriguingly, the untreated CHE-13 protein displayed a monomeric peak with a molecular weight of 53 kDa judged from MALS analysis, on the contrary, the DYF-18-phosohorylated CHE-13 eluted under the void peak, indicating that phosphorylation induces aggregation/oligomerization of the CHE-13 subunit (Figure 32a). Notably, the same behavior has been observed for the DYF-3 subunit (Figure 32b).

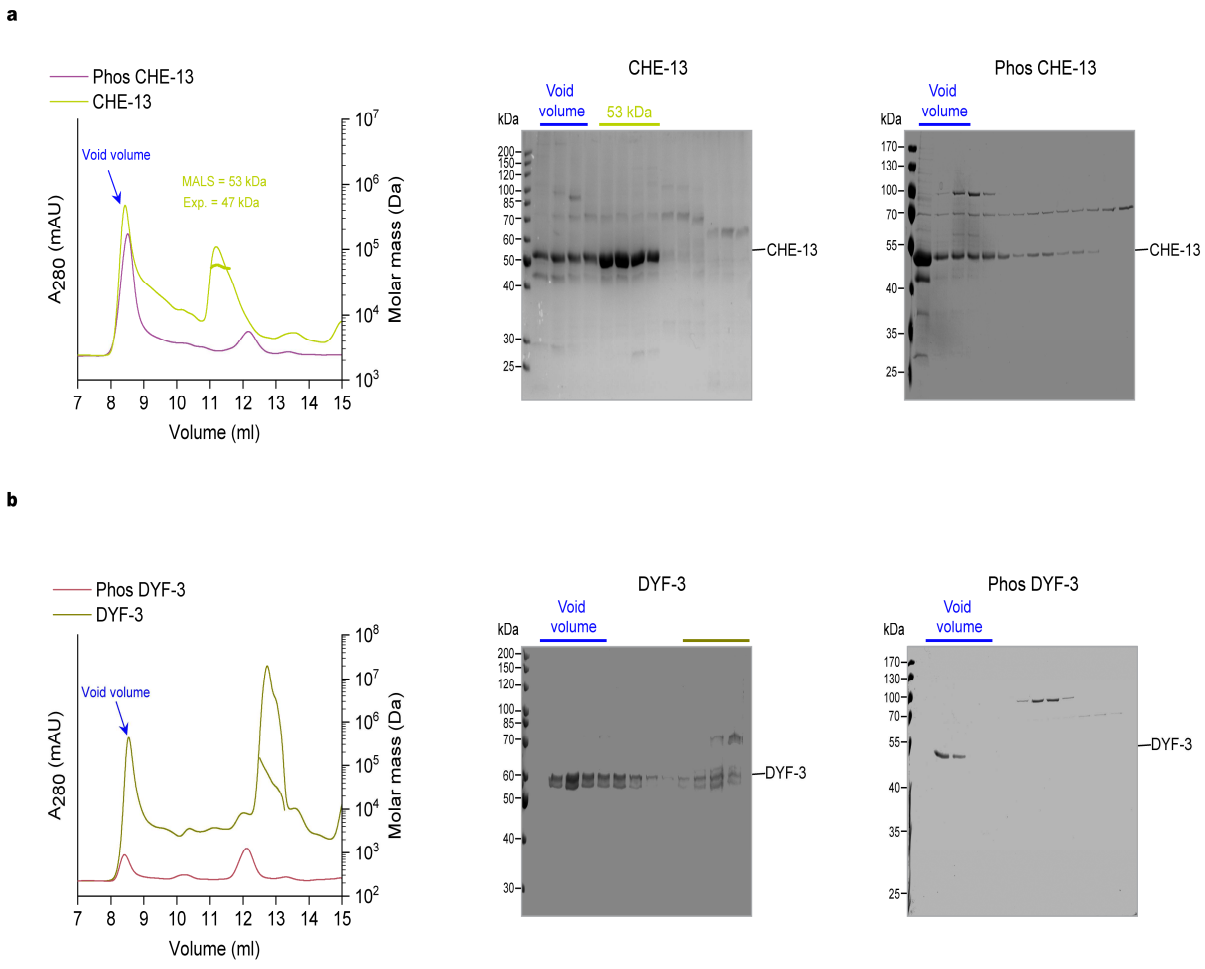

Figure 32: Phosphorylation induces oligomerization of the IFT-B peripheral subunits. (a) The monomeric peak of mock CHE-13 with 53 kDa disappears after phosphorylation by DYF-18 (left). While a significant amount of mock CHE-13 protein eluted in the fractions of the monomeric peak, most of the phosphorylated CHE-13 protein eluted in the void fractions, suggesting aggregation/multimerization of CHE-13 after phosphorylation (middle versus right). **(b)** DYF-3 also tends to form oligomers upon phosphorylation. The SEC-MALS profile of the untreated DYF-3 shows an unstable monomeric peak with a heterogeneous distribution of MALS fit that spans from ~150 kDa to ~10 kDa. SDS-PAGE gels show that phosphorylation results in elution of all amount of DYF-3 in the void fractions (middle versus right). The proteins were purified using the Superdex 200 Increase 10/300 GL column.

Taken together, these results support our hypothesis that the formation of IFT trains at the ciliary base may indeed be regulated in a phosphorylation-dependent manner in vivo.

5.7 Phosphorylation induces disassembly of DYF-11

DYF-11 is recently proposed to be implicated into the remodeling process of IFT trains, however, the exact mechanism by which this subunit functions at the ciliary tip remains to be revealed [130]. Being a phosphorylation target of the spatially-localized DYF-5 and DYF-18 kinases, we asked whether phosphorylation interferes with the DYF-11 structural integrity. To this end, the untreated DYF-11, and the DYF-5- and the DYF-18-phosphorylated DYF-11 were subjected to SEC-MALS analysis. The untreated DYF-11 displayed an oligomeric, well-defined peak with a molecular weight of 210 kDa compared to 58 kDa the theoretical molecular weight of DYF-11 (Figure 33). Strikingly, phosphorylation by DYF-5 and DYF-18 kinases resulted in disassembly of a significant amount of the ~210 kDa complex into monomers of DYF-11 with molecular weights of 67 kDa and 62 kDa, respectively (Figure 33). Consistent with our observations, the mNeonGreen (NG)-tagged *C. reinhardtii* homologue of DYF-11 (IFT-54) was shown to display a bright fluorescence signal when compared to other IFT fluorophore-labeled subunits, implying that the DYF-11 subunit form indeed a higher order oligomer in vivo [131]. Additionally, a recent publication showed that the DYF-11 can indeed form a higher order oligomer in the sensory cilia of *C. elegans*, as observed in our in vitro assays [132]. Noteworthy, at the moment, it is hard to judge whether the 210 kDa corresponds to a trimer or a tetramer of DYF-11 because such distinction is not trivial in SEC-MALS analysis. With more sophisticated techniques such as cryo-EM, we will be able to tell whether DYF-11 is a trimer or a tetramer.

Despite sharing a mutual domain architecture (CH domain at the N-terminal and coiled-coil domain at the C-terminal) (Figure 6a), DYF-11 displays an opposite behavior than that observed in DYF-3 and CHE-13 upon phosphorylation. Phosphorylation induces aggregation/oligomerization of DYF-3 and CHE-3, in contrast, it induces disassembly/monomerization of DYF-11 (Figure 32 versus Figure 33). This therefore leads to the hypothesis that preventing phosphorylation of CHE-13 and DYF-3 subunits will have a pronounced impact on anterograde train frequency and/or assembly at the ciliary base, whereas abolishing phosphorylation of DYF-11 subunit will affect retrograde trains frequency and/or disassembly of anterograde trains at the ciliary tip. However, this speculation needs to be validated by in vivo experiments (by the Ou group).

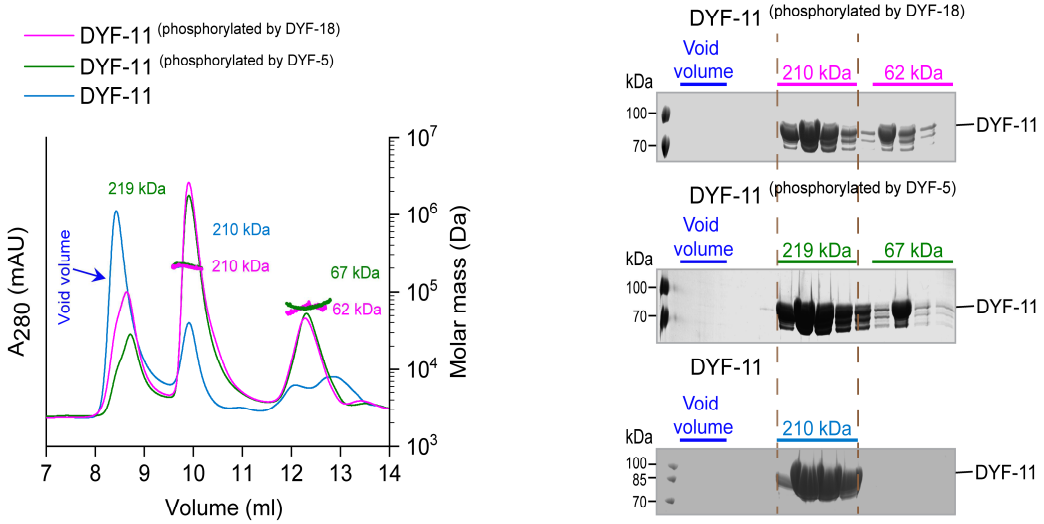

Figure 33: Phosphorylation interferes with the oligomerization properties of DYF-11. Overlay of the elution profiles of the wild type recombinantly expressed and phosphorylated DYF-11 protein (left). The blue chromatogram represents the untreated DYF-11, the green chromatogram represents the DYF-5-phosphorylated DYF-11, and the pink chromatogram represents the DYF-18-phosphorylated DYF-11. Inset MALS fits and chromatograms are color coded. Coomassie-stained SDS-PAGE gels (right) of the corresponding elution profiles. After phosphorylation by DYF-18 and DYF-5, monomeric fractions of DYF-11 with 62 kDa and 67 kDa appeared, respectively (right). Note that these fractions are absent in case of untreated DYF-11 (bottom right). The SDS-PAGE gels of all elution profiles were cropped and aligned together for easier comparison. The dashed brown lines separate the oligomeric peak fractions form the monomeric peak fractions of DYF-11. The factions under the void peak of all three mentioned chromatograms were resolved onto SDS-PAGE gel. Purification was carried out on Superdex 200 Increase 10/300 GL column.

Given that phosphorylation induced disassembly of DYF-11, we asked whether dephosphorylation induces even more oligomerization of DYF-11 than that observed in the wild type construct (i.e., > 210 kDa). To this end, DYF-11 was dephosphorylated using Antarctic Phosphatase enzyme (see section 8.3.5) and subjected to SEC-MALS analysis. Dephosphorylation showed no impact on the oligomeric state of DYF-11 (Figure 34). The molar mass of the dephosphorylated DYF-11 is roughly similar to the wild type, untreated DYF-11 (220 kDa vs 210 kDa, respectively, (Figure 34 versus Figure 33).

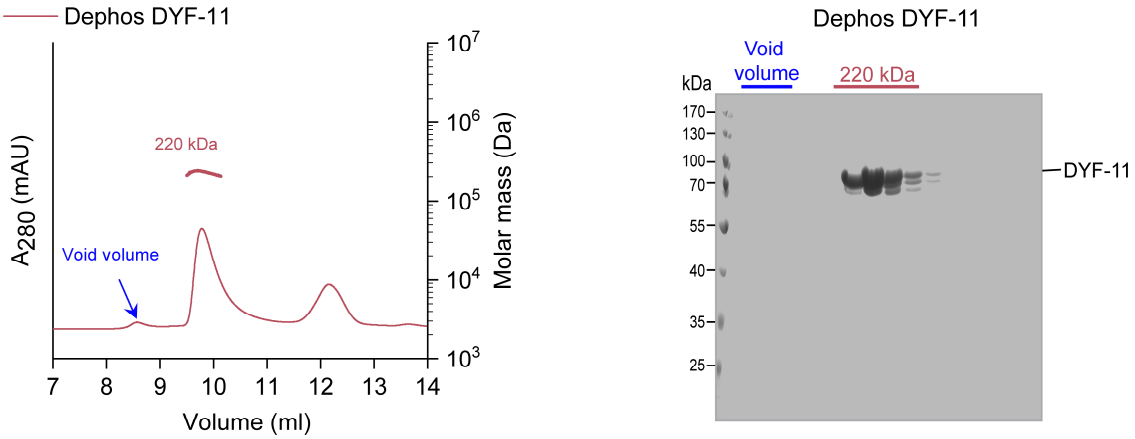

Figure 34: Dephosphorylation does not increase the higher order oligomerization of DYF-11. The SEC-MALS profile (left) shows that the molecular weight of the dephosphorylated DYF-11 (220 kDa) is indistinguishable in comparison to the molecular weight of untreated DYF-11 (210 kDa, see Figure 33). The fractions of the MALS peak along with the void volume were resolved onto SDS-PAGE gel (right). The Purification was carried out on the Superdex 200 Increase 10/300 GL column.

5.8 DYF-11 associates with Y110A7A.20 via its distal C-terminus

IFT subunits are known to form networks of interactions with one another (Figure 6b). The stability of the IFT complexes relies on the reciprocal interaction relationship between the subunits. Y110A7A.20 subunit is the well-characterized binding partner of DYF-11 as demonstrated in several model organisms [92, 133, 134]. The N-terminal region of DYF-11 contains a calponin homology domain (CH domain), whereas the C-terminal region contains a coiled-coil domain (Figure 35). The CH domain is shown to bind to tubulins/MTs and is not essential for ciliogenesis, on the other hand,

the C-terminal coiled-coil-2 domain is required for ciliogenesis and interaction with the C-terminal coiled-coil of Y110A7A.20 to form a heteromeric complex [92, 130].

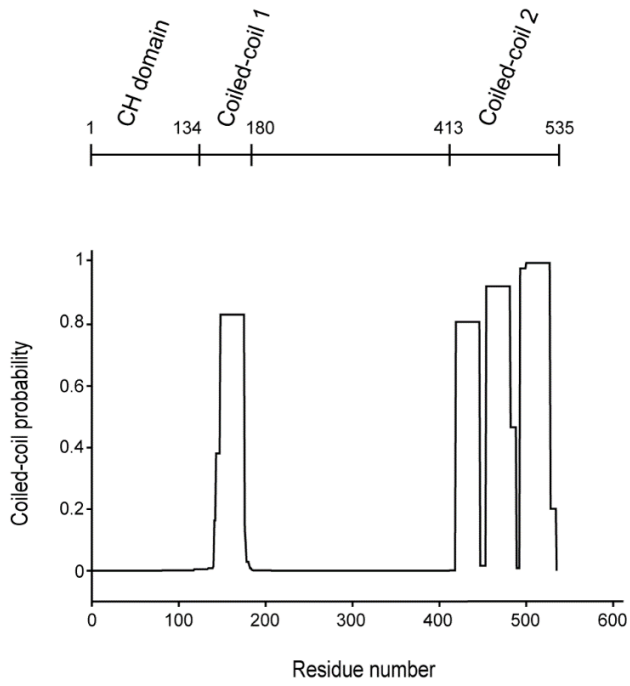

Figure 35: Domain architecture of DYF-11. Domain architecture of DYF-11 reveals the positions of CH, coiled-coil 1, and coiled coil-2 domains (top) based on the previous findings in *C. reinhardtii*. Coiled-coil predictions (bottom) of DYF-11 construct. Domain sizes are shown roughly proportional to the length of the sequence in each domain. The website: https://embnet.vital-it.ch/software/COILS_form.html has been used to calculate the probability of coiled-coil formation**.**

To characterize the interaction of DYF-11 with Y110A7A.20 in *C. elegans*, we designed a Flag-tagged truncation constructs of DYF-11 by removing the N-terminal CH domain (134-535) and the predicted C-terminal coiled-coil 2 domain (1-413). We also designed a Y110A7A.20 construct containing a His-tag at the N-terminal to avoid interfering with the association of Y110A7A.20 with DYF-11 at their C-termini. The Flag-tagged DYF-11 (134-535) and (1-413) truncation constructs were co-expressed with the His-tagged Y110A7A.20 construct. Subsequently, FLAG-tag and His-tag affinity purifications were performed for each co-expression experiment. In consistent with previous findings in *C. reinhardtii*, while removal of the N-terminal domain (134-535) did not interfere with the interaction of DYF-11 with Y110A7A.20, removal of the coiled-coil 2 domain (1-413) completely abolished DYF-11 binding to Y110A7A.20 (Figure 36).

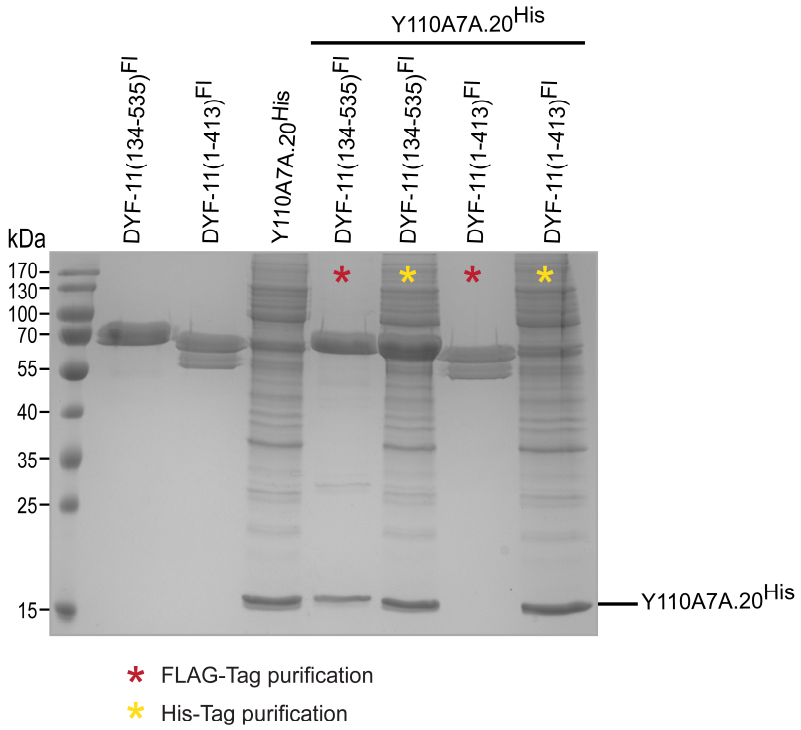

Figure 36: Co-expression assays of the His-tagged Y110A7A.20 with the Flag-tagged DYF-11 truncation constructs. The Coomassie-stained SDS-PAGE gel shows the co-precipitation of the differentially-tagged Y110A7A.20 with the truncated DYF-11 constructs, respectively. The molecular weight ladder (kDa) is shown on the left. The following three lanes show the single expression of the respective constructs that are used in the co-precipitation assay as a size control (Fl =Flag-tag, His=6x-His tag). The color-coded asterisks indicate the purification tag used for the co-precipitation after co-expression of the Y110A7A.20 with the truncated DYF-11 constructs. The last two lanes show that in the absence of its C-terminal coiled-coil domain 2, the DYF-11 (1-413) construct cannot co-precipitate the His-tagged IFT-20 subunit.

5.9 DYF-11 binding stabilizes Y110A7A.20 subunit

The stability of Y110A7A.20 relies on the presence of DYF-11 not vice versa as shown in previous in vivo findings in *C. elegans* [130]. In agreement with this notion, DYF-11 was shown to be a stable subunit alone as previously reported in our gel filtration results (the blue trace in Figure 33); however, the recombinantly expressed Y110A7A.20 subunit with a molecular weight of 16 kDa is unstable on its own judged from the heterogeneous distribution of its MALS fit (Figure 37 left). The instability of Y110A7A.20 is, on the other hand, completely abolished when co-purified with its binding partner DYF-11, as the DYF-11/Y110A7A.20 is eluted from the column as a stable heteromeric complex

with a molecular weight of 215 kDa (the blue MALS fit in Figure 38). This molecular weight is practically indistinguishable from the molecular weight of DYF-11 alone (210 kDa) (compare the blue MALS fits in Figure 38 and Figure 33). It is challenging to gauge the exact stoichiometry of Y110A7A.20 with its 16 kDa in the DYF-11/Y110A7A.20 complex using SEC-MALS. Thus, other techniques are required for this purpose.

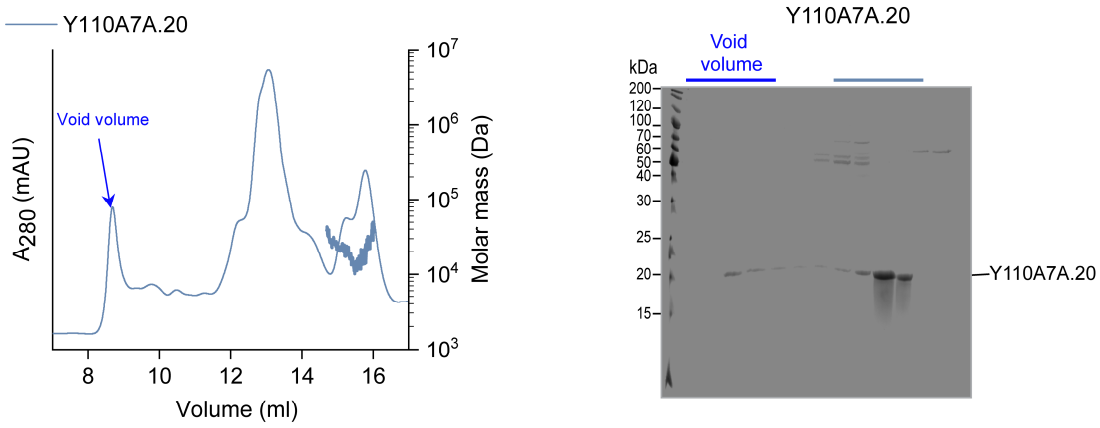

Figure 37: The Y110A7A.20 subunit is highly unstable alone. The elution profile (left) shows the heterogeneous distribution of the MALS fit of the Y110A7A.20 subunit as an indication of instability. The Coomassie-stained SDS-PAGE gel (right) of Y110A7A.20 peak fractions and the void peak. The protein was purified using the Superdex 200 Increase 10/300 GL column.

5.10 Can Y110A7A.20 protect DYF-11 from phosphorylation-induced disassembly?

To determine whether binding to Y110A7A.20 has any potential regulatory effects on the phosphorylation-induced disassembly of DYF-11, the heteromeric DYF-11/Y110A7A.20 complex was phosphorylated by DYF-5/DYF-18 kinases and then subjected to gel filtration. The SEC-MALS analysis showed that Y110A7A.20 protects DYF-11 from phosphorylation-induced disassembly (Figure 38). The elution profile of the phosphorylated DYF-11/Y110A7A.20 complex displayed a splitted peak. The left part of the peak with a molecular weight of 267 kDa corresponds to DYF-11 alone, whereas the right part with 215 kDa corresponds to DYF-11/Y110A7A.20 complex (the brown trace in Figure 38 left), which is also shown in the corresponding SDS-PAGE gel (Figure 38 right). Intriguingly, phosphorylation of the DYF-11/Y110A7A.20 complex failed to induce monomeric

fractions, which have been observed previously with the phosphorylated DYF-11 (Figure 33 versus Figure 38).

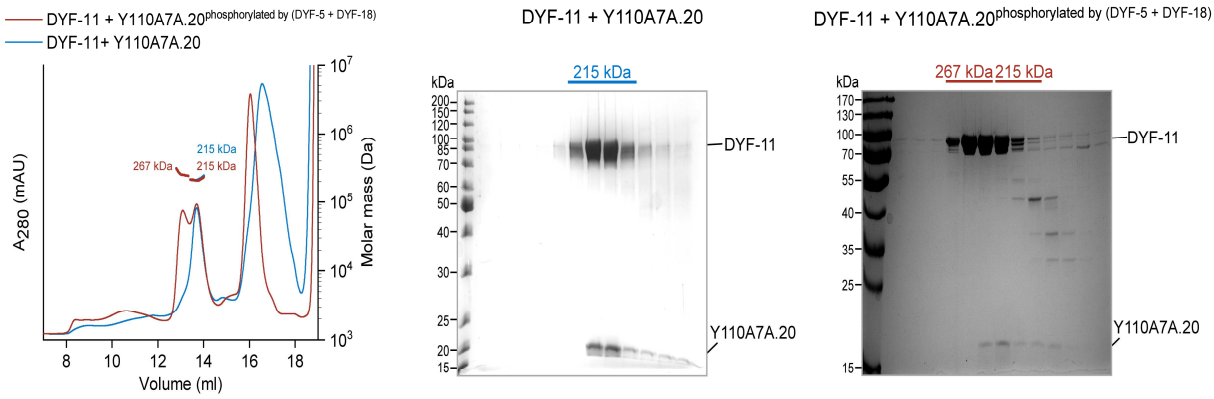

Figure 38: The Y110A7A.20 subunit prevents phosphorylation from interfering with the structural integrity of DYF-11. The blue trace represents the SEC-MALS profile of the mock DYF-11 + Y110A7A.20 complex, whereas the brown trace corresponds to the SEC-MALS profile of the DYF-5 and DYF-18-phosphorylated DYF-11 + Y110A7A.20 complex (left). MALS fits and chromatogram traces are color coded. SDS-PAGE analyses of the protein fractions under the respective elution profiles (middle and right). Note that DYF-11 and Y110A7A.20 elute under the same peak, indicating formation of a stable complex. Y110A7A.20 abolishes the effect of phosphorylation-induced monomerization of DYF-11 (for comparison see Figure 33). The longer peaks on the right side of the SEC-MALS profiles belong to the FLAG peptides that have been used for eluting the proteins off the FLAG- resin. Gel filtration was carried out using the Superose 6 Increase 10/300 GL column.

Taken together, our preliminary data hold promise to provide the first insights into the direct impacts of ciliary kinases on the structural integrity of IFT trains at the ciliary base (i.e., assembly) and the ciliary tip (i.e., remodeling).

5.11 Kinases and loading/unloading of tubulins

Cilia assembly depends mainly on the availability of building blocks of tubulin protein, the major structural component of cilia that is transported by IFT. Tubulins are loaded onto IFT trains at the ciliary base, transported along the ciliary axoneme, and eventually unloaded at sites of axonemal assembly. To control their ciliary length, cilia balance between axonemal assembly and disassembly rates that are regulated by IFT [104]. During the cilium growth, IFT trains are highly loaded with tubulins, whereas during steady-state cilium length, IFT trains are less occupied with tubulins [94].

The underlying molecular basis governing loading/unloading of the building blocks of tubulin is unknown.

Only three subunits of IFT-B complex have so far been identified to form main binding domains for tubulin transport. The N-termini of the IFT-B core subunits IFT-81 and IFT-74 form a module for tubulin binding with a μM affinity. This process takes place as follows: first, the N-terminal domain of the IFT-81 functions as a recognition site, which weakly binds to the globular domains of α and β tubulins. Second, the positively charged N-terminal domain of the IFT-74 binds to the negatively charged E-hooks of β tubulins, which in turn enhances the weak association of IFT-81 with tubulins by ~18 fold [107]. A second tubulin binding domain has been revealed in the N-terminal CH domain of the IFT-54 (DYF-11) [92]. These two tubulin binding modules match the building kinetics of cilia. Consistently, in our in vitro microtubules decoration assays, the *C. elegans* homologues IFT-81, IFT-74, and DYF-11 are shown to bind to microtubules (Figure 39).

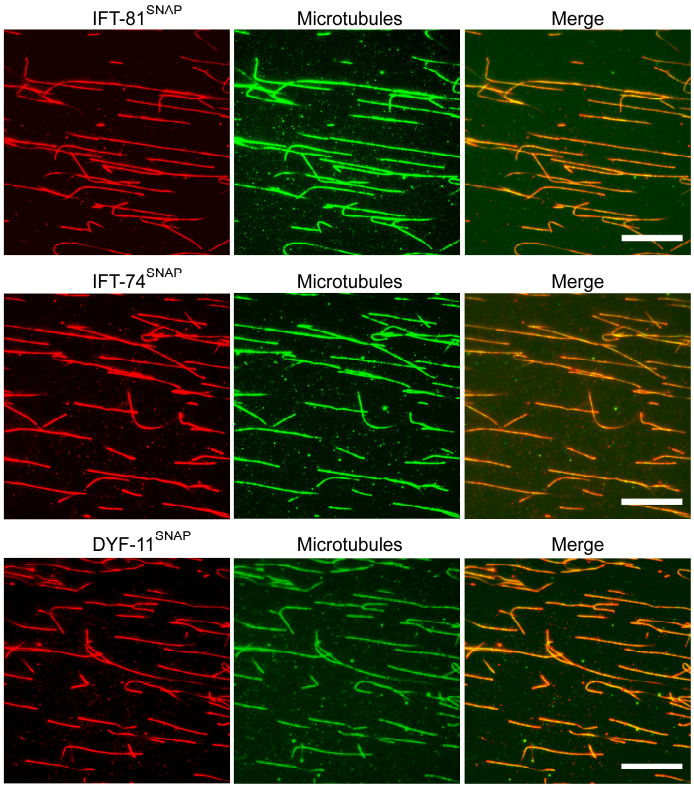

Figure 39: Association of IFT-B subunits with microtubules. The C-terminal, SNAP-tagged IFT-81, IFT-74, and DYF-11 robustly decorate the surface-immobilized, Atto488-labeled microtubules. Scale bars, 10 μm.

Several kinases were shown to be responsible for controlling ciliary length. Of particular interest, activities of DYF-5 and DYF-18 kinases are known for regulating ciliary length. For example, the length of the sensory cilium of *C. elegans* increases in the loss of DYF-5 and DYF-18 function mutants, whereas overexpression of both kinases leads to formation of shorter cilia [104, 112]. As mentioned before, DYF-18 and DYF-5 display an exclusive localization pattern between the ciliary base and the ciliary tip. With the exception of the IFT-81 that is moderately phosphorylated by the DYF-5 kinase, the other microtubules/tubulin binding subunits IFT-74 and DYF-11 are heavily phosphorylated by the DYF-5 and DYF-18 kinases.

The strategic positioning of DYF-5 and DYF-18 kinases, and the fact that the IFT-B tubulin-binding subunits are targets of phosphorylation suggest that these kinases are involved in the process of tubulin loading and unloading at the ciliary base and ciliary tip, respectively. Perhaps phosphorylation of the respective subunits and assessing their binding to microtubules and tubulins in in vitro decoration and tubulin pull-down assays will give us some hints about the molecular basis of tubulin transport by IFT.

6 Perspectives and future directions

The work presented in this thesis (part I) provides the first detailed insights into how a kinesin-2 motor (i.e., OSM-3) is recruited to its IFT train, and reveals the key regulator subunit that activates OSM-3 motor for efficient IFT in vivo. These results now pave the way to investigate the underlying molecular mechanisms of OSM-3 deactivation at the ciliary tip. Previous in vivo imaging in *C. elegans* showed that the IFT-B complex and the OSM-3 motor pause shortly at the ciliary tip for remodeling whereas the IFT-A complex turnaround immediately [58]. Therefore, the most probable scenario to think of is that the deactivation happens by disrupting OSM-3 interaction with its activator DYF-1 during their pausing time at the ciliary tip (Figure 30). Simultaneous in vivo imaging of DYF-1 and OSM-3 in the same worm will clarify this.

Our work has also showed that the QCC fully unleashes OSM-3 activity in vitro as the motor displayed a transport rate of ~1.8 µm/s, which has been reported for the first time, to our knowledge, in this study. This finding allows us to ask the following questions: what is the functional relevance of the full activation (~1.8 µm/s) of the motor in vivo? And what are the factors involved in keeping the speed of OSM-3 at ~1.2 µm/s instead of ~1.8 µm/s in the cilium? By answering these questions we will be able to achieve a complete understanding of the regulation mechanisms of OSM-3.

The successful assembly of the IFT-B-OSM-3 complex lays the foundation to begin the mechanistic dissection of the IFT-A-kinesin-II complex. The architecture of the IFT-A complex is poorly understood and much less information is available on the structure and functions of its building subunits. However, our lab has been able to recombinantly express all the wild type, full-length IFT-A subunits of *C. elegans* (unpublished data). This enables the dissection of the IFT-A-kinesin-II complex in vitro. To this end, the same strategy that has been used in part I can be applied to assemble the IFT-A complex with its kinesin-II motor. Briefly, co-expression experiments should first be carried out using constructs with different tags to systematically map the interactions between the individual subunits of the IFT-A complex. This can be followed by SEC-MALS of the interacting subunits and hence formation of bigger complexes for subsequent assembly of the whole IFT-A complex. Once the entire IFT-A complex is assembled, the in vitro reconstitution of the kinesin-II-dependent IFT-A can be achieved. The assembly of the IFT-A-kinesin-II complex will reveal the docking site/s of the kinesin-II motor within the IFT-A complex and demonstrate how the kinesin-II motor is functionally regulated in vivo. Finally, the assembly of the IFT-A-kinesin-II complex along with the IFT-B-OSM-3 complex will pave the way for investigating how the slower kinesin-II motor

and the faster OSM-3 kinesin motor function together to transport the IFT trains along the middle segment at an intermediate speed of 0.7 µm/s.

It has been previously shown that in the *bbs-7* and *bbs-8* mutants of *C. elegans*, the IFT particles fall apart into IFT-A and IFT-B complexes, which are then moved separately by kinesin-II and OSM-3 at their distinctive speeds, respectively [69]. Therefore, it has been proposed that the BBS-7 and BBS-8 subunits act as mediators that link the IFT-A and the IFT-B complexes together and stabilize their interaction. However, another later study in *C. elegans* demonstrated that the IFT-A and the IFT-B complexes can remain associated in the absence of the BBSome complex, and that the IFT-A component DYF-2 (the homologue of IFT-144 in *C. reinhardtii*) is critical for the association between the IFT-A and the IFT-B complexes [98]. Thus, whether or not the BBSome complex is required for the association between the IFT complexes awaits clarification. Having obtained a complete list of the stably expressed subunits of IFT-A and IFT-B, SEC-MALS and MST experiments can be carried out to assess whether there are direct interactions between the components of the IFT-A and the IFT-B or the BBSome complex is needed to mediate their association.

In summary, the aforementioned points can act as an experimental platform to reconstitute the entire kinesin-2-driven IFT machinery of *C. elegans* and hence answering why the rod-shaped sensory cilia of *C. elegans* are built by two distinct kinesin-2 motors. Moreover, this will provide valuable insights into the functional coordination between the slower kinesin-II motor and the faster OSM-3 motor. In a broader context, this work will lay the foundation for future studies to investigate the Tug-of-War between the microtubule-based motors and also to investigate the molecular basis of motor regulation and coordination.

In part II, it has been shown that phosphorylation induces oligomerization of CHE-13 and DYF-3 subunits of IFT-B peripheral complex. Next, we will systematically dissect the phosphorylation-dependent oligomerization properties of the assembled CHE-13/DYF-3 heterodimer followed by the whole interaction interface between the IFT-B core and peripheral complexes (CHE-13/DYF-3 + OSM-6/OSM-5). In addition, we will dissect the phosphorylation-dependent complex formation properties of the CHE-13/DYF-3 heterodimer with other interaction partners from the IFT-B peripheral complex that have been reported in *C. reinhardtii*, including DYF-11/Y110A7A.20 heterodimer, OSM-1, and CHE-2 the homologue of *C. reinhardtii* IFT-80 that has been previously shown to form a homodimer, which is consistent with our SEC-MALS results (Supplementary figure 2) [124]. Finally, we will reveal the phosphorylation residues of CHE-13 and DYF-3 subunits using quantitative phosphorylation analysis by mass spectrometry and then mutate them into alanines in

order to check whether we can manipulate the oligomerization states of the respective subunits in vitro. The functional relevance of these residues will be tested in vivo (in collaboration with the Ou group).

In contrast, phosphorylation has been shown to interfere with the structure properties of DYF-11 by inducing its disassembly, and that the Y110A7A.20 subunit protects DYF-11 from phosphorylation-induced disassembly. Therefore, to successfully finalize this project, the following points will be covered:

(1) Identification of the domain that is responsible for the previously reported oligomerization behavior of DYF-11. This can be achieved by SEC-MALS analysis of the designed truncation constructs of DYF-11(134-535 and 1-413).

(2) As with CHE-13 and DYF-3 subunits, the potential phosphorylation sites of DYF-11 will be revealed using quantitative LC-MS/MS analysis. Next, the respective sites will be mutated into alanine or phenylalanine in order to prevent their presumed phosphorylation, which will hopefully allow us to manipulate the oligomerization state of DYF-11 at amino acid level.

(3) Identification of the residues that are essential for the heteromerization of Y110A7A.20 and DYF-11 from. This requires a detailed structural understanding of the higher order coiled-coil formation between DYF-11 and Y110A7A.20 subunits. To this end, we will make use of bi-functional chemical crosslinking of lysine residues that are frequently enriched in the predicted C-terminal coiled-coil domains of DYF-11 and Y110A7A.20 (in collaboration with Dr. Felix Müller-Planitz) to identify crosslinks and obtain a high-resolution structure of DYF-11/ Y110A7A.20 complex, and then build and atomistic model (in collaboration with the Zacharias group, Technische Universität München).

(4) The respective constructs from the aforementioned points should be introduced into *C. elegans* using CRISPR technology to assess their functional consequences in vivo.

7 Materials

7.1 Chemicals and reagents

Name	Company/Location
Acetic Acid	Roth, Karlsruhe
Agarose NEEO ultra-quality	Roth, Karlsruhe
AMP-PNP	Sigma-Aldrich, Taufkirchen
Ampicillin	Roth, Karlsruhe
Ammonium persulfate	Roth, Karlsruhe
Bovine Serum Albumin	Sigma-Aldrich, Taufkirchen
Biotin-Conjugated BSA	Sigma-Aldrich, Taufkirchen
Coomassie® Brilliant blue R 250	Sigma-Aldrich, Taufkirchen
cOmplete™, EDTA-free Protease Inhibitor Cocktail	Roche, Penzberg
DMSO	Roth, Karlsruhe
Methanol ≥99,8 %, p.a.	Roth, Karlsruhe
DTT	Sigma-Aldrich, Taufkirchen
EGTA	Sigma-Aldrich, Taufkirchen
Ethanol ≥99,8 %, p.a.	Roth, Karlsruhe
Glucose	Roth, Karlsruhe
Glycerin ROTIPURAN® ≥99,5 %, p.a.	Roth, Karlsruhe
GTP	Sigma-Aldrich, Taufkirchen
ATP	Sigma-Aldrich, Taufkirchen
2-Propanol ROTISOLV® ≥99,8 %	Roth, Karlsruhe
peqGOLD prestained Protein-Marker IV	PeqLab, Erlangen
peqGOLD Protein-Marker II	PeqLab, Erlangen
Paclitaxel from *Taxus brevifolia*	Sigma-Aldrich, Taufkirchen
PIPES	Sigma-Aldrich, Taufkirchen
Tetracyclin	Sigma-Aldrich, Taufkirchen
Kanamycin Monosulfate	Sigma-Aldrich, Taufkirchen
Triton™ X-100	Sigma-Aldrich, Taufkirchen

TEMED	Roth, Karlsruhe
$MgCl_2 \cdot 6\ H_2O$	Roth, Karlsruhe
NaCl	Roth, Karlsruhe
Sodium azide (NaN3)	Roth, Karlsruhe
Rotiphorese® Gel 30	Roth, Karlsruhe
SDS pellets	Roth, Karlsruhe
ANTI-FLAG® M2 Affinity Gel	Sigma-Aldrich, Taufkirchen
FLAG® Peptide	Sigma-Aldrich, Taufkirchen
Imidazole	Sigma-Aldrich, Taufkirchen
Tween® 20	Sigma-Aldrich, Taufkirchen
Bromophenol Blue	Sigma-Aldrich, Taufkirchen
β-Mercaptoethanol	Sigma-Aldrich, Taufkirchen
Tris (hydroxylmethyl) aminomethane	Roth, Karlsruhe
Glycine	Sigma-Aldrich, Taufkirchen
Streptavidin from *Streptomyces avidinii*	Sigma-Aldrich, Taufkirchen

7.2 Cell culture consumables and reagents

Name	**Company/Location**
Cellfectin™ II Reagent	Thermo Fisher Scientific, Darmstadt
Fetal Bovine Serum (FBS)	Sigma-Aldrich, Taufkirchen
Gentamicin (50mg/ml)	Sigma-Aldrich, Taufkirchen
Sf-900 II SFM medium	Thermo Fisher Scientific, Darmstadt
Filtropur S 0.2	Sarstedt AG, Nümbrecht
Sterile syringes	B. Braun, Melsungen
Serological pipettes (5, 10, 25, and 50ml)	Sarstedt AG, Nümbrecht

7.3 Vectors

Vector	**Company/Location**
pFastBac™1	Thermo Fisher Scientific, Darmstadt
pFastBac™ Dual	Thermo Fisher Scientific, Darmstadt

pFBDM	Thermo Fisher Scientific, Darmstadt

7.4 Reagents kits and enzymes for molecular biology and biochemistry

Kit/Enzyme	**Company/Location**
Antarctic Phosphatase	New England Biolabs, Frankfurt a. Main
Bac-to-Bac® Baculovirus Expression System	Thermo Fisher Scientific, Darmstadt
Platinum™ *Pfx* DNA Polymerase	Thermo Fisher Scientific, Darmstadt
QIAprep® Miniprep Kit	Qiagen, Hilden
QIAquick® PCR Purification Kit	Qiagen, Hilden
Restriction enzymes	New England Biolabs, Frankfurt a. Main
SNAP-Surface® Alexa Fluor® 488 and 647	New England Biolabs, Frankfurt a. Main
T4 DNA Ligase kit	New England Biolabs, Frankfurt a. Main
HaloTag® Alexa Fluor® 660	Promega, Mannheim
Glucose Oxidase Type VII from *Aspergillus niger*	Sigma-Aldrich, Germany
Catalase from bovine liver	Sigma-Aldrich, Germany

7.5 Microorganisms

Cell strain	**Company/Location**
MAX Efficiency™ DH10Bac Competent Cells	Thermo Fisher Scientific, Darmstadt
XL1-Blue Subcloning-Grade Competent Cell	Stratagene, La Jolla (U.S.A.)

7.6 Software for data acquisition and analysis

Software	**Company/Location**
ImageJ Versions 1.44p and 1.50i	NIH, Bethesda (U.S.A.)
ImageJ plugin ParticleTracker 2D/3D	NIH, Bethesda (U.S.A.)
MATLAB R2016b	The MathWorks, Natick (U.S.A.)
OriginPro 9.1G 64-bit	OriginLab, Northampton (U.S.A.)
ASTRA 6	Wyatt Technology
NanoTemper Analysis software	NanoTemper Technologies, Munich

7.7 Size-exclusion chromatography columns

Column	Company/Location
TSKgel G4000SW$_{XL}$	Tosoh Biosciences, Griesheim
Superose 6 Increase 10/300 GL	GE Healthcare, Freiburg
Superdex 200 Increase 10/300 GL	GE Healthcare, Freiburg

7.8 Buffers and solutions

Buffer	Recipe
FLAG lysis buffer	50 mM PIPES, pH 6.9; 300 mM KAc, 1 mM $MgCl_2$, 1 mM DTT, 0.5% Triton X-100, 10% Glycerin, 0.1 mM ATP, cOmplete Protease Inhibitor tablet
FLAG wash buffer 1	80 mM PIPES, pH 6.9; 500 mM KAc, 1 mM $MgCl_2$, 1 mM DTT, 0.1% Tween-20, 10% Glycerin, 5 µM ATP, 1 mM EGTA
FLAG wash buffer 2	80 mM PIPES, pH 6.9; 200 mM KAc, 1 mM $MgCl_2$, 1 mM DTT, 0.1% Tween-20, 10% Glycerin, 0.1 mM ATP, 1 mM EGTA
FLAG elution buffer	FLAG wash buffer 2 + 0.5 mg/ml of 1x FLAG peptides
FLAG® Peptides (5 mg/ml)	5 mg FLAG® Peptide + 1ml TBS (1X)
TBS buffer (1X, pH 7.2)	20 mM Tris Base + 150 mM NaCl
Gel filtration buffer	25 mM PIPES, pH 7.0; 200 mM NaCl, 1 mM $MgCl_2$, 1 mM DTT, 1 mM EGTA
MST buffer	50 mM Tris- HCl, pH 7.6; 150 mM NaCl, 1 mM $MgCl_2$, 0.1% Tween 20, 10% Glycerin, 1 mM EGTA, 1 mM DTT
His lysis buffer	50 mM PIPES, pH 8.0; 300 mM KAc, 1 mM $MgCl_2$, 1 mM DTT, 0.5% Triton X-100, 10% Glycerin, 10 mM Imidazole, cOmplete Protease Inhibitor tablet
His wash buffer	50 mM PIPES, pH 8.0; 500 mM KAc, 1 mM $MgCl_2$, 1 mM DTT, 0.1% Tween-20, 10% Glycerin, 40 mM Imidazole,

	1mM EGTA
His elution buffer	50 mM PIPES, pH 7.5; 100 mM KAc, 1 mM $MgCl_2$, 1 mM DTT, 0.1% Tween-20, 10% Glycerin, 500 mM Imidazole, 1mM EGTA
TAE buffer (50X)	24.2% (w/v) Tris Base, 5.7% (v/v) Glacial acetic acid, 50 mM EDTA pH 7.0
DNA loading buffer	20% Glycerin, 0.1 M EDTA, 1% SDS, % 0.25 Bromophenol Blue
DNA elution buffer	10 mM Tris Base pH 8.0; 1 mM EDTA
S.O.C. medium	2% (w/v) Tryptone, 0.5% (w/v) Yeast extract, 10 mM NaCl, 2.5 mM KCl, 10 mM $MgCl_2$, 10 mM $MgSO_4$, 2% (v/v) 1 M Glucose
LB-Ampicillin agar	1.5% (w/v) Agar, 0.5% (w/v) Yeast extract, 1% (w/v) NaCl, 1% (w/v) Tryptone 0.1% (v/v) Ampicillin (100mg/ml)
LB-Ampicillin medium	0.5% (w/v) Yeast extract, 1% (w/v) Tryptone, 1% (w/v) NaCl, 0.1% (v/v) Ampicillin (100mg/ml)
Separating gel (10%, 10 ml)	3.3 ml Rotiphorese Gel 30, 2.5 ml separating gel buffer, 4.2 ml H_2O, 10 µl Temed, 100 µl APS
Separating gel buffer (10X)	0.5 M Tris Base pH 6.8; 0.4% (w/v) SDS
APS solution (100X)	10% (w/v) APS in H_2O
Stacking gel (10%, 10ml)	1.3 ml Rotiphorese Gel 30, 2.5 ml stacking gel buffer, 6.2 ml H_2O, 10 µl Temed, 100 µl APS
Stacking gel buffer (10X)	1.5 M Tris Base pH 8.8; 0.4% (w/v) SDS
Electrophoresis buffer (10X, pH 8.8)	3% (w/v) Tris Base, 1% (w/v) SDS, 14% (w/v) Glycine
SDS protein sample buffer (6X)	300 mM Tris Base pH 6.8; 15 mM EDTA , 12% (w/v) SDS, 30% (v/v) Glycerin, 0.06 % (v/v) Bromophenol Blue, 15% (v/v) β-Mercaptoethanol
Coomassie Brilliant Blue solution	10% (v/v) Glacial acetic acid, 50% (v/v) Methanol, 0.25% (w/v) Brilliant Blue R-250

Coomassie destaining solution	10% Glacial acetic acid, 25% Isopropyl alcohol
Buffer A	100 mM PIPES pH 6.8; 2 mM EGTA, 1 mM $MgSO_4$, 1mM DTT, 0.1 mM ATP
Buffer B	500 mM PIPES pH 6.8; 2 mM EGTA, 1 mM $MgSO_4$, 1mM DTT, 1 mM ATP
Buffer C	100 mM PIPES pH 6.8; 1 mM EGTA, 1 mM $MgSO_4$, 1mM DTT, 1 mM ATP
Buffer D	100 mM PIPES pH 6.8; 1 mM EGTA, 1 mM $MgSO_4$, 1mM DTT, 0.05 mM ATP, 0.022 mM GTP
BRB80 buffer (1X)	80 mM PIPES pH 6.9; 2 mM $MgCl_2$, 1 mM EGTA, 5mM DTT
BRB80/TX	BRB80 buffer (1X) + 5 µM Paclitaxel
Paclitaxel (4 mM in DMSO)	25 mg Paclitaxel + 7.3 ml DMSO
BRB80 motility buffer	BRB80 buffer (1X) + 10 mM ATP + 20% Glucose + 0.145 mg/ml Glucose Oxidase + 0.0485 mg/ml Catalase
Catalase solution (100X)	170000 U/ml Catalase in O_2 Quench buffer (1X), 50% (v/v) Glycerin
Glucose Oxidase solution (100X)	2600 U/ml Glucose Oxidase in O_2 Quench buffer (1X), 50% (v/v) Glycerin
Glucose solution (100X, 1 ml)	500 mg Glucose in 1 ml water
O_2 Quench buffer (1X)	24 mM PIPES, 4 mM $MgCl_2$, 4 mM EGTA
Assay Buffer AB (10X)	250 mM Imidazole, pH 7.4; 250 mM KCl, 40 mM $MgCl_2$, 100 mM DTT
Dephosphorylation buffer	60 UN of Antarctic Phosphatase, 10 mM DTT, 20 µl of AB(10X), 20 µl of AP buffer (10X) in a total volume of 200 µl H_2O
PBS (1X, pH 7.4)	140 mM NaCl, 2.7 mM KCl, 1.8 mM KH_2PO_4, 10 mM Na_2HPO_4
BBSA solution (10 ml)	10 mg BBSA in 10 ml PBS (1X)
Streptavidin solution (10 ml)	10 mg Streptavidin in 10 ml PBS (1X)
Blue-white agar	1.5% (w/v) Agar, 1% (w/v) Tryptone, 0.5% (w/v) Yeast extract, 1% (w/v) NaCl, 0.1

	mg/ml Bluo-gal, 0.04 mg/ml IPTG, 0.05 mg/ml Kanamycin, 7 µg/ml Gentamicin, 0.02 mg/ml Tetracycline
Blue-white medium	1% (w/v) Tryptone, 0.5% (w/v) Yeast extract, 1% (w/v) NaCl, 0.05 mg/ml Kanamycin, 7 µg/ml Gentamicin, 0.02 mg/ml Tetracycline
Tetracycline solution (100 ml)	50 mg Tetracycline in 100 ml H_2O
Kanamycin solution (100 ml)	50 mg Kanamycin Monosulfate in 100 ml H_2O
Gentamicin solution (100 ml)	50 mg Gentamicin in 100 ml H_2O
ATP solution (0.1 M pH 7.0)	100 mM Na_2ATP in H_2O
GTP solution (pH 7.0)	0.1 M GTP in H_2O
EDTA solution (pH 7.0)	200 mM EDTA in TAE buffer (50X)
EGTA solution (pH 7.0)	200 mM EGTA in TAE buffer (50X)

8 Methods

8.1 Cell culture

8.1.1 Cell culture of Sf9 insect cells

The Baculovirus Expression System (Thermo Fisher Scientific) was used to express all the recombinant proteins in the Sf9 insect cell line following the manufacturer's instructions. The original Sf9 cells were cloned from the parental *Spodoptera frugiperda* cell line IPLB-Sf-21-AE, which was originated from a population of cells of the pupal ovarian tissue *of Spodoptera frugiperda* [135, 136]. Sf9 cells were grown in Sf-900 II SFM medium supplement with 10% FBS and 0.5 mg/ml Gentamicin. The cell stock was kept at a cell density between 0.5 to 8×10^6 cells/ml. Cells were counted and diluted every other day with a fresh supplemented medium. For protein expression, Sf9 cells at a density of 2×10^6 cells/ml were infected with corresponding viruses, whereas cells concentration was brought down to a density of 0.5×10^6 cells/ml for virus amplification. The cell line was propagated up to 30 passages. Subsequently, a new cell stock was thawed and expanded according to the manufacturer's protocol (Thermo Fisher Scientific). DMSO-preserved cell aliquots were prepared and stored in liquid nitrogen as described by the manufacturer.

8.2 Molecular biology methods

8.2.1 DNA

All DNA constructs used in this study were commercially synthesized (GenScript Biotech, Piscataway, U.S.A.) by employing OptimumGene™ codon optimization technology to increase protein yields in insect cells. OptimumGene™ algorithm was used to alter bases in DNA sequence without changing amino acids sequence. DNA constructs were based on sequence information that is available on the WormBase website (http://www.wormbase.org) and cloned into the pFastBac1 vector according to the manufacturer's instructions (Thermo Fisher Scientific). In addition, the pFastBac1 vector was functionalized with Halo, SNAP, or GFP genes for C-terminal or N-terminal tagging of several constructs as described in this thesis. Four different OSM-3 constructs were designed for this study (see Supplementary information for details of DNA and protein sequences).

8.2.2 Separation of DNA fragments by agarose gel electrophoresis

DNA samples were mixed with 6X DNA loading buffer in a 1:6 ratio prior loading on 1% agarose gel. Electrophoresis was usually conducted at ~70 V for 45 minutes in 1X TAE buffer. A standard 1 kb DNA ladder was used to verify sizes of amplified DNA fragments. A UV light source was used to detect DNA bands.

8.2.3 Gel extraction of DNA fragments

Following electrophoresis, DNA bands of interest were excised from agarose gel with a clean and decontaminated scalpel. DNA bands were solubilized in buffer QG. DNA was gel-extracted using QIAquick® Gel extraction kit according to the manufacturer's protocol. Purified DNA was eluted in 30 µl of elution buffer.

8.2.4 Purification of DNA products and plasmids

DNA digestion products and amplified plasmids were purified from any excess of restriction enzymes and salt by using QIAquick® PCR Purification kit following the manufacturer's instructions. Purified samples were eluted in 30 µl of elution buffer. Samples were stored at -20ºC.

8.2.5 Determination of DNA concentration

Concentration of purified DNA samples was measured by NanoDrop® ND-1000 Spectrophotometer (Peqlab Biotechnologie GmBH) at 260 nm wavelength. Elution buffer was used as a blank.

8.2.6 Cloning techniques

Restriction enzyme-mediated DNA digest

Constructs used in this study were cloned using two different restriction sites fused at their 5' and 3' ends. Digestion with corresponding restriction enzymes was done according to the manufacturer's instructions. Double digestions were performed for 1 hour at 37ºC using a common buffer for both enzymes. Vector linearization was performed using 5 µg of DNA in 20 µl reaction volume.

Dephosphorylation of DNA vector

To prevent self-religation of already digested DNA vectors, a dephosphorylation step was performed. Linearized vectors were incubated with Antarctic Phosphatase and Antarctic Phosphatase buffer for 1 hour at 37ºC following the manufacturer's protocol. To quench the reaction, the mixture was incubated for 5 minutes at 70ºC.

Ligation of DNA inserts into linearized vectors

DNA inserts with their respective vectors were first mixed in a 1:5 ratio and then incubated overnight at 16ºC with T4 DNA Ligase enzyme in provided T4 DNA Ligase reaction buffer (10X).

Transformation of competent *E. coli* (XL1-Blue cells)

Ligation products were mixed with 200 µl of slowly thawed XL1-Blue cells and incubated on ice for 15 to 20 minutes. Cells were exposed to heat shock for 1 minute at 42ºC. Immediately after the heat shock, cells were placed back on ice for 5 minutes. 200 µl of S.O.C. medium was added to the mixture and incubated with shaking in a thermomixer at 37ºC and 850 rpm for 1 hour. Finally, cells were plated onto LB-Ampicillin Petri dishes and incubated overnight at 37ºC.

Screening, selection, and expansion of transformed *E. coli*

After overnight incubation, only cells that incorporated plasmid of interest were able to grow colonies since they contain the Ampicillin-resistance cassette (pFastBac1 and pFBDM). Eight colonies from each construct were picked. Each colony was inoculated in 2 ml of LB-Ampicillin medium for Mini-plasmid preparation (Mini-prep) and incubated overnight at 37ºC and 210 rpm in a shaker device.

Plasmid-DNA extraction from transformed bacteria

Overnight-grown cell cultures were pelleted by centrifugation for 10 to 15 minutes at 3,000 rpm. DNA was extracted from cell pellets using QIAprep® Miniprep Kit. Finally, DNA was eluted with 40 µl of pre-warmed elution buffer.

8.3 Protein biochemistry

8.3.1 Analytical methods

Protein analysis by SDS-polyacrylamide gel electrophoresis (SDS-PAGE)

10 or 12% polyacrylamide gels were used for protein separation. Protein samples were mixed with 6X SDS loading buffer and denatured at 95ºC for 5 minutes. Usually 20 to 35 µl of samples were loaded onto SDS gels with Mini-PROTEAN® 15-well or 10-well combs. A peqGOLD prestained Protein-Marker IV and unstained peqGOLD Protein-Marker II were used as a size control. Electrophoresis was performed at 50 mA with 240 V for ~50 minutes in 1X SDS separating gel buffer. Gels were stained with Coomassie Brilliant Blue solution for at least 2 hours under constant shaking. Afterwards, staining solution was exchanged with destaining solution. Destained gels were stored in H_2O and digitalized.

Determination of protein concentration

The concentration of the purified proteins was determined either by the NanoDrop® ND-1000 Spectrophotometer (Peqlab Biotechnologie GmBH) at 280 nm wavelength using elution buffer as a blank or by the ImageJ software. To this end, four different concentrations (0.1, 0.2, 0.3, and 0.4 ng/ml) of BSA were used to generate a calibration curve. Band intensities of digitalized SDS gels were measured using the ImageJ software [137]. The protein concentrations were calculated by measuring the respective band intensity and employing the BSA calibration curve. The absolute concentration was converted into a molar concentration using the following equation:

$$C_{molar}\ (Mol) = \frac{C_{absolute}\ (mg\ /\ ml)}{MW\ (kDa)}$$

8.3.2 Handling of tubulin protein

Isolation and purification of tubulin from porcine brain tissue

Porcine brains were freshly picked up from the slaughterhouse before each preparation, kept on ice, and brought back to the laboratory. Brain stems, veins, and meninges were removed off brains in a cold room. Around 700 to 800 g of brains were mixed with one volume of buffer A and homogenized in a waring blender. The homogenate was centrifuged at 4ºC and 13,000 rpm for 70 minutes. The supernatant was collected and gently mixed with 2 mM ATP and Glycerin (quarter of the final volume). To polymerize tubulins, the suspension was kept shaking at 35ºC for 30 minutes. The

polymerized MTs were pelleted by centrifugation at 42,000 rpm and 35ºC for 45 minutes. The pellets were resuspended in buffer C and homogenized on ice for 25 minutes to depolymerize the MTs. The homogenate was centrifuged for 30 minutes at 36,000 rpm and 4ºC. The supernatant was again collected and mixed with 2 mM ATP. For polymerization, the suspension was incubated for 30 minutes at 35ºC. MTs were sedimented by centrifugation for 40 minutes at 35ºC and 35,000 rpm. The pellets were collected, resuspended in buffer B, kept on ice, and occasionally homogenized for 25 minutes to depolymerize the MTs. The homogenate was centrifuged at 36,000 rpm and 4ºC for 25 minutes. The supernatant was mixed with 2 mM ATP and DMSO (one tenth of the final volume), and finally kept at 35ºC for 30 minutes, allowing the MTs to polymerize. The polymerized MTs were pelleted via centrifugation at 33,000 rpm and 35ºC for 40 minutes. The pellets were then resuspended in buffer D and homogenized on ice for 30 minutes to depolymerize the MTs filaments. Precipitates were removed by centrifugation at 34,000 rpm and 4ºC for 30 minutes. The supernatant was loaded onto a phosphocellulose (P-11) column to separate tubulin from microtubule associated proteins (MAPs). Tubulin was eluted from the column with buffer D. Fractions of interest were combined and mixed with 0.1 M GTP. The concentration of tubulin was calculated according to the law of Lambert-Beer. Tubulin aliquots were snap frozen in liquid nitrogen and stored at -80ºC.

$$\varepsilon_{\text{tubulin at 280 nm}} = 1.03\ \text{Mol}^{-1} \times \text{cm}^{-1} 1 \times 10^{3} \text{L} \rightarrow \text{with d} = 1\ \text{cm}$$

$$C_{\text{molar}}\,(\mu M) = \left(\frac{A_{280\text{nm}}}{\varepsilon_{\text{tubulin at 280nm}}}\right) \times 10 \times \text{dilution factor}$$

Tubulin polymerization

Typically, 50 µl of purified tubulin was mixed with 2 to 4 µl of biotinylated tubulin or 1 µl Atto488-labeled tubulin. The mixture was centrifuged for 10 minutes at 4ºC and 100,000 rpm. Afterwards, the supernatant was gently mixed with 1 mM of GTP and then incubated in a heat block at 35ºC for at least 1 hour to help formation of MTs filaments. To stabilize MTs filaments, 5 µM Paclitaxel was added after the incubation time. Polymerized MTs were kept in a heat block at 35ºC. Before conducting microscopy assays, MTs were diluted in BRB80/TX buffer and stored back at 35ºC.

8.3.3 Protein production using the baculovirus-insect cell expression system

In this study, we opted for the baculovirus-insect cell (Sf9) system for protein expression. This system offers many advantages, which exist in higher eukaryotic systems such as mammalian systems and do not exist in other traditional systems (e.g., the bacterial expression system). For example, post-translational modifications and proper protein folding. Proteins produced in this

system adopt native and folded confirmation with proper post-translational modifications that are essential for proper functionality displayed by these proteins, in particular motor proteins (e.g., OSM-3). Furthermore, the baculovirus system combines biological safety with high expression levels of mostly soluble-produced proteins.

Generation and isolation of recombinant bacmids

Genes of interest were cloned into a donor plasmid either pFastBac™1 or pFBDM, which is derived from pFastBac™ Dual. pFBDM possesses a central multiplication module flanked by two multiple cloning sites (MCS1 and MCS2) driven by polyhedrin (polH) and p10 promoters, allowing for a simultaneous expression of two different proteins in the same plasmid. In contrast to pFBDM, pFastBac™1 possesses only a polH promoter. Donor plasmids were transformed into *E. coli* MAX Efficiency™ DH10Bac Competent Cells to produce the baculovirus shuttle vector (bacmid). DH10Bac cells contain a helper plasmid that encodes a transposase and confers resistance to tetracycline. The mini-Tn7 element from the pFastBac™ donor plasmid is site specifically transposed to the mini-attTn7 site in the bacmid, which allows introducing the gene of interest into the viral genome and disrupting the lacZα region. Cells with successfully transposed bacmids are white, whereas the non-transposed cells are growing blue on blue-white selection agar Petri dishes.

Around 500 ng of the recombinant donor plasmid was gently mixed with slowly thawed DH10Bac competent cells. The mixture was kept on ice for 15 to 20 minutes followed by a heat shock for 1 minute at 42ºC and then the cells were again kept on ice for another 5 minutes. 800 µl of S.O.C. medium was added to the cell suspension and left to grow at 37ºC for 5 hours with shaking at 210 rpm. 50 and 100 µl of the cell suspension were streaked on a freshly prepared blue-white plates and incubated for 3 days at 37ºC. White colonies were picked and restreaked on a new blue-white plates, and left to grow overnight to confirm choosing the right colonies. Subsequently, four large white colonies were picked, and each colony was mixed with 6 ml of blue-white medium. Colonies were left to grow overnight in a shaker at 37ºC and 210 rpm. Cells were pelleted by centrifugation for 15 minutes at 3,000 rpm, and DNA was isolated using QIAprep® Spin Miniprep Kit following the manufacturer's protocol. Isolated DNA was solved in 100 µl of sterile H_2O.

Transfection of Sf9 cells with recombinant bacmid

2 ml of Sf9 cells at a density of 0.5×10^6 cells/ml were seeded into a 6-well plate and incubated at 28ºC. Isolated bacmid DNA (15 to 25 µl) was mixed with 10 µl of Cellfectin™ II Reagent and 200 µl of Sf-900 II SFM medium (FBS and Gentamicin free), and incubated at room temperature for 30 minutes, allowing lipids to cover DNA for better transfection of Sf9 cells. Seeded cells were washed

two times with Sf-900 II SFM medium (FBS and Gentamicin free). 800 µl of Sf-900 II SFM medium (FBS and Gentamicin free) was added to the DNA-Cellfectin mixture and then the total mixture was applied onto seeded Sf9 cells. Cells were incubated for 5 hours at 28ºC. Following the incubation time, the DNA-Cellfectin mixture was exchanged with 2 ml of Sf-900 II SFM medium (supplement with 10% FBS and 1% of 50 mg/ml Gentamicin). Cells were incubated for 4 to 5 days at 28ºC. First virus generation (P_0) was harvested with a sterile 2 ml syringe and 0.22 µm Filtropur S. P_0 virus was stored at 4ºC for further use.

Virus amplification of P_0 generation

Due to low volume yields (~2 ml) of P_0 virus, a second baculovirus generation (P_1) was amplified from P_0 virus. To this end, 1 ml of P_0 virus was added to 30 ml of Sf9 cells at a density of 0.5×10^6 cells/ml. A negative control containing 30 ml of 0.5×10^6 cells/ml of Sf9 cells was prepared for later comparison. Cells were incubated for at least 7 days at 28ºC. After successful transfection, cells were harvested by centrifuging for 20 minutes at 3,500 rpm. The supernatant containing P_1 virus particles was transferred into a new sterile 50 ml falcon tube. P_1 virus was used for amplification of a third virus generation (P_2) following the same previous steps. P_2 virus was used in all experiments in this study. P_1 and P_2 viruses were stored at 4ºC.

Protein expression in Sf9 cells

For a small scale infection, 50 to 200 ml of Sf9 cells at a density of 2×10^6 cells/ml were prepared from the cell stock, whereas 1 to 2 liters of cells were used for a large scale infection. Sf9 cells were subsequently infected with 4 to 6% of P_2 virus (v/v). For efficient infection, cells were grown for 65 to 72 hours at 28ºC with shaking at 110 rpm. Cells were then harvested by centrifugation for 15 minutes at 1,500 rpm. Cell pellets were either used for immediate protein purification or stored at -20ºC for later use.

8.3.4 Affinity protein purification

Affinity purification is used to capture proteins of interest from a pool of complex mixture of cell lysate. Therefore, proteins used in this study were fused either with FLAG or 6XHis-tag at their C- or N-termini for affinity purification.

FLAG-tag affinity purification

Cell pellets were lysed in FLAG lysis buffer. Cell lysate was centrifuged for 10 minutes at 30,000 rpm and 4ºC. The supernatant containing proteins of interest was incubated with 0.1% (v/v) of ANTI-FLAG® M2 Affinity Gel for 90 minutes with rotation at 4ºC. The suspension was centrifuged for 15

minutes at 700 rpm and 4ºC. The supernatant was either discarded or subjected to His-tag affinity purification (see the following section), whereas the pelleted FLAG-resin was transferred into a new 1.5 ml Eppendorf tube. To get rid of non-specific bound proteins, FLAG-resin was washed three times with 1 ml of FLAG wash buffer 1 followed by three times with 1 ml of FLAG wash buffer 2. Proteins were eluted with FLAG elution buffer for 1 hour at 4ºC with rotation. Only in case of motility assays, ATP was added to all FLAG buffers. For SEC-MALS and MST experiments, proteins were eluted twice, and each time for 45 minutes. Eluted proteins were either used fresh or aliquoted, snap frozen in liquid nitrogen, and stored at -80ºC. It is highly recommended that freshly purified proteins should be used in SEC-MALS experiments and functional transport TIRF assays.

His-tag affinity purification

Harvested cell pellets were lysed in His lysis buffer. Cell debris was pelleted by centrifugation for 10 minutes at 30,000 rpm and 4ºC. Supernatant containing target proteins was incubated with 0.5% (v/v) of washed Ni-NTA agarose beads for 90 minutes at 4ºC in a rotator. Agarose beads were collected by centrifugation for 15 minutes at 700 rpm and 4ºC. Supernatant was discarded and agarose beads were transferred into a new 1.5 ml Eppendorf tube. Agarose beads were washed six times with 1 ml of His wash buffer to remove nonspecific bound proteins. Proteins were eluted with His elution buffer for 1 hour at 4ºC with rotation. Eluted proteins were either used fresh for SDS-PAGE analysis or aliquoted, snap frozen in liquid nitrogen, and stored at -80ºC.

8.3.5 Phosphorylation and dephosphorylation of IFT-B subunits

In case of phosphorylation, the purified proteins were mixed with the protein kinases (DYF-5 and/or DYF-18). Around 0.25 mM ATP was added to the mixture and incubated for 45 minutes in a heat block at 30ºC. For dephosphorylation, the FLAG elution buffer of the purified proteins was exchanged with the dephosphorylation buffer by using Amicon® Ultra 0.5 mL Centrifugal Filters Ultracel® -10 K (Merck Millipore, Darmstadt, Germany). The proteins were incubated for 45 minutes in a heat block at 30ºC and then were loaded into a new Amicon® Ultra 0.5 mL tube. They were subsequently washed three times with FLAG elution buffer to remove remnants of the phosphatase enzyme and buffer. Finally, the proteins were eluted back in FLAG elution buffer.

8.3.6 In vitro phosphorylation assay with the isotope-labeled ATP (Kinase assay)

Kinase assays were conducted as described previously [138]. ATP [ɣ-32P] was used to identify IFT-B phosphorylation targets of protein kinases (i.e., DYF-5 and DYF-18). To this end, an equivolume of the recombinantly expressed protein kinase (DYF-5 or DYF-18) was mixed with an equimolar

concentration of the purified IFT-B proteins. An ATP master mix was prepared (0.1 µl of 1 µM ATP [ɣ-32P] and 3 µl of 0.01 mM cold ATP) and added to the protein mixtures, and the total volume of each reaction was kept constant at 30 µl. The mixtures were then incubated in a thermomixer (Eppendorf, Germany) for 25 to 30 minutes at 30ºC. To quench the reactions, a 10 µl of 6X SDS buffer was added to the mixtures and the reactions were cooked for 5 minutes at 95ºC. 15 to 25 µl from each reaction were loaded onto a 10% or 12% SDS gel and electrophoresis was conducted for 1 hour at 300 V and 35 mA. The gel was trimmed, wrapped with a plastic cling, and exposed overnight to a phosphor storage screen. The screen was scanned with a phosphorimager (Typhoon 9200, Molecular Dynamics) and digital images were used for analysis.

8.3.7 SEC-MALS

MALS is a multiple fixed angles system that is used as a part of SEC setup to gauge molar masses of molecules such as polymers and proteins. The number of angels (photodetectors) in MALS varies between 2 up to 20, our MALS system contains only 8 angles. In MALS, a laser source producing a collimated beam of monochromatic light is used to illuminate a flow cell containing the sample to be analyzed (Figure 40). The scattering intensity produced by the sample is measured simultaneously at each angel in dependence of the scattering angle (θ), which is called scattering curve $I_{\text{scattered}}(\theta)$. This gives information about the size, shape, and molar mass of the scattering particle. The intensity of scattered light depends on the polarizability of the solute. The polarizability is expressed by the change in the refractive index (RI) of the solution (Δn) with the change in molecular concentration (Δc). This parameter is called the specific RI increment dn/dc. The amount of scattered light is directly proportional to the molar mass (M_w) and concertation of the protein (C).

$$I_{\text{scattered}}(\theta) \propto M_W C \left(\frac{dn}{dc}\right)^2$$

If the specific refractive index increment (dn/dc) and concentration of the protein are known, the measured light scattering directly determines the molar mass. Since the angular dependence of the scattering depends only on the rms radius of the molecule, the rms radius can be determined without knowing the concentration or the dn/dc value of the molecule.

The mathematical relationship describing the angular variation of the scattered intensity as a function of particle size, i.e., the Form Factor $P(\theta)$, depends on the size of the particle, the wavelength of the light l, and the observation angle θ. Therefore, size information can be retrieved from the angular dependence of the scattering intensity alone. No information of the concentration or dn/dc of the solute is necessary to determine the size.

$$I_{\text{scattered}}(\theta) \propto M_W C \left(\frac{dn}{dc}\right)^2 P(\theta)$$

Note that the equations included in this part are quoted from Wyatt company seminars, the company from which we have purchased our MALS devices.

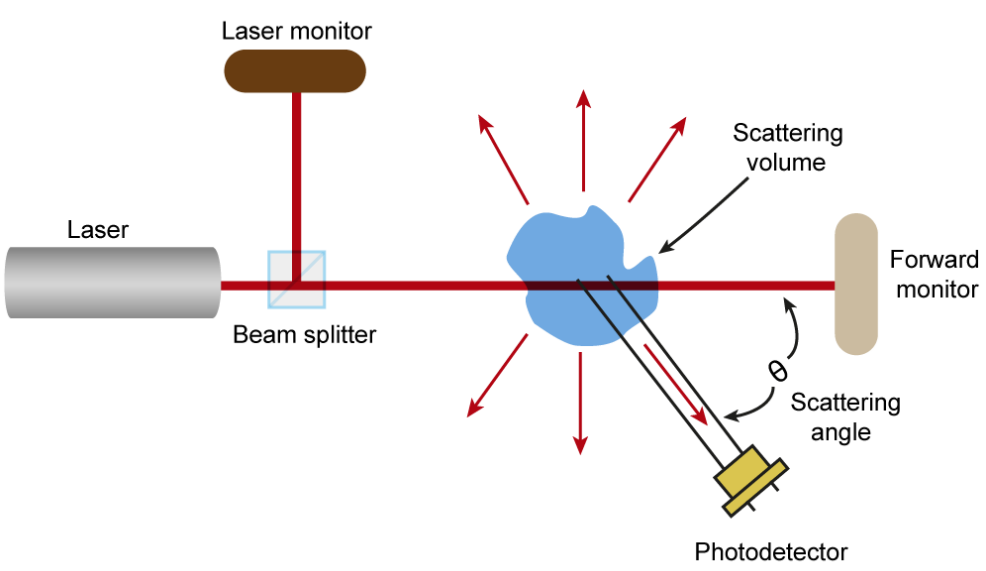

Figure 40: Schematic of the of MALS apparatus for measurement of static light scattering. The laser intensity is determined by the laser monitor before the beam enters the flow cell. The laser beam then propagates through the flow cell bore. The scattered light detected in the horizontal plane propagates through the flow cell glass to the photodetectors. The remaining light that is unscattered reaches the forward monitor. The forward monitor reading is only used for diagnostic purposes or in the case of samples that absorb at the laser wavelength. This figure is adapted from Wyatt seminars that I have attended.

In this study, three different gel filtration columns (TSKgel G4000SW$_{XL}$, Superose 6 Increase 10/300 GL, and Superdex 200 Increase 10/300 GL) were used to purify the corresponding protein complexes. The columns were inline with a Quaternary Pump (Agilent 1260 Infinity series), a Variable Wavelength Detector (Agilent 1260 Infinity series), a DAWN8+ MALS detector (Wyatt Technology), and an Analytical-Scale Fraction Collector (Agilent 1260 Infinity series). Before each measurement, the columns were calibrated with at least two column volume of the gel filtration buffer. Note that all the purification buffers were supplemented with 10% Glycerin and 0.1% Tween-20 to stabilize already-formed protein complexes and prevent aggregates formation during the concentration step, respectively. Purified proteins from a large scale infection (1 to 2 liters of infected

Sf9 cells) were concentrated using Amicon® Ultra 0.5 mL Centrifugal Filters Ultracel® -10 K (Merck Millipore) and exposed to hard spin for 10 minutes at 80,000 rpm and 4ºC to get rid of any beads leftover from the purification step. 100 to 150 µl of concentrated proteins were collected, transferred into a new 2 ml Eppendorf tube, and manually injected into the sample loop of the HPLC system using a 1 ml sterile syringe. Protein samples were either separated at a flow rate of 0.2 or 0.3 ml/min. Fractions of interest were collected, run on a SDS gel, and eventually stored at -80ºC. In case of lower yields, fractions were collected and then concentrated before running a SDS gel using the same Amicon® Ultra 0.5 mL tubes. Molar masses were calculated with ASTRA 6 software with the d*n*/d*c* value set to 0.185 ml/g. BSA was used as a calibration standard. All the raw data were extracted from ASTRA 6 software and the elution profiles were plotted using OriginPro 9 software.

8.3.8 MST binding assays

MST is a tool used to monitor direct movements of fluorescent molecules through a temperature gradient, allowing for precise analysis of binding molecules in µl volumes independent of size and physical properties [111]. A temperature difference ΔT in space results in a depletion of molecules in the region of elevated temperature, which can be quantified by the Soret coefficient S_T with the C_{hot} and C_{cold} representing the concentration in the heated and non-heated regions inside the measuring capillary, respectively [111]:

$$C_{hot}/C_{cold} = e^{-S_T \Delta T}$$

To determine K_d values of a certain complex in MST, a non-fluorescent ligand is titrated against a fixed amount of a fluorescent binding partner. The thermophoretic movement of the fluorescent molecule changes upon binding to the non-fluorescent ligand resulting in a different traces, which can be expressed as the changes in the normalized fluorescence [111]:

$$\Delta F_{norm} = F_{hot}/F_{cold} .1000$$

Plotting the values of ΔF_{norm} against the ligand concentration eventually results in a binding isotherm, which yields the K_d value of the interaction [111]. In our MST, the fluorophore-labeled OSM-3(G444E)-Halo at 10 nM was titrated with the respective unlabeled protein complexes, the concentration of which varied between 0.2 nM and 2 µM. 15 such serially diluted titrations of the unlabeled proteins were prepared to generate one full binding curve. The reactions were incubated overnight in the dark at 4ºC. Samples were loaded into standard coated capillaries (NanoTemper

Technologies) and mounted in Monolith NT.115 system (NanoTemper Technologies). All the experiments were performed using LED at 60% excitation power (red filter, excitation 605-645 nm, emission 680-685 nm) and IR-laser power at 20%. K_d values were determined using NTAffinity Analysis software (NanoTemper Technologies), in which the binding curves were derived from the raw fluorescence data. The raw data were extracted from the NanoTemper Analysis software and plotted using OriginPro 9 software.

8.3.9 Fluorescent labeling of proteins

Proteins of interest were either C- or N-terminally functionalized with a SNAP or Halo tags. The SNAP-tag is derived from O^6-alkylguanine-DNA-alkyltransferase and reacts with benzylguanines (BGs) and benzylchloropyrimidines derivatives, whereas the HaloTag is a modified haloalkane dehalogenase designed to react irreversibly with primary alkylhalides [139, 140]. These two tags bind specifically and covalently to their synthetic ligands. This labeling strategy is widely applicable for microscopy imaging. Fluorescent labeling of proteins was conducted prior to the elution step. Protein-coated beads were suspended in 150 µl of FLAG wash buffer 2 containing either 1 mM HaloTag® Alexa Fluor® 660 ligand (for labeling OSM-3(G444E)^{Halo} motor) or 1 mM SNAP-Surface® Alexa Fluor® 488 or 647 (for labeling OSM-3^{SNAP} motor and the corresponding IFT-B subunits) and incubated for 30 minutes at room temperature in the dark with rotation. The beads were subsequently washed three times with 1 ml of FLAG wash buffer 2 to remove excess dye. Proteins were then eluted as mentioned before. While OSM-3(G444E)^{Halo} and OSM-3^{SNAP} labeled proteins were used fresh right after the elution step for functional assays, other fluorescently labeled proteins were aliquoted, snap frozen, and stored at -80ºC.

8.4 TIRF microscopy assays

8.4.1 Photobleaching assay

SNAP and GFP functionalized IFT-B subunits used in single-molecule assays were initially subjected to bleaching step analysis in order to verify that the transport parameters were obtained from non-aggregated, single subunits. To this end, the proteins were diluted in BRB80 buffer (1X), mounted on a glass slide, and fluorescence was observed in TIRF illumination. Spots for analysis were chosen for all proteins by intensity over the mean intensity, and the intensity values for a 3×3 pixel window were summarized. Bleaching curves were extracted from observation of the spot intensities over time. Performing a gliding *t*-value test with a corresponding threshold identified the bleaching steps.

8.4.2 Colocalization assay

The pairwise colocalization experiments for the functionalized proteins were performed as follows: the corresponding proteins were purified and labeled with two different fluorophores (see section 8.3.4 and 8.3.9). The labeled proteins were run onto a SDS-PAGE gel, and their concentrations were determined (section 8.3.1) and adjusted accordingly. Equimolar concentrations of the labeled proteins were mixed together and incubated overnight with rotation at 4ºC. In the following day, protein mixtures were diluted in 1X BRB80 buffer and flowed into a flow chamber. Excitation was carried out at 488 and 638 nm wavelength and fluorescence signals from the two channels were detected using TIRF illumination. The colocalized images were analyzed using custom-written routines in MATLAB software (MathWorks). Raw data points were extracted from MATLAB software and plotted using OriginPro 9 software. The colocalized images were further processed in ImageJ software.

8.4.3 Functional transport TIRF assay

Purified proteins were mixed with the corresponding motor protein in an equimolar concentration and incubated overnight at 4ºC on a rotator. Flow chambers (coated with 1 mg/ml BBSA and 1 mg/ml streptavidin) were prepared with biotinylated-microtubules attached to their surfaces. To track the motor movement alone or in the presence of IFT-B proteins, the protein complexes were diluted to the desired concentrations in BRB80 motility buffer and flowed into the chamber. Movements of the fluorescent signals were recorded with a cycle time of 235 ms with an objective-type Leica DMI6000 B TIRF microscope (Leica, Germany), equipped with an oil-immersion 100× Plan objective lens (numerical aperture (NA) 1.47), and a back-illuminated Andor U897 EMCCD camera (Andor, UK). Excitation was carried with the help of diode lasers at 488 and 635 nm wavelength, and frames were recorded and analyzed with AF 6000 software (Leica, Germany). Acquired movies were further processed using ImageJ software. Velocities and run lengths were analyzed with custom-written programs using MATLAB software (Mathworks). Spots were selected automatically according to their brightness compared to the mean brightness in each frame. The position of the spots was determined with subpixel accuracy using a radial centre approach. From each frame a list of spots was created and the distance of a spot in each subsequent frame was compared. A tracking trace was generated by connecting each spot to the closet one in the next frame with a cut-off maximal distance. The distance to the first position of each spot over time was fitted with a linear model. A threshold of 1 µm was applied to run length measurements to be considered processive (χ_0 = 1 µm). Parts of the distance-over-time data were considered for speed calculation in a linear fit of at

least six frames that resulted in a $r^2 > 95\%$. Histograms of velocities were fitted to a Gaussian distribution, whereas run lengths were fitted to a single exponential ± confidence. Landing events were counted from the data obtained using the tracking algorithm described above. Events that started after the first frame and showed a displacement from the binding position of at least 2 µm while associated with the microtubule were counted (*n*).

As no processive movement was observed for the OSM-3^{SNAP}, runs were not selected for unidirectionality. Images of the MTs positions were obtained from maximum intensity projections of the single molecule movies and their length (*l*) were measured using ImageJ. Considering the total length of a movie (t), the landing rate for a movie was calculated as $e = n/l/t$. This value was then corrected for the relative dilution (*c*) of the motor over the motor plus adaptor ($e_{corr} = e/c$). The mean of this value over three independent purifications was calculated alongside the s.d. and reported. In order to assign colocalized movements, runs were compared pairwise from the two channels. Weighted penalties resulted from the mean distances of tracked positions (pixel, factor 1/3) and the difference of the starting time (frames, factor 1). Runs with a penalty below ten were considered, and parameters are averages of single runs. Statistical significance between datasets was determined by a two-sample *t*-test performed in *R*. Random resampling of the data by boot-strapping ($R = 1{,}000$) resulted in *P* values for comparison of the means. The *P* values for single population speed distributions were calculated in MATLAB using the ttest2 function. *P* values of < 0.01 were considered significant.

8.4.4 Microtubules decoration assay

Biotinylated, Atto488-labeled microtubule filaments were polymerized as described previously (see section 8.3.2). 10µl of BBSA solution with a concentration of 1 mg/ml was flushed into a flow chamber and incubated for three minutes. The glass surface of the flow chamber was blocked with 10 mg/ml of BSA in BRB80 buffer (1X). Afterwards, the streptavidin solution (1 mg/ml) was flowed into the chamber and incubated for another three minutes to bind to BBSA. This followed by a washing step with 10 mg/ml of BSA in BRB80 buffer (1X) to remove the excess of streptavidin. The polymerized microtubules were attached to the BBSA-Streptavidin layer, and the unbound filaments were washed off with 10 mg/ml of BSA in BRB80 buffer (1X). The corresponding Alexa Fluor 647-labeled IFT-B proteins were diluted in BRB80 motility buffer that lacks ATP and then flowed into the flow chamber. Images of the flow chamber were acquired at room temperature using TIRF microscope. The acquired images were further processed using ImageJ software.

9 Appendix

9.1 Abbreviations

IFT	Intraflagellar transport
IFT-A	Intraflagellar transport-A
IFT-B	Intraflagellar transport-B
C. elegans	*Caenorhabditis elegans*
C. reinhardtii	*Chlamydomonas reinhardtii*
OSM-3	Osmotic avoidance abnormal protein 3
QCC	Quadripartite core complex
TCC	Tripartite core complex
MST	Microscale thermophoresis
SEC	Size exclusion chromatography
MALS	Multi-angel light scattering
HPLC	High-performance liquid chromatography
TIRF	Total internal reflection fluorescence
kDa	Kilodalton
GFP	Green fluorescent protein
S.D.	Standard deviation
PAGE	Polyacryl amide gel electrophoresis
SDS	Sodium dodecyl sulfate
MTs	Microtubules
S.O.C.	Super optimal catabolite
DTT	Dithiothreitol
BSA	Bovine serum albumin
BBSA	Biotinylated bovine serum albumin
C-terminus	Carboxy terminus
N-terminus	Amino terminus
EGTA	Ethylene-bis(oxyethylenenitrilo)tetraacetic acid
EDTA	Ethylenediaminetetraacetic acid
FBS	Fetal bovine serum
GTP	Guanosine 5’-triphosphate

ATP	Adenosine-5'-triphosphate
rpm	Rounds per minute
PIPES	Piperazine-1,4-bis(2-ethanesulfonic acid)
TEMED	N,N,N′,N′-Tetramethylethylenediamine
LC-MS/MS	Liquid chromatography tandem mass spectrometry
LB	Luria broth
Bluo-Gal	Halogenated indolyl-β-galactosidase
DMSO	Dimethyl sulfoxide
IPTG	Isopropyl β-D-1-thiogalactopyranoside
MAPS	Microtubule-associated proteins
TAE	Tris-acetate-EDTA
Tris Base	Tris (hydroxylmethyl) aminomethan
KAc	Potassium acetate
$MgCl_2$	Magnesium chloride
AB	Assay buffer
AP	Antarctic phosphatase
PBS	Phosphate buffer saline

9.2 Supplementary information

9.2.1 SEC-MALS analysis OSM-3(G444E)^{Halo} motor

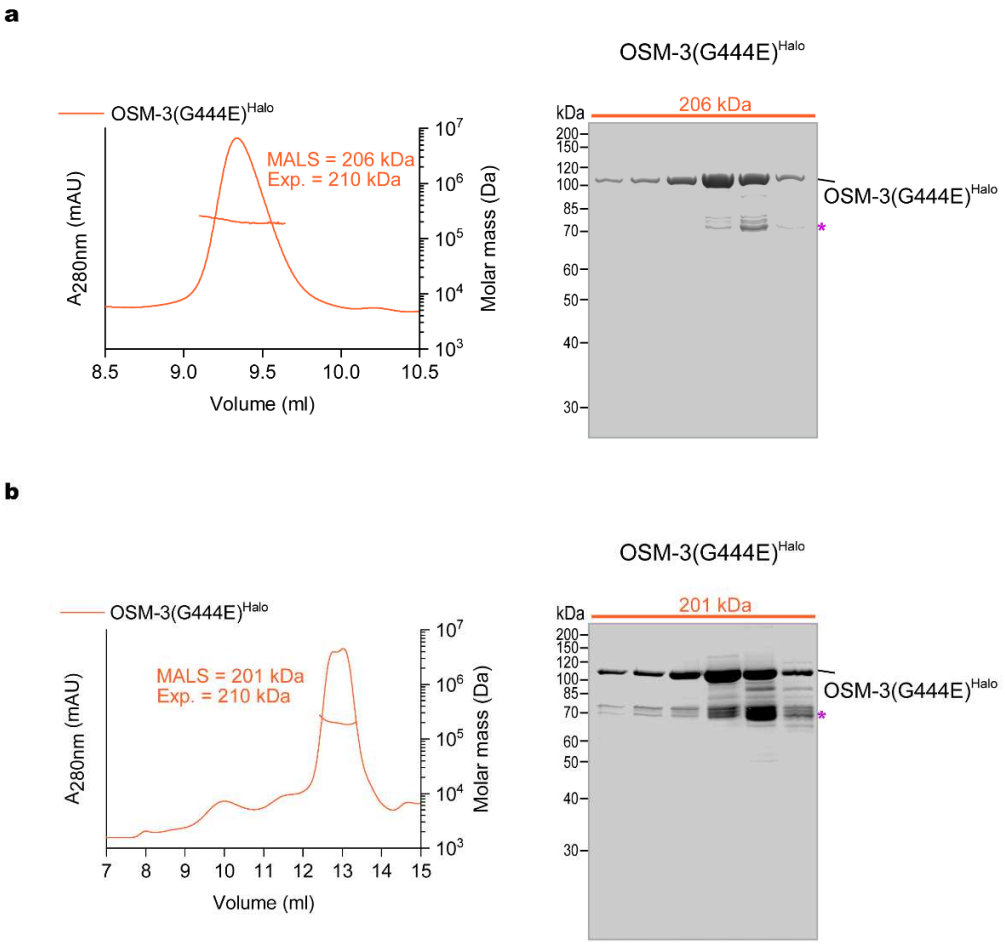

Supplementary figure 1: SEC-MALS analysis of the OSM-3(G444E)^{Halo} motor. **(a)** The SEC-MALS and the SDS gel analyses of the OSM-3(G444E)^{Halo} motor (left and right, respectively) after gel filtration using the TSKgel G4000SW$_{XL}$ column. **(b)** The SEC-MALS profile (left) and the Coomassie-stained SDS-PAGE gel (right) of peak fractions of the OSM-3(G444E)^{Halo} motor after purification using the Superose 6 Increase 10/300 GL column.

9.2.2 SEC-MALS analysis of CHE-2 (IFT-80) subunit

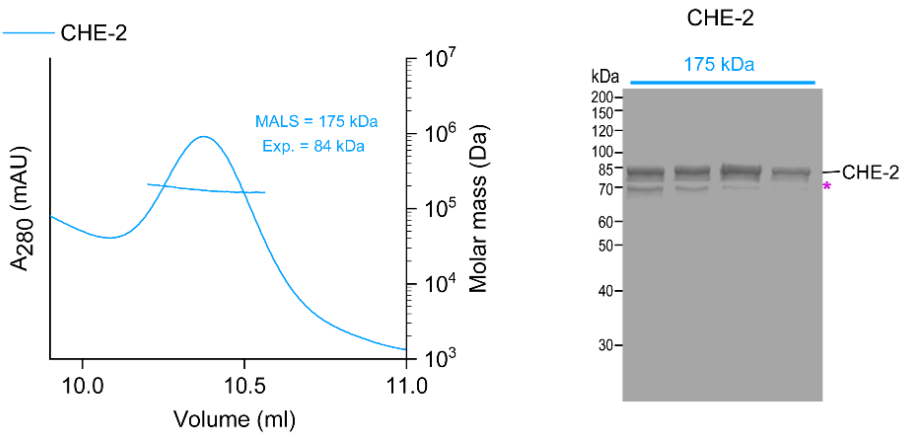

Supplementary figure 2: Homodimerization behavior of the CHE-2 subunit. The SEC-MALS profile (left) along with the SDS-PAGE gel (right) of MALS fractions of CHE-2 subunit show that the CHE-2 subunit form a homodimer judged from the MALS fit displaying a molar mass of 175 kDa compared to 84 kDa the expected molar mass theoretically calculated from the protein sequence. Gel filtration was conducted using the Superdex 200 Increase 10/300 GL column. Asterisk indicates the HSP70 protein band.

9.2.3 Supplementary table 1: A comprehensive list of IFT components

IFT component	*C. reinhardtii*	*C. elegans*	*Homo sapiens*	Protein size (kDa)
IFT-A complex	IFT-144	DYF-2	WDR19	155
	IFT-140	CHE-11	IFT-140	162
	IFT-139	ZK328.7	TTC21B	151
	IFT-122	DAF-10	IFT-122	136
	IFT-121	IFTA-1	WDR35	141
	IFT-43	IFT-43	IFT-43	28
IFT-B complex	IFT-52	OSM-6	IFT-52	55
	IFT-88	OSM-5	IFT-88	92
	IFT-70	DYF-1	TTC30A/TTC30B	73
	IFT-46	DYF-6	IFT-46	55
	IFT-74	IFT-74	IFT-74	73
	IFT-81	IFT-81	IFT-81	70
	IFT-22	IFTA-2	RABL5	29
	IFT-27	-	IFT-27/RABL4	22
	IFT-25	-	IFT-25	20
	IFT-172	OSM-1	IFT-172	190
	IFT-80	CHE-2	IFT-80	84
	IFT-57	CHE-13	IFT-57/HIPPI	47
	IFT-54	DYF-11	TRAF3IP1/MIPT3	58
	IFT-20	Y110A7A.20	IFT-20	16
	IFT-56	DYF-13	TTC26	66
	IFT-38/FAP22	DYF-3	CLUAP1	44
Homodimeric Kinesin-2	-	OSM-3	KIF-17	75
Heterotrimeric Kinesin-2 (kinesin-II)	FLA-10	KLP-20	KIF3A	73
	FLA-8	KLP-11	KIF3B	88
	FLA-3	KAP-1	KAP3/KIFAP3	78
Dynein-2	DHC1b	CHE-3	DYNC2H1	473
	FAP133	DYCI-1	WDR34	72
	D1BLIC	XBX-1	DYNC2LI1	42
	LC8/FLA14	DLC-1	DYNLL1	10
BBSome complex	BBS-1	BBS-1	BBS1	65
	-	BBS-2	BBS2	81
	BBS-3/ARL6	BBS-3/ARL6	BBS3/ARL6	21
	BBS-4	BBS-4	BBS4	51
	BBS-5	BBS-5	BBS5	41
	BBS-7	BBS-7	BBS7	80
	BBS-8	BBS-8	BBS8	56
	BBS-9	BBS-9	BBS9	83
	-	-	BBS18/BBIP10	10

9.2.4 Supplementary videos

The supplementary videos and their corresponding legends are freely available on the following publication link:

Mohamed, M.A.A., W.L. Stepp, and Z. Ökten, Reconstitution reveals motor activation for intraflagellar transport. *Nature*, 2018. **557**(7705): p. 387-391.

https://www.nature.com/articles/s41586-018-0105-3#MOESM4

9.3 DNA and protein sequences of the OSM-3 constructs used in the study

9.3.1 OSM-3(G444E)^{Halo} (OSM-3 sequence with the G444E mutation C-terminally tagged with Halo and Flag)

Cloning sites into the pFastBac1 vector: SpeI and Not I

ACTAGTATGGCAGAAAGCGTTAGAGTGGCAGTTAGATGTAGACCGTTCAACCAGAGAGAAAA
AGACCTCAACACAACCCTGTGCGTGGGCATGACCCCAAACGTGGGCCAGGTCAACCTGAAC
GCTCCTGACGGAGCTGCCAAGGACTTCACCTTCGACGGAGCCTACTTCATGGACTCCACTGG
TGAACAGATCTACAACGACATCGTGTTCCCACTGGTGGAAAACGTCATCGAGGGATACAACG
GTACCGTCTTCGCTTACGGACAGACCGGCTCAGGAAAGACTTTCTCCATGCAGGGTATCGAG
ACTATCCCAGCTCAGAGGGGCGTGATCCCTAGAGCCTTCGACCACATCTTCACCGCCACTGC
TACCACTGAAAACGTGAAGTTCCTGGTCCACTGCTCCTACCTGGAGATCTACAACGAGGAAG
TCAGGGACCTGCTGGGTGCCGACAACAAGCAGAAGCTGGAAATCAAGGAGCAGCCAGACAG
AGGAGTGTACGTCGCTGGTCTGAGCATGCACGTGTGCCACGACGTCCCTGCCTGCAAGGAG
CTGATGACCCGCGGTTTCAACAACCGTCACGTGGGCGCTACTCTGATGAACAAGGACTCCAG
CCGCTCTCACTCAATCTTCACCGTGTACGTCGAAGGCATGACCGAGACTGGAAGCATCCGTA
TGGGCAAGCTGAACCTCGTGGACCTGGCTGGATCTGAAAGGCAGTCTAAGACCGGCGCTAC
TGGTGACCGCCTGAAGGAGGCCACCAAGATCAACCTGTCCCTGAGCGCTCTGGGAAACGTG
ATCAGCGCCCTGGTCGACGGCAAGTCTAAGCACATCCCTTACCGCGACTCAAAGCTGACTCG
TCTGCTGCAGGACTCCCTGGGTGGCAACACCAAGACTATCATGATCGCTTGCGTGTCACCCT
CTTCAGACAACTACGACGAAACCCTGTCCACTCTGCGCTACGCCAACCGTGCTAAGAACATC
AAGAACAAGCCCACCATCAACGAAGACCCAAAGGACGCTCTGCTGAGGGAGTACCAGGAGG
AAATCGCCAGACTGAAGAGCATGGTGCAACCTGGTGCTGTGGGTGTGGGCGCCCCAGCTCA
GGACGCTTTCTCTATCGAGGAAGAGAGGAAGAAGCTGAGAGAAGAGTTCGAAGAGGCTATGA
ACGACCTGAGGGGCGAATACGAGAGAGAACAGACTAGCAAGGCTGAACTGCAGAAGGACCT
GGAGTCTCTGCGCGCCGACTACGAGCGTGCCAACGCTAACCTGGACAACCTGAACCCCGAA
GAGGCTGCCAAGAAGATCCAGCAGCTGCAGGACCAGTTCATCGAGGGTGAAGAGGCTGGTA
ACACCCAGCTGAAGCAGAAGCGCATGAAGCAGCTGAAGGAGGCCGAAACCAAGACTCAGAA
GCTGGCTGCCGCTCTGAACGTGCACAAGGACGACCCACTGCTGCAGGTCTACTCTACCACTC
AGGAGAAGCTGGACGCTGTGACTAGCCAGCTGGAGAAGGAAGTCAAGAAGTCTAAGGGCTA
CGAGCGCGAAATCGAGGACCTGCACGGAGAATTCGAGCTGGACCGCCTGGACTACCTGGAC
ACCATCCGTAAGCAGGACCAGCAGCTGAAGCTGCTGATGCAGATCATGGACAAGATCCAGCC
TATCATCAAGAAGGACACTAACTACTCAAACGTGGACCGTATCAAGAAGGAAGCCGTCTGGA
ACGAAGACGAGTCCAGGTGGATCCTGCCCGAGATGTCTATGTCAAGAACCATCCTGCCACTG
GCTAACAACGGCTACATGCAGGAACCTGCCCGCCAGGAGAACACTCTGCTGCGTTCAAACTT
CGACGACAAGCTGCGCGAACGTCTGGCTAAGTCCGACAGCGAGAACCTGGCCAACTCCTAC

TTCAAGCCCGTGAAGCAGATCAACGTCATCAACAAGTACAAGAGCGACCAGAAGCTGTCTAC
CTCAAAGTCCCTGTTCCCCTCTAAGACCCCAACTTTCGACGGACTGGTGAACGGTGTGGTCT
ACACTGACGCTCTGTACGAACGCGCTCAGTCAGCTAAGAGGCCTCCCAGACTGGCTTCCCTG
AACCCTAAGGGCGCGCCCATGGAGATCGGAACCGGTTTCCCATTCGACCCTCACTACGTGGA
AGTCCTGGGAGAGAGGATGCACTACGTGGACGTCGGCCCAAGAGACGGAACCCCTGTGCTG
TTCCTGCACGGTAACCCTACTTCCAGCTACGTGTGGCGCAACATCATCCCACACGTCGCTCC
TACTCACCGTTGCATCGCCCCCGACCTGATCGGCATGGGAAAGTCTGACAAGCCAGACCTGG
GTTACTTCTTCGACGACCACGTGCGTTTCATGGACGCCTTCATCGAGGCTCTGGGCCTGGAA
GAGGTGGTCCTGGTCATCCACGACTGGGGTTCAGCTCTGGGCTTCCACTGGGCCAAGCGCA
ACCCCGAACGTGTGAAGGGCATCGCTTTCATGGAGTTCATCCGCCCCATCCCAACCTGGGAC
GAATGGCCAGAGTTCGCTCGTGAAACTTTCCAGGCCTTCAGGACCACTGACGTGGGAAGAAA
GCTGATCATCGACCAGAACGTCTTCATCGAGGGCACCCTGCCTATGGGAGTGGTCAGGCCC
CTGACTGAAGTGGAGATGGACCACTACAGAGAACCCTTCCTGAACCCAGTCGACAGGGAGC
CTCTGTGGAGATTCCCTAACGAACTGCCCATCGCTGGTGAACCTGCTAACATCGTGGCCCTG
GTCGAAGAGTACATGGACTGGCTGCACCAGAGCCCTGTGCCCAAGCTGCTGTTCTGGGGTA
CCCCAGGCGTCCTGATCCCACCTGCTGAGGCCGCTAGGCTGGCCAAGTCTCTGCCTAACTG
CAAGGCTGTGGACATCGGTCCCGGCCTGAACCTGCTGCAGGAAGACAACCCTGACCTGATC
GGATCAGAGATCGCCAGATGGTTGAGCACACTGGAAATCTCCGGCGGCGACTACAAGGACG
ACGACGATAAGTAAGCGGCCGC

Color-coded protein sequence:

OSM-3G444E_ Halo_Flag

M A E S V R V A V R C R P F N Q R E K D L N T T L C V G M T P N V G Q V N L N A P D G A A
K D F T F D G A Y F M D S T G E Q I Y N D I V F P L V E N V I E G Y N G T V F A Y G Q T G S G
K T F S M Q G I E T I P A Q R G V I P R A F D H I F T A T A T T E N V K F L V H C S Y L E I Y N
E E V R D L L G A D N K Q K L E I K E Q P D R G V Y V A G L S M H V C H D V P A C K E L M T
R G F N N R H V G A T L M N K D S S R S H S I F T V Y V E G M T E T G S I R M G K L N L V D
L A G S E R Q S K T G A T G D R L K E A T K I N L S L S A L G N V I S A L V D G K S K H I P Y
R D S K L T R L L Q D S L G G N T K T I M I A C V S P S S D N Y D E T L S T L R Y A N R A K N
I K N K P T I N E D P K D A L L R E Y Q E E I A R L K S M V Q P G A V G V G A P A Q D A F S I
E E E R K K L R E E F E E A M N D L R G E Y E R E Q T S K A E L Q K D L E S L R A D Y E R A
N A N L D N L N P E E A A K K I Q Q L Q D Q F I E G E E A G N T Q L K Q K R M K Q L K E A E
T K T Q K L A A A L N V H K D D P L L Q V Y S T T Q E K L D A V T S Q L E K E V K K S K G Y E
R E I E D L H G E F E L D R L D Y L D T I R K Q D Q Q L K L L M Q I M D K I Q P I I K K D T N Y
S N V D R I K K E A V W N E D E S R W I L P E M S M S R T I L P L A N N G Y M Q E P A R Q E
N T L L R S N F D D K L R E R L A K S D S E N L A N S Y F K P V K Q I N V I N K Y K S D Q K L
S T S K S L F P S K T P T F D G L V N G V V Y T D A L Y E R A Q S A K R P P R L A S L N P K
G A P M E I G T G F P F D P H Y V E V L G E R M H Y V D V G P R D G T P V L F L H G N P T S
S Y V W R N I I P H V A P T H R C I A P D L I G M G K S D K P D L G Y F F D D H V R F M D A F
I E A L G L E E V V L V I H D W G S A L G F H W A K R N P E R V K G I A F M E F I R P I P T W
D E W P E F A R E T F Q A F R T T D V G R K L I I D Q N V F I E G T L P M G V V R P L T E V E
M D H Y R E P F L N P V D R E P L W R F P N E L P I A G E P A N I V A L V E E Y M D W L H Q
S P V P K L L F W G T P G V L I P P A E A A R L A K S L P N C K A V D I G P G L N L L Q E D N
P D L I G S E I A R W L S T L E I S G G D Y K D D D D K **Stop**

9.3.2 OSM-3(G444E)^{Flag} (OSM-3 sequence with the G444E mutation C-terminally tagged with Flag)

Cloning sites into the pFastBac1 vector: SpeI and Not I

ACTAGTATGGCAGAGAGCGTCCGGGTCGCCGTAAGATGTCGTCCGTTCAATCAGAGAGAAAA
GGACCTGAATACGACGCTATGCGTCGGAATGACTCCGAACGTTGGACAGGTCAACCTGAACG
CGCCGGACGGGGCGGCCAAGGACTTCACGTTCGATGGAGCCTACTTTATGGATTCGACCGG
CGAGCAGATTTACAATGATATTGTCTTTCCGCTAGTTGAGAACGTGATAGAAGGCTACAATGG
CACTGTGTTTGCCTATGGCCAAACTGGATCGGGCAAGACTTTCTCCATGCAGGGCATCGAAA
CAATTCCAGCTCAACGGGGTGTGATTCCACGGGCTTTTGATCACATATTCACCGCCACGGCT
ACGACGGAAAATGTGAAATTCCTGGTGCACTGCAGCTATTTAGAGATTTACAACGAAGAGGTT
AGAGACTTGCTGGGCGCCGACAATAAACAAAAACTGGAGATCAAAGAGCAACCGGATCGGG
GTGTCTATGTGGCGGGCCTCTCCATGCATGTTTGTCATGATGTCCCGGCTTGCAAGGAGCTG
ATGACTCGGGGCTTCAACAATCGGCACGTCGGCGCCACGTTGATGAACAAGGACTCTTCCCG
AAGTCACTCAATCTTCACGGTATACGTGGAAGGCATGACAGAAACCGGATCGATCAGGATGG
GAAAGTTGAATCTGGTCGATTTGGCTGGAAGTGAGCGGCAGAGCAAGACAGGAGCCACCGG
TGACCGTTTGAAGGAGGCCACGAAGATTAACCTATCGCTGTCGGCGTTGGGTAATGTGATAT
CGGCGTTGGTGGACGGAAAGTCGAAGCATATACCCTACAGGGACAGTAAGCTGACTAGGTTG
TTACAGGATTCTCTTGGTGGTAACACAAAGACCATTATGATCGCCTGCGTGTCCCCATCCAGT
GACAACTACGACGAGACTCTCTCCACACTTCGATATGCCAACCGTGCCAAGAACATCAAGAA
CAAGCCGACGATCAACGAGGATCCAAAGGATGCTCTTCTTCGAGAGTACCAGGAGGAAATCG
CTCGGCTCAAGTCTATGGTTCAACCGGGGGCCGTTGGAGTTGGCGCTCCTGCGCAGGACGC
TTTCTCGATAGAAGAGGAGAGGAAGAAGCTACGGGAAGAATTCGAGGAGGCGATGAACGACT
TGCGTGGCGAGTATGAGCGGGAGCAGACGAGTAAAGCGGAGCTACAGAAGGACCTGGAGTC
CTTGAGAGCAGACTATGAAAGGGCTAATGCGAATTTAGACAACTTGAATCCGGAAGAAGCGG
CGAAGAAGATCCAACAGCTCCAAGATCAGTTTATTGAAGGAGAAGAAGCAGGCAATACTCAG
CTGAAGCAAAAACGGATGAAGCAGCTGAAGGAGGCAGAGACTAAAACGCAGAAGTTGGCAG
CCGCGTTAAACGTTCATAAGGATGATCCTCTGCTTCAAGTCTACAGTACTACTCAAGAAAAAC
TTGACGCAGTTACTTCTCAACTGGAGAAGGAAGTCAAGAAATCCAAAGGTTACGAGCGAGAA
ATCGAGGATCTCCACGGCGAATTCGAACTGGATCGTCTCGATTATCTAGACACAATTCGGAAG
CAGGACCAGCAGTTGAAGCTCCTTATGCAGATTATGGACAAAATCCAGCCGATCATCAAGAAA
GATACGAATTATAGTAACGTGGATCGGATAAAGAAGGAGGCGGTGTGGAATGAAGACGAGAG
TCGATGGATTTTGCCGGAAATGTCGATGAGTCGGACTATTCTGCCGTTGGCTAATAATGGTTA
TATGCAAGAACCTGCTCGGCAAGAGAACACCTTATTACGGTCTAACTTTGACGACAAACTACG
CGAGCGGCTAGCGAAAAGTGACTCGGAAAACCTGGCAAACAGCTACTTCAAGCCAGTGAAGC
AGATCAATGTGATCAACAAGTACAAGAGTGATCAAAAATTATCAACTTCCAAATCGCTATTTCC
ATCCAAGACCCCAACATTCGATGGTCTTGTCAACGGAGTCGTCTACACTGATGCTCTCTACGA
GCGGGCTCAATCTGCAAAACGACCACCTCGACTAGCCTCTCTGAATCCCAAAGGGCCCGACT
ACAAGGACGATGACGACAAGTGAGCGGCCGC

Color-coded protein sequence:

OSM-3G444E_Flag

M A E S V R V A V R C R P F N Q R E K D L N T T L C V G M T P N V G Q V N L N A P D G A A
K D F T F D G A Y F M D S T G E Q I Y N D I V F P L V E N V I E G Y N G T V F A Y G Q T G S G
K T F S M Q G I E T I P A Q R G V I P R A F D H I F T A T A T T E N V K F L V H C S Y L E I Y N
E E V R D L L G A D N K Q K L E I K E Q P D R G V Y V A G L S M H V C H D V P A C K E L M T
R G F N N R H V G A T L M N K D S S R S H S I F T V Y Y V E G M T E T G S I R M G K L N L V D

L A G S E R Q S K T G A T G D R L K E A T K I N L S L S A L G N V I S A L V D G K S K H I P Y
R D S K L T R L L Q D S L G G N T K T I M I A C V S P S S D N Y D E T L S T L R Y A N R A K N
I K N K P T I N E D P K D A L L R E Y Q E E I A R L K S M V Q P G A V G V G A P A Q D A F S I
E E E R K K L R E E F E E A M N D L R G E Y E R E Q T S K A E L Q K D L E S L R A D Y E R A
N A N L D N L N P E E A A K K I Q Q L Q D Q F I E G E E A G N T Q L K Q K R M K Q L K E A E
T K T Q K L A A A L N V H K D D P L L Q V Y S T T Q E K L D A V T S Q L E K E V K K S K G Y E
R E I E D L H G E F E L D R L D Y L D T I R K Q D Q Q L K L L M Q I M D K I Q P I I K K D T N Y
S N V D R I K K E A V W N E D E S R W I L P E M S M S R T I L P L A N N G Y M Q E P A R Q E
N T L L R S N F D D K L R E R L A K S D S E N L A N S Y F K P V K Q I N V I N K Y K S D Q K L
S T S K S L F P S K T P T F D G L V N G V V Y T D A L Y E R A Q S A K R P P R L A S L N P K
G P D Y K D D D D K Stop

9.3.3 OSM-3^{SNAP} (wild type OSM-3 sequence N-terminally tagged with Flag and SNAP)

Cloning sites into the pFastBac1 vector: SpeI and Not I

ACTAGTATGGATTACAAAGATGACGATGACAAAGGTGGAATGGACAAAGACTGCGAAATGAAA
AGAACAACTCTGGACAGCCCGCTCGGAAAACTGGAACTGTCAGGTTGCGAGCAGGGCCTGC
ACGAAATCAAGCTGCTGGGCAAGGGCACCTCCGCTGCTGACGCTGTGGAGGTCCCAGCTCC
TGCTGCTGTGCTGGGTGGCCCTGAACCACTGATGCAGGCCACTGCTTGGCTGAACGCCTACT
TCCACCAGCCAGAGGCTATCGAGGAATTCCCAGTCCCTGCTCTGCACCACCCTGTGTTCCAG
CAGGAAAGCTTCACCCGCCAGGTCCTGTGGAAGCTGCTGAAGGTGGTCAAGTTCGGAGAGG
TCATCTCTTACCAACAACTCGCTGCTCTGGCTGGTAACCCAGCTGCTACCGCTGCCGTCAAG
ACTGCTCTGTCCGGCAACCCCGTGCCAATCCTGATCCCTTGCCACAGGGTGGTGTCCAGCTC
TGGAGCTGTCGGAGGTTACGAGGGCGGACTGGCTGTGAAGGAGTGGCTGCTGGCTCACGAA
GGACACAGACTGGGCAAGCCTGGACTGGGCGCGCCAGGTGGCGGAAGCGGTGGCTCTATG
GCCGAGTCAGTGAGGGTCGCTGTGCGCTGCCGTCCATTCAACCAGAGAGAAAAGGACCTGA
ACACCACTCTGTGCGTGGGAATGACCCCTAACGTCGGTCAGGTGAACCTGAACGCCCCCGA
CGGAGCTGCCAAGGACTTCACCTTCGACGGTGCTTACTTCATGGACTCCACTGGCGAACAGA
TCTACAACGACATCGTCTTCCCTCTGGTCGAAAACGTGATCGAGGGATACAACGGTACTGTGT
TCGCTTACGGACAGACTGGAAGCGGAAAGACTTTCTCTATGCAGGGAATCGAGACTATCCCT
GCTCAGCGCGGTGTCATCCCTAGGGCTTTCGACCACATCTTCACCGCCACTGCTACCACTGA
GAACGTCAAGTTCCTGGTGCACTGCAGCTACCTGGAAATCTACAACGAGGAAGTGCGCGACC
TGCTGGGTGCTGACAACAAGCAGAAGCTGGAAATCAAGGAGCAGCCTGACCGTGGTGTCTA
CGTGGCCGGCCTGTCTATGCACGTCTGCCACGACGTGCCCGCTTGCAAGGAGCTGATGACC
AGGGGCTTCAACAACAGACACGTCGGAGCCACTCTGATGAACAAGGACTCATCCAGGAGCCA
CTCTATCTTCACCGTCTACGTGGAAGGAATGACCGAGACTGGTAGCATCAGAATGGGCAAGC
TGAACCTGGTGGACCTGGCTGGCTCAGAGAGGCAGTCCAAGACCGGCGCCACTGGAGACAG
ACTGAAGGAAGCTACCAAGATCAACCTGTCACTGTCCGCCCTGGGCAACGTCATCTCAGCTC
TGGTGGACGGAAAGTCCAAGCACATCCCCTACAGGGACAGCAAGCTGACTAGACTGCTGCA
GGACTCTCTGGGAGGTAATACCAAGACTATCATGATCGCTTGCGTCAGCCCAAGCTCTGACA
ACTACGACGAAACCCTGTCTACTCTGCGCTACGCCAACCGTGCTAAGAACATCAAGAACAAG
CCTACCATCAACGAGGACCCCAAGGACGCCCTGCTGAGGGAATACCAGGAAGAGATCGCTA
GACTGAAGAGCATGGTGCAACCTGGTGCTGTGGGTGTGGGCGCCCCAGCTCAGGACGCTTT
CTCTATCGAGGAAGAGAGGAAGAAGCTGAGAGAAGAGTTCGAAGAGGCTATGAACGACCTG
CGCGGCGAATACGAGCGTGAACAGACTTCAAAGGCCGAGCTGCAGAAGGACCTGGAATCCC
TGAGGGCTGACTACGAGAGAGCCAACGCTAACCTGGACAACCTGAACCCTGAAGAGGCTGC
CAAGAAGATCCAGCAGCTGCAGGACCAGTTCATCGGCGGAGAAGAGGCCGGTAACACCCAG
CTGAAGCAGAAGCGTATGAAGCAGCTGAAGGAAGCTGAAACCAAGACTCAGAAGCTGGCTG
CCGCTCTGAACGTCCACAAGGACGACCCCCTGCTGCAGGTGTACAGCACCACTCAGGAGAA
GCTGGACGCCGTCACTTCACAGCTGGAGAAGGAAGTGAAGAAGTCCAAGGGTTACGAGAGG

GAAATCGAGGACCTGCACGGCGAATTCGAGCTGGACCGCCTGGACTACCTGGACACCATCC
GTAAGCAGGACCAGCAGCTGAAGCTGCTGATGCAGATCATGGACAAGATCCAGCCCATCATC
AAGAAGGACACTAACTACAGCAACGTCGACCGCATCAAGAAGGAAGCTGTGTGGAACGAAGA
CGAGTCTCGCTGGATCCTGCCAGAAATGAGCATGTCTCGTACCATCCTGCCTCTGGCCAACA
ACGGTTACATGCAGGAGCCCGCTCGCCAGGAAAACACTCTGCTGCGTTCAAACTTCGACGAC
AAGCTGAGGGAGAGACTGGCCAAGTCAGACTCCGAAAACCTGGCTAACTCCTACTTCAAGCC
AGTCAAGCAGATCAACGTGATCAACAAGTACAAGTCAGACCAGAAGCTGAGCACCTCTAAGT
CACTGTTCCCATCCAAGACCCCTACTTTCGACGGCCTGGTCAACGGAGTGGTCTACACTGAC
GCCCTGTACGAGCGCGCCCAGTCTGCTAAGCGCCCTCCCCGTCTGGCTTCTCTGAACCCAAA
AGGGCCCTAAGCGGCCGC

Color-coded protein sequence:

Flag_SNAP_WT_OSM-3

M D Y K D D D D K G G M D K D C E M K R T T L D S P L G K L E L S G C E Q G L H E I K L L G
K G T S A A D A V E V P A P A A V L G G P E P L M Q A T A W L N A Y F H Q P E A I E E F P V
P A L H H P V F Q Q E S F T R Q V L W K L L K V V K F G E V I S Y Q Q L A A L A G N P A A T
A A V K T A L S G N P V P I L I P C H R V V S S S G A V G G Y E G G L A V K E W L L A H E G
H R L G K P G L G A P G G G S G G S M A E S V R V A V R C R P F N Q R E K D L N T T L C V
G M T P N V G Q V N L N A P D G A A K D F T F D G A Y F M D S T G E Q I Y N D I V F P L V E
N V I E G Y N G T V F A Y G Q T G S G K T F S M Q G I E T I P A Q R G V I P R A F D H I F T A
T A T T E N V K F L V H C S Y L E I Y N E E V R D L L G A D N K Q K L E I K E Q P D R G V Y V
A G L S M H V C H D V P A C K E L M T R G F N N R H V G A T L M N K D S S R S H S I F T V Y
V E G M T E T G S I R M G K L N L V D L A G S E R Q S K T G A T G D R L K E A T K I N L S L S
A L G N V I S A L V D G K S K H I P Y R D S K L T R L L Q D S L G G N T K T I M I A C V S P S S
D N Y D E T L S T L R Y A N R A K N I K N K P T I N E D P K D A L L R E Y Q E E I A R L K S M
V Q P G A V G V G A P A Q D A F S I E E E R K K L R E E F E E A M N D L R G E Y E R E Q T S
K A E L Q K D L E S L R A D Y E R A N A N L D N L N P E E A A K K I Q Q L Q D Q F I G G E E A
G N T Q L K Q K R M K Q L K E A E T K T Q K L A A A L N V H K D D P L L Q V Y S T T Q E K L
D A V T S Q L E K E V K K S K G Y E R E I E D L H G E F E L D R L D Y L D T I R K Q D Q Q L K
L L M Q I M D K I Q P I I K K D T N Y S N V D R I K K E A V W N E D E S R W I L P E M S M S R
T I L P L A N N G Y M Q E P A R Q E N T L L R S N F D D K L R E R L A K S D S E N L A N S Y F
K P V K Q I N V I N K Y K S D Q K L S T S K S L F P S K T P T F D G L V N G V V Y T D A L Y E
R A Q S A K R P P R L A S L N P K G P **Stop**

9.3.4 OSM-3^{Flag} (wild type OSM-3 sequence C-terminally tagged with Flag)

Cloning sites into the pFastBac1 vector: SpeI and Not I

ACTAGTATGGCAGAAAGCGTTAGAGTGGCAGTTAGATGTAGACCGTTCAACCAGAGAGAAAA
AGACCTCAACACAACCCTGTGCGTGGGCATGACCCCAAACGTGGGCCAGGTCAACCTGAAC
GCTCCTGACGGAGCTGCCAAGGACTTCACCTTCGACGGAGCCTACTTCATGGACTCCACTGG
TGAACAGATCTACAACGACATCGTGTTCCCACTGGTGGAAAACGTCATCGAGGGATACAACG
GTACCGTCTTCGCTTACGGACAGACCGGCTCAGGAAAGACTTTCTCCATGCAGGGTATCGAG
ACTATCCCAGCTCAGAGGGGCGTGATCCCTAGAGCCTTCGACCACATCTTCACCGCCACTGC
TACCACTGAAAACGTGAAGTTCCTGGTCCACTGCTCCTACCTGGAGATCTACAACGAGGAAG
TCAGGGACCTGCTGGGTGCCGACAACAAGCAGAAGCTGGAAATCAAGGAGCAGCCAGACAG
AGGAGTGTACGTCGCTGGTCTGAGCATGCACGTGTGCCACGACGTCCCTGCCTGCAAGGAG
CTGATGACCCGCGGTTTCAACAACCGTCACGTGGGCGCTACTCTGATGAACAAGGACTCCAG
CCGCTCTCACTCAATCTTCACCGTGTACGTCGAAGGCATGACCGAGACTGGAAGCATCCGTA
TGGGCAAGCTGAACCTCGTGGACCTGGCTGGATCTGAAAGGCAGTCTAAGACCGGCGCTAC

TGGTGACCGCCTGAAGGAGGCCACCAAGATCAACCTGTCCCTGAGCGCTCTGGGAAACGTG
ATCAGCGCCCTGGTCGACGGCAAGTCTAAGCACATCCCTTACCGCGACTCAAAGCTGACTCG
TCTGCTGCAGGACTCCCTGGGTGGCAACACCAAGACTATCATGATCGCTTGCGTGTCACCCT
CTTCAGACAACTACGACGAAACCCTGTCCACTCTGCGCTACGCCAACCGTGCTAAGAACATC
AAGAACAAGCCCACCATCAACGAAGACCCAAAGGACGCTCTGCTGAGGGAGTACCAGGAGG
AAATCGCCAGACTGAAGAGCATGGTGCAACCTGGTGCTGTGGGTGTGGGCGCCCCAGCTCA
GGACGCTTTCTCTATCGAGGAAGAGAGGAAGAAGCTGAGAGAAGAGTTCGAAGAGGCTATGA
ACGACCTGAGGGGCGAATACGAGAGAGAACAGACTAGCAAGGCTGAACTGCAGAAGGACCT
GGAGTCTCTGCGCGCCGACTACGAGCGTGCCAACGCTAACCTGGACAACCTGAACCCCGAA
GAGGCTGCCAAGAAGATCCAGCAGCTGCAGGACCAGTTCATCGGAGGTGAAGAGGCTGGTA
ACACCCAGCTGAAGCAGAAGCGCATGAAGCAGCTGAAGGAGGCCGAAACCAAGACTCAGAA
GCTGGCTGCCGCTCTGAACGTGCACAAGGACGACCCACTGCTGCAGGTCTACTCTACCACTC
AGGAGAAGCTGGACGCTGTGACTAGCCAGCTGGAGAAGGAAGTCAAGAAGTCTAAGGGCTA
CGAGCGCGAAATCGAGGACCTGCACGGAGAATTCGAGCTGGACCGCCTGGACTACCTGGAC
ACCATCCGTAAGCAGGACCAGCAGCTGAAGCTGCTGATGCAGATCATGGACAAGATCCAGCC
TATCATCAAGAAGGACACTAACTACTCAAACGTGGACCGTATCAAGAAGGAAGCCGTCTGGA
ACGAAGACGAGTCCAGGTGGATCCTGCCCGAGATGTCTATGTCAAGAACCATCCTGCCACTG
GCTAACAACGGCTACATGCAGGAACCTGCCCGCCAGGAGAACACTCTGCTGCGTTCAAACTT
CGACGACAAGCTGCGCGAACGTCTGGCTAAGTCCGACAGCGAGAACCTGGCCAACTCCTAC
TTCAAGCCCGTGAAGCAGATCAACGTCATCAACAAGTACAAGAGCGACCAGAAGCTGTCTAC
CTCAAAGTCCCTGTTCCCCTCTAAGACCCCAACTTTCGACGGACTGGTGAACGGTGTGGTCT
ACACTGACGCTCTGTACGAACGCGCTCAGTCAGCTAAGAGGCCTCCCAGACTGGCTTCCCTG
AACCCTAAGGGCGGCGACTACAAGGACGACGACGATAAGTAAGCGGCCGC

Color-coded protein sequence

WT_OSM-3_Flag

M A E S V R V A V R C R P F N Q R E K D L N T T L C V G M T P N V G Q V N L N A P D G A A
K D F T F D G A Y F M D S T G E Q I Y N D I V F P L V E N V I E G Y N G T V F A Y G Q T G S G
K T F S M Q G I E T I P A Q R G V I P R A F D H I F T A T A T T E N V K F L V H C S Y L E I Y N
E E V R D L L G A D N K Q K L E I K E Q P D R G V Y V A G L S M H V C H D V P A C K E L M T
R G F N N R H V G A T L M N K D S S R S H S I F T V Y V E G M T E T G S I R M G K L N L V D
L A G S E R Q S K T G A T G D R L K E A T K I N L S L S A L G N V I S A L V D G K S K H I P Y
R D S K L T R L L Q D S L G G N T K T I M I A C V S P S S D N Y D E T L S T L R Y A N R A K N
I K N K P T I N E D P K D A L L R E Y Q E E I A R L K S M V Q P G A V G V G A P A Q D A F S I
E E E R K K L R E E F E E A M N D L R G E Y E R E Q T S K A E L Q K D L E S L R A D Y E R A
N A N L D N L N P E E A A K K I Q Q L Q D Q F I G G E E A G N T Q L K Q K R M K Q L K E A E
T K T Q K L A A A L N V H K D D P L L Q V Y S T T Q E K L D A V T S Q L E K E V K K S K G Y E
R E I E D L H G E F E L D R L D Y L D T I R K Q D Q Q L K L L M Q I M D K I Q P I I K K D T N Y
S N V D R I K K E A V W N E D E S R W I L P E M S M S R T I L P L A N N G Y M Q E P A R Q E
N T L L R S N F D D K L R E R L A K S D S E N L A N S Y F K P V K Q I N V I N K Y K S D Q K L
S T S K S L F P S K T P T F D G L V N G V V Y T D A L Y E R A Q S A K R P P R L A S L N P K
G G D Y K D D D D K **Stop**

Bibliography

1. Bisgrove, B.W. and H.J. Yost, The roles of cilia in developmental disorders and disease. *Development*, 2006. **133**(21): p. 4131-43.
2. Caspers, H., Dobell, Clifford: Antony van Leeuwenhoek and his “Little Animals”. With 32 pl. New York, N. Y.: Dover Publ. Inc. 1960. VII/435 pp. $ 2,25. *Internationale Revue der gesamten Hydrobiologie und Hydrographie*, 1964. **49**(3): p. 503-503.
3. Dobell, C. and A.v. Leeuwenhoek, Antony van Leeuwenhoek and his "Little animals" : being some account of the father of protozoology and bacteriology and his multifarious discoveries in these disciplines. 1960, New York: Dover Publications.
4. Fliegauf, M., T. Benzing, and H. Omran, When cilia go bad: cilia defects and ciliopathies. *Nat Rev Mol Cell Biol*, 2007. **8**(11): p. 880-93.
5. Abou Alaiwi, W.A., S.T. Lo, and S.M. Nauli, Primary cilia: highly sophisticated biological sensors. *Sensors (Basel)*, 2009. **9**(9): p. 7003-20.
6. Wheatley, D.N., The primary cilium - once a "rudimentary" organelle that is now a ubiquitous sensory cellular structure involved in many pathological disorders. *J Cell Commun Signal*, 2018. **12**(1): p. 211-216.
7. Wang, Z., et al., Intraflagellar transport (IFT) protein IFT25 is a phosphoprotein component of IFT complex B and physically interacts with IFT27 in *Chlamydomonas*. *PLoS One*, 2009. **4**(5): p. e5384.
8. Bayless, B.A., F.M. Navarro, and M. Winey, Motile Cilia: Innovation and Insight From Ciliate Model Organisms. *Front Cell Dev Biol*, 2019. **7**: p. 265.
9. Kohl, L., D. Robinson, and P. Bastin, Novel roles for the flagellum in cell morphogenesis and cytokinesis of trypanosomes. *EMBO J*, 2003. **22**(20): p. 5336-46.
10. Scholey, J.M., Kinesin-2 motors transport IFT-particles, dyneins and tubulin subunits to the tips of *Caenorhabditis elegans* sensory cilia: relevance to vision research? *Vision Res*, 2012. **75**: p. 44-52.
11. Robinson, R., Ciliate genome sequence reveals unique features of a model eukaryote. *PLoS Biol*, 2006. **4**(9): p. e304.
12. Satir, P. and S.T. Christensen, Overview of structure and function of mammalian cilia. *Annu Rev Physiol*, 2007. **69**: p. 377-400.
13. Satir, P. and S.T. Christensen, Structure and function of mammalian cilia. *Histochem Cell Biol*, 2008. **129**(6): p. 687-93.

14. Nicastro, D., et al., The molecular architecture of axonemes revealed by cryoelectron tomography. *Science*, 2006. **313**(5789): p. 944-8.
15. Pigino, G., et al., Electron-tomographic analysis of intraflagellar transport particle trains in situ. *J Cell Biol*, 2009. **187**(1): p. 135-48.
16. Silflow, C.D. and P.A. Lefebvre, Assembly and motility of eukaryotic cilia and flagella. Lessons from *Chlamydomonas reinhardtii*. *Plant Physiol*, 2001. **127**(4): p. 1500-7.
17. Porter, M.E., et al., Cytoplasmic dynein heavy chain 1b is required for flagellar assembly in *Chlamydomonas*. *Mol Biol Cell*, 1999. **10**(3): p. 693-712.
18. Porter, M.E. and W.S. Sale, The 9 + 2 axoneme anchors multiple inner arm dyneins and a network of kinases and phosphatases that control motility. *J Cell Biol*, 2000. **151**(5): p. F37-42.
19. Johnson, K.A., Keeping the beat: Form meets function in the *Chlamydomonas* flagellum. *BioEssays*, 1995. **17**(10): p. 847-854.
20. Perkins, L.A., et al., Mutant sensory cilia in the nematode *Caenorhabditis elegans*. *Dev Biol*, 1986. **117**(2): p. 456-87.
21. Dabdoub, A. and M.W. Kelley, Planar cell polarity and a potential role for a Wnt morphogen gradient in stereociliary bundle orientation in the mammalian inner ear. *J Neurobiol*, 2005. **64**(4): p. 446-57.
22. Sobkowicz, H.M., S.M. Slapnick, and B.K. August, The kinocilium of auditory hair cells and evidence for its morphogenetic role during the regeneration of stereocilia and cuticular plates. *J Neurocytol*, 1995. **24**(9): p. 633-53.
23. Hirokawa, N., et al., Nodal flow and the generation of left-right asymmetry. *Cell*, 2006. **125**(1): p. 33-45.
24. Pugacheva, E.N., et al., HEF1-dependent Aurora A activation induces disassembly of the primary cilium. *Cell*, 2007. **129**(7): p. 1351-63.
25. Pan, J. and W. Snell, The primary cilium: keeper of the key to cell division. *Cell*, 2007. **129**(7): p. 1255-7.
26. Geimer, S. and M. Melkonian, The ultrastructure of the *Chlamydomonas reinhardtii* basal apparatus: identification of an early marker of radial asymmetry inherent in the basal body. *J Cell Sci*, 2004. **117**(Pt 13): p. 2663-74.
27. Beisson, J. and M. Wright, Basal body/centriole assembly and continuity. *Curr Opin Cell Biol*, 2003. **15**(1): p. 96-104.
28. Breslow, D.K., et al., An in vitro assay for entry into cilia reveals unique properties of the soluble diffusion barrier. *J Cell Biol*, 2013. **203**(1): p. 129-47.

29. Czarnecki, P.G. and J.V. Shah, The ciliary transition zone: from morphology and molecules to medicine. *Trends Cell Biol*, 2012. **22**(4): p. 201-10.
30. Garcia-Gonzalo, F.R. and J.F. Reiter, Open Sesame: How Transition Fibers and the Transition Zone Control Ciliary Composition. *Cold Spring Harb Perspect Biol*, 2017. **9**(2).
31. Reiter, J.F., O.E. Blacque, and M.R. Leroux, The base of the cilium: roles for transition fibres and the transition zone in ciliary formation, maintenance and compartmentalization. *EMBO Rep*, 2012. **13**(7): p. 608-18.
32. Tyler, K.M., et al., Flagellar membrane localization via association with lipid rafts. *J Cell Sci*, 2009. **122**(Pt 6): p. 859-66.
33. Serricchio, M., et al., Flagellar membranes are rich in raft-forming phospholipids. *Biol Open*, 2015. **4**(9): p. 1143-53.
34. Simons, K. and R. Ehehalt, Cholesterol, lipid rafts, and disease. *J Clin Invest*, 2002. **110**(5): p. 597-603.
35. Molla-Herman, A., et al., The ciliary pocket: an endocytic membrane domain at the base of primary and motile cilia. *J Cell Sci*, 2010. **123**(Pt 10): p. 1785-95.
36. Benmerah, A., The ciliary pocket. *Curr Opin Cell Biol*, 2013. **25**(1): p. 78-84.
37. Overath, P. and M. Engstler, Endocytosis, membrane recycling and sorting of GPI-anchored proteins: *Trypanosoma brucei* as a model system. *Mol Microbiol*, 2004. **53**(3): p. 735-44.
38. Marshall, W.F. and S. Nonaka, Cilia: tuning in to the cell's antenna. *Curr Biol*, 2006. **16**(15): p. R604-14.
39. Inaba, K. and K. Mizuno, Sperm dysfunction and ciliopathy. *Reprod Med Biol*, 2016. **15**(2): p. 77-94.
40. Jain, R., et al., Sensory functions of motile cilia and implication for bronchiectasis. *Front Biosci (Schol Ed)*, 2012. **4**: p. 1088-98.
41. Afzelius, B.A., A human syndrome caused by immotile cilia. *Science*, 1976. **193**(4250): p. 317-9.
42. Eliasson, R., et al., The immotile-cilia syndrome. A congenital ciliary abnormality as an etiologic factor in chronic airway infections and male sterility. *N Engl J Med*, 1977. **297**(1): p. 1-6.
43. Pazour, G.J., et al., *Chlamydomonas* IFT88 and its mouse homologue, polycystic kidney disease gene tg737, are required for assembly of cilia and flagella. *J Cell Biol*, 2000. **151**(3): p. 709-18.
44. Long, H. and K. Huang, Transport of Ciliary Membrane Proteins. *Front Cell Dev Biol*, 2019. **7**: p. 381.

45. Fai, T.G., et al., Length regulation of multiple flagella that self-assemble from a shared pool of components. *Elife*, 2019. **8**.
46. Ma, R., et al., Speed and Diffusion of Kinesin-2 Are Competing Limiting Factors in Flagellar Length-Control Model. *Biophys J*, 2020.
47. Marshall, W.F., et al., Flagellar length control system: testing a simple model based on intraflagellar transport and turnover. *Mol Biol Cell*, 2005. **16**(1): p. 270-8.
48. Pazour, G.J., et al., Proteomic analysis of a eukaryotic cilium. *J Cell Biol*, 2005. **170**(1): p. 103-13.
49. Kozminski, K.G., et al., A motility in the eukaryotic flagellum unrelated to flagellar beating. *Proc Natl Acad Sci USA*, 1993. **90**(12): p. 5519-23.
50. Kozminski, K.G., P.L. Beech, and J.L. Rosenbaum, The *Chlamydomonas* kinesin-like protein FLA10 is involved in motility associated with the flagellar membrane. *J Cell Biol*, 1995. **131**(6 Pt 1): p. 1517-27.
51. Hao, L., et al., Analysis of intraflagellar transport in *C. elegans* sensory cilia. *Methods Cell Biol*, 2009. **93**: p. 235-66.
52. Hao, L. and J.M. Scholey, Intraflagellar transport at a glance. *J Cell Sci*, 2009. **122**(Pt 7): p. 889-92.
53. Cole, D.G., et al., *Chlamydomonas* kinesin-II-dependent intraflagellar transport (IFT): IFT particles contain proteins required for ciliary assembly in *Caenorhabditis elegans* sensory neurons. *J Cell Biol*, 1998. **141**(4): p. 993-1008.
54. Cole, D.G., The intraflagellar transport machinery of *Chlamydomonas reinhardtii*. *Traffic*, 2003. **4**(7): p. 435-42.
55. Taschner, M., S. Bhogaraju, and E. Lorentzen, Architecture and function of IFT complex proteins in ciliogenesis. *Differentiation*, 2012. **83**(2): p. S12-22.
56. Pedersen, L.B., S. Geimer, and J.L. Rosenbaum, Dissecting the molecular mechanisms of intraflagellar transport in *Chlamydomonas*. *Curr Biol*, 2006. **16**(5): p. 450-9.
57. San Agustin, J.T., G.J. Pazour, and G.B. Witman, Intraflagellar transport is essential for mammalian spermiogenesis but is absent in mature sperm. *Mol Biol Cell*, 2015. **26**(24): p. 4358-72.
58. Prevo, B., et al., Functional differentiation of cooperating kinesin-2 motors orchestrates cargo import and transport in *C. elegans* cilia. *Nat Cell Biol*, 2015. **17**(12): p. 1536-45.
59. Prevo, B., J.M. Scholey, and E.J.G. Peterman, Intraflagellar transport: mechanisms of motor action, cooperation, and cargo delivery. *FEBS J*, 2017. **284**(18): p. 2905-2931.

60. Scholey, J.M., Kinesin-2: a family of heterotrimeric and homodimeric motors with diverse intracellular transport functions. *Annu Rev Cell Dev Biol*, 2013. **29**: p. 443-69.
61. Gindhart, J.G., Jr. and L.S. Goldstein, Tetratrico peptide repeats are present in the kinesin light chain. *Trends Biochem Sci*, 1996. **21**(2): p. 52-3.
62. Wedaman, K.P., et al., Sequence and submolecular localization of the 115-kD accessory subunit of the heterotrimeric kinesin-II (KRP85/95) complex. *J Cell Biol*, 1996. **132**(3): p. 371-80.
63. Pedersen, L.B. and J.L. Rosenbaum, Intraflagellar transport (IFT) role in ciliary assembly, resorption and signalling. *Curr Top Dev Biol*, 2008. **85**: p. 23-61.
64. Nonaka, S., et al., Randomization of left-right asymmetry due to loss of nodal cilia generating leftward flow of extraembryonic fluid in mice lacking KIF3B motor protein. *Cell*, 1998. **95**(6): p. 829-37.
65. Takeda, S., et al., Kinesin superfamily protein 3 (KIF3) motor transports fodrin-associating vesicles important for neurite building. *J Cell Biol*, 2000. **148**(6): p. 1255-65.
66. Brown, J.M., et al., Kinesin-II is preferentially targeted to assembling cilia and is required for ciliogenesis and normal cytokinesis in *Tetrahymena*. *Mol Biol Cell*, 1999. **10**(10): p. 3081-96.
67. Scholey, J.M., Intraflagellar transport motors in cilia: moving along the cell's antenna. *J Cell Biol*, 2008. **180**(1): p. 23-9.
68. Sonar, P., et al., Kinesin-2 from *C. reinhardtii* Is an Atypically Fast and Auto-inhibited Motor that Is Activated by Heterotrimerization for Intraflagellar Transport. *Curr Biol*, 2020. **30**(6): p. 1160-1166 e5.
69. Ou, G., et al., Functional coordination of intraflagellar transport motors. *Nature*, 2005. **436**(7050): p. 583-7.
70. Brunnbauer, M., et al., Regulation of a heterodimeric kinesin-2 through an unprocessive motor domain that is turned processive by its partner. *Proc Natl Acad Sci USA*, 2010. **107**(23): p. 10460-5.
71. Snow, J.J., et al., Two anterograde intraflagellar transport motors cooperate to build sensory cilia on *C. elegans* neurons. *Nat Cell Biol*, 2004. **6**(11): p. 1109-13.
72. Pan, X., et al., Mechanism of transport of IFT particles in *C. elegans* cilia by the concerted action of kinesin-II and OSM-3 motors. *J Cell Biol*, 2006. **174**(7): p. 1035-45.
73. Peden, E.M. and M.M. Barr, The KLP-6 kinesin is required for male mating behaviors and polycystin localization in *Caenorhabditis elegans*. *Curr Biol*, 2005. **15**(5): p. 394-404.

74. Engelke, M.F., et al., Acute Inhibition of Heterotrimeric Kinesin-2 Function Reveals Mechanisms of Intraflagellar Transport in Mammalian Cilia. *Curr Biol*, 2019. **29**(7): p. 1137-1148 e4.
75. Yang, Z., E.A. Roberts, and L.S. Goldstein, Functional analysis of mouse kinesin motor Kif3C. *Mol Cell Biol*, 2001. **21**(16): p. 5306-11.
76. Jenkins, P.M., et al., Ciliary targeting of olfactory CNG channels requires the CNGB1b subunit and the kinesin-2 motor protein, KIF17. *Curr Biol*, 2006. **16**(12): p. 1211-6.
77. Setou, M., et al., Kinesin superfamily motor protein KIF17 and mLin-10 in NMDA receptor-containing vesicle transport. *Science*, 2000. **288**(5472): p. 1796-802.
78. Insinna, C., et al., The homodimeric kinesin, Kif17, is essential for vertebrate photoreceptor sensory outer segment development. *Dev Biol*, 2008. **316**(1): p. 160-70.
79. Insinna, C. and J.C. Besharse, Intraflagellar transport and the sensory outer segment of vertebrate photoreceptors. *Dev Dyn*, 2008. **237**(8): p. 1982-92.
80. Toropova, K., et al., Structure of the dynein-2 complex and its assembly with intraflagellar transport trains. *Nat Struct Mol Biol*, 2019. **26**(9): p. 823-829.
81. Stepanek, L. and G. Pigino, Microtubule doublets are double-track railways for intraflagellar transport trains. *Science*, 2016. **352**(6286): p. 721-4.
82. Pazour, G.J., B.L. Dickert, and G.B. Witman, The DHC1b (DHC2) isoform of cytoplasmic dynein is required for flagellar assembly. *J Cell Biol*, 1999. **144**(3): p. 473-81.
83. Yi, P., et al., Dynein-Driven Retrograde Intraflagellar Transport Is Triphasic in *C. elegans* Sensory Cilia. *Curr Biol*, 2017. **27**(10): p. 1448-1461 e7.
84. Toropova, K., M. Mladenov, and A.J. Roberts, Intraflagellar transport dynein is autoinhibited by trapping of its mechanical and track-binding elements. *Nat Struct Mol Biol*, 2017. **24**(5): p. 461-468.
85. Mukhopadhyay, S., et al., TULP3 bridges the IFT-A complex and membrane phosphoinositides to promote trafficking of G protein-coupled receptors into primary cilia. *Genes Dev*, 2010. **24**(19): p. 2180-93.
86. Behal, R.H., et al., Subunit interactions and organization of the *Chlamydomonas reinhardtii* intraflagellar transport complex A proteins. *J Biol Chem*, 2012. **287**(15): p. 11689-703.
87. Jekely, G. and D. Arendt, Evolution of intraflagellar transport from coated vesicles and autogenous origin of the eukaryotic cilium. *Bioessays*, 2006. **28**(2): p. 191-8.
88. Rompolas, P., et al., *Chlamydomonas* FAP133 is a dynein intermediate chain associated with the retrograde intraflagellar transport motor. *J Cell Sci*, 2007. **120**(Pt 20): p. 3653-65.

89. Lucker, B.F., et al., Characterization of the intraflagellar transport complex B core: direct interaction of the IFT81 and IFT74/72 subunits. *J Biol Chem*, 2005. **280**(30): p. 27688-96.
90. Taschner, M. and E. Lorentzen, The Intraflagellar Transport Machinery. *Cold Spring Harb Perspect Biol*, 2016. **8**(10).
91. Cole, D.G. and W.J. Snell, SnapShot: Intraflagellar transport. *Cell*, 2009. **137**(4): p. 784-784 e1.
92. Taschner, M., et al., Intraflagellar transport proteins 172, 80, 57, 54, 38, and 20 form a stable tubulin-binding IFT-B2 complex. *EMBO J*, 2016. **35**(7): p. 773-90.
93. Taschner, M., et al., Crystal structures of IFT70/52 and IFT52/46 provide insight into intraflagellar transport B core complex assembly. *J Cell Biol*, 2014. **207**(2): p. 269-82.
94. Lechtreck, K.F., IFT-Cargo Interactions and Protein Transport in Cilia. *Trends Biochem Sci*, 2015. **40**(12): p. 765-778.
95. Lechtreck, K.F., et al., Protein transport in growing and steady-state cilia. *Traffic*, 2017. **18**(5): p. 277-286.
96. Mourao, A., S.T. Christensen, and E. Lorentzen, The intraflagellar transport machinery in ciliary signaling. *Curr Opin Struct Biol*, 2016. **41**: p. 98-108.
97. Xue, B., et al., Intraflagellar transport protein RABL5/IFT22 recruits the BBSome to the basal body through the GTPase ARL6/BBS3. *Proc Natl Acad Sci USA*, 2020. **117**(5): p. 2496-2505.
98. Wei, Q., et al., The BBSome controls IFT assembly and turnaround in cilia. *Nat Cell Biol*, 2012. **14**(9): p. 950-7.
99. Verhey, K.J. and J.W. Hammond, Traffic control: regulation of kinesin motors. *Nat Rev Mol Cell Biol*, 2009. **10**(11): p. 765-77.
100. Imanishi, M., et al., Autoinhibition regulates the motility of the *C. elegans* intraflagellar transport motor OSM-3. *J Cell Biol*, 2006. **174**(7): p. 931-7.
101. Jordan, M.A., et al., The cryo-EM structure of intraflagellar transport trains reveals how dynein is inactivated to ensure unidirectional anterograde movement in cilia. *Nat Cell Biol*, 2018. **20**(11): p. 1250-1255.
102. Hao, L., et al., Intraflagellar transport delivers tubulin isotypes to sensory cilium middle and distal segments. *Nat Cell Biol*, 2011. **13**(7): p. 790-8.
103. Ou, G., et al., Sensory ciliogenesis in *Caenorhabditis elegans*: assignment of IFT components into distinct modules based on transport and phenotypic profiles. *Mol Biol Cell*, 2007. **18**(5): p. 1554-69.

104. Burghoorn, J., et al., Mutation of the MAP kinase DYF-5 affects docking and undocking of kinesin-2 motors and reduces their speed in the cilia of *Caenorhabditis elegans*. *Proc Natl Acad Sci USA*, 2007. **104**(17): p. 7157-62.
105. Masyukova, S.V., et al., A Screen for Modifiers of Cilia Phenotypes Reveals Novel MKS Alleles and Uncovers a Specific Genetic Interaction between osm-3 and nphp-4. *PLoS Genet*, 2016. **12**(2): p. e1005841.
106. Baker, S.A., et al., IFT20 links kinesin II with a mammalian intraflagellar transport complex that is conserved in motile flagella and sensory cilia. *J Biol Chem*, 2003. **278**(36): p. 34211-8.
107. Bhogaraju, S., et al., Molecular basis of tubulin transport within the cilium by IFT74 and IFT81. *Science*, 2013. **341**(6149): p. 1009-12.
108. Wachter, S., et al., Binding of IFT22 to the intraflagellar transport complex is essential for flagellum assembly. *EMBO J*, 2019. **38**(9).
109. Rual, J.F., et al., Towards a proteome-scale map of the human protein-protein interaction network. *Nature*, 2005. **437**(7062): p. 1173-8.
110. Mohamed, M.A.A., W.L. Stepp, and Z. Ökten, Reconstitution reveals motor activation for intraflagellar transport. *Nature*, 2018. **557**(7705): p. 387-391.
111. Jerabek-Willemsen, M., et al., MicroScale Thermophoresis: Interaction analysis and beyond. *Journal of Molecular Structure*, 2014. **1077**: p. 101-113.
112. Yi, P., C. Xie, and G. Ou, The kinases male germ cell-associated kinase and cell cycle-related kinase regulate kinesin-2 motility in *Caenorhabditis elegans* neuronal cilia. *Traffic*, 2018. **19**(7): p. 522-535.
113. Stepp, W.L., et al., Kinesin-2 motors adapt their stepping behavior for processive transport on axonemes and microtubules. *EMBO Rep*, 2017. **18**(11): p. 1947-1956.
114. Stepp, W.L. and Z. Ökten, Resolving kinesin stepping: one head at a time. *Life Sci Alliance*, 2019. **2**(5).
115. Dave, D., et al., DYF-1 Is Required for Assembly of the Axoneme in *Tetrahymena thermophila*. *Eukaryotic Cell*, 2009. **8**(9): p. 1397-1406.
116. Pathak, N., C.A. Austin, and I.A. Drummond, Tubulin tyrosine ligase-like genes *ttll3* and *ttll6* maintain zebrafish cilia structure and motility. *J Biol Chem*, 2011. **286**(13): p. 11685-95.
117. Pathak, N., et al., The zebrafish fleer gene encodes an essential regulator of cilia tubulin polyglutamylation. *Mol Biol Cell*, 2007. **18**(11): p. 4353-64.
118. Sirajuddin, M., L.M. Rice, and R.D. Vale, Regulation of microtubule motors by tubulin isotypes and post-translational modifications. *Nat Cell Biol*, 2014. **16**(4): p. 335-44.

119. O'Hagan, R., et al., The tubulin deglutamylase CCPP-1 regulates the function and stability of sensory cilia in *C. elegans*. *Curr Biol*, 2011. **21**(20): p. 1685-94.
120. Howard, P.W., S.F. Jue, and R.A. Maurer, Interaction of mouse TTC30/DYF-1 with multiple intraflagellar transport complex B proteins and KIF17. *Exp Cell Res*, 2013. **319**(14): p. 2275-81.
121. Wang, L. and B.D. Dynlacht, The regulation of cilium assembly and disassembly in development and disease. *Development*, 2018. **145**(18).
122. Guillaud, L., R. Wong, and N. Hirokawa, Disruption of KIF17-Mint1 interaction by CaMKII-dependent phosphorylation: a molecular model of kinesin-cargo release. *Nat Cell Biol*, 2008. **10**(1): p. 19-29.
123. Liang, Y., et al., FLA8/KIF3B phosphorylation regulates kinesin-II interaction with IFT-B to control IFT entry and turnaround. *Dev Cell*, 2014. **30**(5): p. 585-97.
124. Taschner, M., et al., Crystal structure of intraflagellar transport protein 80 reveals a homo-dimer required for ciliogenesis. *Elife*, 2018. **7**.
125. Vannuccini, E., et al., Two classes of short intraflagellar transport train with different 3D structures are present in *Chlamydomonas* flagella. *J Cell Sci*, 2016. **129**(10): p. 2064-74.
126. Taschner, M., et al., Biochemical mapping of interactions within the intraflagellar transport (IFT) B core complex: IFT52 binds directly to four other IFT-B subunits. *J Biol Chem*, 2011. **286**(30): p. 26344-52.
127. Brazelton, W.J., et al., The *bld1* mutation identifies the *Chlamydomonas osm-6* homolog as a gene required for flagellar assembly. *Curr Biol*, 2001. **11**(20): p. 1591-4.
128. Deane, J.A., et al., Localization of intraflagellar transport protein IFT52 identifies basal body transitional fibers as the docking site for IFT particles. *Curr Biol*, 2001. **11**(20): p. 1586-90.
129. Pedersen, L.B., et al., *Chlamydomonas* IFT172 is encoded by *FLA11*, interacts with CrEB1, and regulates IFT at the flagellar tip. *Curr Biol*, 2005. **15**(3): p. 262-6.
130. Zhu, X., et al., IFT54 regulates IFT20 stability but is not essential for tubulin transport during ciliogenesis. *Cell Mol Life Sci*, 2017. **74**(18): p. 3425-3437.
131. Wingfield, J.L., et al., IFT trains in different stages of assembly queue at the ciliary base for consecutive release into the cilium. *Elife*, 2017. **6**.
132. Xie, C., et al., Optimal sidestepping of intraflagellar transport kinesins regulates structure and function of sensory cilia. *EMBO J*, 2020: p. e103955.
133. Funabashi, T., et al., Ciliary entry of KIF17 is dependent on its binding to the IFT-B complex via IFT46-IFT56 as well as on its nuclear localization signal. *Mol Biol Cell*, 2017. **28**(5): p. 624-633.

134. Omori, Y., et al., elipsa is an early determinant of ciliogenesis that links the IFT particle to membrane-associated small GTPase Rab8. *Nat Cell Biol*, 2008. **10**(4): p. 437-44.
135. Vaughn, J.L. and F. Fan, Differential requirements of two insect cell lines for growth in serum-free medium. *In Vitro Cell Dev Biol Anim*, 1997. **33**(6): p. 479-82.
136. Vaughn, J.L., et al., The establishment of two cell lines from the insect *Spodoptera frugiperda* (Lepidoptera; Noctuidae). *In Vitro*, 1977. **13**(4): p. 213-7.
137. Schneider, C.A., W.S. Rasband, and K.W. Eliceiri, NIH Image to ImageJ: 25 years of image analysis. *Nat Methods*, 2012. **9**(7): p. 671-5.
138. Oberhofer, A., et al., Myosin Va's adaptor protein melanophilin enforces track selection on the microtubule and actin networks in vitro. *Proc Natl Acad Sci USA*, 2017. **114**(24): p. E4714-E4723.
139. Erdmann, R.S., et al., Labeling Strategies Matter for Super-Resolution Microscopy: A Comparison between HaloTags and SNAP-tags. *Cell Chem Biol*, 2019. **26**(4): p. 584-592 e6.
140. Liss, V., et al., Self-labelling enzymes as universal tags for fluorescence microscopy, super-resolution microscopy and electron microscopy. *Sci Rep*, 2015. **5**: p. 17740.

Acknowledgments

So he [Sulaiman (Solomon)] smiled, amused at her speech and said: "My Lord! Inspire and bestow upon me the power and ability that I may be grateful for Your Favors which You have bestowed on me and on my parents, and that I may do righteous good deeds that will please You, and admit me by Your Mercy among Your righteous servants."

Surah An-Naml [verse 19]

First and Foremost, All praise is due to Allah.

Writing these acknowledgements gives me the opportunity to thank all the people who have been involved directly or indirectly to the development of this work.

I would like to express my sincere and deep gratitude to my supervisor Zeynep Ökten, for support, guidance, encouragement, and enlightening discussions during my PhD.

I am indeed indebted to Hieu for personal and technical support at crucial stages of this work.

On an academic and personal level, I am grateful to my friend Willi Stepp, for helping me to integrate into the German culture, fruitful scientific discussions and opinions, activities outside academia, and his positive attitude over the past years.

In the same line, I am very thankful to the Stepp family Herbert and Karin, for their generosity and great hospitality at their home in München and Bramberg, Austria.

Thanks to all of the Ökten's lab members for creating such a productive working environment. For penetrating comments on my thesis and coffee breaks, I acknowledge Georg Merck and Willi Stepp.

Of course, I will never forget the precious help of the secretary team: Elke Fehsenfeld, Nicole Mittermüller, and Anne Ploß, during bureaucratic difficulties.

Thanks to all members of E22 and E27 who have listened to my talks and never stopped of giving me constructive inputs on my work.

On a personal note, I owe everything to my parents Zeinab and Antar who are constantly pushing me forward. To my brothers Ahmed and Abdul-Wahab, my uncles Salah and Abdul-Wahab, and my aunt Awatif, thanks for your genuine and ceaseless support. To the little kids Aya and Omar, for brining joy, laughter, and happiness into our family.

Finally, I dedicate this work to my mother and my grandparents.